ESA-QCA00104T-C

EUROPEAN SPACE AGENCY
CONTRACT REPORT

The work described in this report was done under ESA contract. Responsibility for the contents resides in the author or organisation that prepared it.

# FINAL REPORT

## Radiation Testing of EEV CCDs for the MERIS Programme

**Author: G R Hopkinson**

ESTEC CONTRACT No: 9557/91/NL/LC(SC)
SIRA CONTRACT No: A/9119/00

AUGUST 1992

SIRA RESEARCH & DEVELOPMENT

RESEARCH & DEVELOPMENT

SIRA LTD · SOUTH HILL · CHISLEHURST · KENT · BR7 5EH · ENGLAND
TELEPHONE: 081 467 2636 · INTERNATIONAL: + 44 81 467 2636
TELEX: 896649 · FACSIMILE: 081 467 6515

Sira Ltd is an independent organisation, incorporated in 1918, which operates internationally providing laboratory and engineering services for research, development, evaluation and applications of scientific and industrial instrumentation and control equipment.

The Research and Development Division undertakes research, development, design applications and consultancy with multi-disciplinary teams of engineers and scientists. The Division also supplies contracting services to national and international procurement agencies and engineered equipment on a commercial basis for specialist applications.

**EUROPEAN SPACE AGENCY CONTRACT REPORT**

The work described in this report was done under ESA contract. Responsibility for the contents resides with the author or the organisation that prepared it.



---

**Final Report**

# Radiation Testing of EEV CCDs for the MERIS Programme

**ESTEC Contract No: 9557/91/NL/LC(SC)**
**Sira Reference No: A/9119/00**

**Author: G R Hopkinson**

**August 1992**

---

# Radiation Testing of EEV CCDs for the MERIS Programme

## FINAL REPORT

**ESTEC Contract No: 9557/91/NL/LC(SC)**
**Sira Contract No: A/9119/00**

| | |
|---|---|
| Issue | Final |
| Authorisation | |
| Date | August 1992 |

# CONTENTS

CONTENTS

# EXECUTIVE SUMMARY

This report looks at space radiation effects on EEV CCDs operated at near room temperature and at pixel rates of the order of 1MHz. The MERIS (MEdium Resolution Imaging Spectrometer) instrument will use six back illuminated frame transfer CCDs and will form part of the payload for ESA's first Polar Orbiting European Mission (POEM-1). CCDs from EEV Ltd (UK) are candidate detectors for this mission, which is highly demanding of CCD performance - particularly of dark current stability and calibration accuracy. The present test campaign uses cobalt60 gamma rays to simulate ionization damage in the CCD gate oxide and SiO2/Si interface and 10 MeV protons to simulate bulk displacement damage. The resulting database will be used in the instrument design to assess the impact on instrument performance and determine parameters such as operating temperature, CCD bias voltages and calibration strategies. The programme follows on from a similar analysis performed on Thomson-CSF devices for the SILEX programme. Transient effects on CCDs, due to ionizing particles and bremsstrahlung, are also considered from a theoretical viewpoint.

First we consider some basic results from the study which can be compared with data from the SILEX tests on standard process (non-MPP) Thomson CSF devices [9].

Looking at ionization damage we find that, as for Thomson devices, biasing the CCDs during irradiation gives a worst case for flatband voltage shifts. For EEV devices the shift is ~0.05V/krad when biased compared with 0.1V/krad for Thomson-CSF CCDs. Flatband voltage shifts can produce changes in gain of the output amplifier (and hence charge to voltage conversion factor). The change is likely to be less than 10% after 4 krad for EEV CCDs, but further measurements may be necessary for flight representative devices. For surface dark current the standard Thomson process gives a value of ~12 nA/cm$^2$/krad at 21°C - allowing for reverse annealing (build-up of interface states) over a period of several months after irradiation. Though unbiased devices show damage reduced by roughly a factor 2. In contrast the value for EEV devices is ~1 nA/cm$^2$/krad and is essentially bias independent. There was no measurable difference in behaviour between front illuminated and back illuminated EEV devices. EEV devices also show reverse annealing of dark current.

For both Thomson-CSF and EEV devices the flatband voltage shifts are larger for cobalt60 irradiation than for normally incident 10 MeV protons. In this study, using 100 MeV protons and non-normal incidence gave comparable results for $Co^{60}$ and proton irradiation. In contrast to previous results on Thomson-CSF devices, surface dark current increases for $Co^{60}$ and 10 MeV protons were very similar. Note that variations in ionization damage with type of irradiation are most likely due to differences in the amount of e-h recombination in the oxide (which is field - and therefore device - dependent).

We should note that though the two types of device are both n-buried channel, polysilicon electrode CCDs with an oxide/nitride dielectric there are basic differences in channel stop technology. Thomson use a conventional locos isolation whereas EEV use a process which keeps the buried channel away from the channel stop boundaries. Also the bias dependence of the ionization damage will depend on the magnitude and polarity of electric fields present within the gate oxide and the channel stop which may not be zero for no bias because of built in voltages due to implants. It is therefore to be expected that bias dependence can depend on CCD design.

For bulk displacement damage, the dark current increase is similar for both device types: 0.1 nA/cm$^2$ increase/krad of normally incident 10 MeV protons at 21°C - and is independent of bias during irradiation. The change in dark current does not seem to depend on the silicon resistivity or epitaxial layer thickness. This is somewhat unexpected and suggests the possibility of an effective diffusion length for radiation induced vacancies/interstitials. Modelling of dark current histograms suggests a value of 4μm.

For the EEV devices used in this study there was the possibility of operating with the CCD surface in inversion. This was achieved by increasing the substrate voltage relative to the image area clock low voltage. This inverts the surface under the low phases. By periodically switching the clock high voltage from phase one to phase two the surface under both electrodes can be kept inverted all the time - if the time between switches is shorter than the trap time constant. Hence we have a state of full inversion and significant suppression of surface dark current. In this report we term this mode of operation dither clocking. The suppression of dark charge also applies to the storage region component generated during readout. It was found however that the suppression in surface dark current at room temperature was not as high as expected - particularly after irradiation. The temperature behaviour of the remaining component suggests a dependence on $n_i^2$ - the square of the intrinsic carrier concentration. There will be a component with this dependence arising from thermionic emission and diffusion to the depletion layer, however this is an intrinsic mechanism and is not defect (or irradiation) related. We surmise that the surface may not be strongly inverted over the whole pixel area and that weak inversion in some areas allows the generation of a surface component. Two implanted inversion mode (IMO or MPP) devices were also tested and gave similar results - although the statistical sample is too small to draw definite conclusions on EEV IMO devices. The main emphasis for MERIS is to achieve inversion through the dither clocking technique since this gives a better value for full well capacity in current technology EEV devices.

In common with previous studies we find that the dither clocking technique can give rise to additional dark charge nonuniformity because of trapping effects. However we find that the effects are small in comparison with other nonuniformities. If necessary, changes to CCD clock biases removes the effect.

Results for EEV devices under full inversion suggest an increase of ~0.4 nA/cm$^2$ per krad at 21°C - though this is a rather conservative value since some devices gave better performance. A value of ~0.2 nA/cm$^2$ per krad is more typical. Also the strong temperature dependence (effective activation energy ~0.85 eV) gives a large improvement on cooling the CCD. Added to this component is the bulk displacement damage of 0.1 nA/cm$^2$/krad at 21°C for 10 MeV protons (which has an effective activation energy of 0.63 eV).
As well as a detailed examination of the temperature behaviour of the various dark charge components and the revelation of unexpected effects for inverted mode operation plus the work on bulk displacement damage leading to the suggestion of a diffusion length for bulk damage, this study has given the opportunity to make discoveries in other areas:

i) For the first time, the charge transfer efficiency for fast readout, room temperature conditions has been accurately measured. The data gives a damage constant for parallel charge transfer loss (change in charge transfer inefficiency per pixel, divided by proton fluence) for 6,000 electron signals (from a $Cd^{109}$ x-ray source) of 3.4 x $10^{-14}$ cm$^2$ at 15°C for normally incident 10 MeV protons - a value significantly less than found for slower readout

rate x-ray astronomy studies (XMM). This lends support to the theory that the capture time constant of the radiation-induced traps is an important parameter; as does the finding that serial CTE damage is a factor 5 less than parallel CTE loss for MERIS conditions. As might be expected, the emission time constant governs into which pixel the lost (deferred) charge falls - and this parameter therefore also has an effect on the MTF.

ii) Studies on developing an optical method of CTE measurement have lead to a promising new technique which gives results for CTE comparable with the x-ray method and gives information on the variation of CTE with signal size (revealing a near linear relationship).

iii) An important new finding is that the bulk dark current resulting from proton displacement damage can be unstable in time and gives rise to a random telegraph signal (RTS) behaviour. The fluctuations can be up to ~0.4nA/cm$^2$ at 21°C for some pixels, though vales ~0.1 nA/cm$^2$ are more common. Time constants for the process are increased on cooling. Tentative theories are discussed in this report. A suggestion is that thermionic capture and emission from traps at or near the $SiO_2$/Si interface leads to local enhancements in electric field which in turn leads to field-enhanced emission from defects in the vicinity of the trap. We give pixels which show RTS behaviour the name 'flipper' pixels since they flip from state to state. Time constants for 'flipping' are of order several minutes at room temperature and increase on cooling.

iv) It appears that the offset voltage between reset and video levels when there is no signal present (ie. for overclocked pixels) is a parameter which needs to be measured for EEV devices (and perhaps for other CCDs also). There can be a large change in offset voltage with radiation if inappropriate CCD biases are used (for $V_{OG}$ and $V_{RD}$). It is expected that a change in CCD design (already implemented) and attention to the optimum setting of CCD biases will minimise the effects.

Finally this study analyses the mission environment (788 km polar orbit) in order to predict effects from the ground test data. The proton environment (after shielding) is equivalent to 3.6 x 10$^9$ normally incident 10 MeV protons/cm$^2$ at solar maximum and 5.6 x 10$^9$ per cm$^2$ at solar minimum. This allows the following predictions for end of life:

| | **solar minimum (4 years)** | **solar maximum (4 years)** |
|---|---|---|
| Parallel CTI change (per pixel) | 1.9 x 10$^{-4}$ | 1.2 x 10$^{-4}$ |
| Serial CTI change (per pixel) | 3.4 x 10$^{-5}$ | 2.2 x 10$^{-5}$ |
| Bulk dark current increase (nA/cm$^2$ at 21°C) | 0.31 | 0.20 |
| Surface dark current increase (nA/cm$^2$ at 21°C), noninverted | 1.4 (average environment, 1.4 krad) | |
| Surface dark current increase (nA/cm$^2$ at 21°C), inverted | 0.28 (average environment, 1.4 krad) | |

The effect of transient charge production from proton and bremsstrahlung events is also considered. These transient events can have significant consequences during passage through the South Atlantic Anomaly and the polar horns.

# 1. INTRODUCTION

## 1.1 Background

This report concerns results from a radiation test campaign devised in order to assess the performance of CCDs manufactured by EEV Ltd (Chelmsford, UK) under conditions appropriate to the MERIS instrument. MERIS is the MEdium Resolution Imaging Spectrometer which will fly on ESA's POEM-1 mission, scheduled for launch in 1998 into a 800 km sun-synchronous polar orbit for a planned mission life of 4 years (Figure 1.1-1).

MERIS will use six n-buried channel, 100Ω cm back illuminated CCDs, each operated in the frame transfer mode and having 780x576 image area pixels. At present CCD operating temperature is baselined at 20°C. The pixels will be readout at a rate close to 1 MHz. Not every line is readout. Those corresponding to unwanted parts of the spectrum will be passed to a dump gate which runs adjacent to the readout register. In addition there are modes of operation which bin pixels together on-chip (up to 4 adjacent lines can be binned together into the readout register and up to 4 of these binned lines can be combined at the output amplifier (thus giving up to 4x4 binning). Using these techniques the frame integration time is reduced to a nominal value of 37.6ms. The line move rate is 0.5 MHz.

In order to achieve a high radiometric accuracy, particularly in the red region of the spectrum, it is necessary for the CCD dark current to be accurately calibrated. Hence the behaviour of the radiation-induced dark current is a major concern, as is stability of the output signal (in terms of gain and offset) and the magnitude of threshold voltage shifts. Since MERIS is an imaging instrument, degradation in MTF (caused through loss in CTE) is also of interest.

The Earth's radiation environment is discussed in several recent reviews (for example [1], [2], [3]). In a polar orbit the CCD will encounter trapped protons during passage through the South Atlantic Anomaly (SAA) and bremsstrahlung photons during passage through the north and south horns of the inner zone electron belt (the electrons themselves will be ranged out by the instrument shielding). In addition the instrument will encounter protons and heavy ions from solar flare events (and to a lesser extent from galactic cosmic rays). An analysis of the environment has been carried out by Aerospatiale (document PP-TN-AER-ME-0010 issue 01). Figure 1.1-2 shows dose depth curves during solar maximum and minimum. The expected mission dose for the CCDs is approximately 1.4 krad(Si).

In order to predict the effects of proton-induced bulk damage it is also necessary to know the energy spectra of the protons.

This information was provided by ESA (as a result of analysis by B Johlander using the 'Space Radiation' code). Bremsstrahlung spectra were not available for this orbit, however the shape of the initial electron energy distribution dose not vary greatly with orbit and use was made of an earlier study by Stassinopoulos, Barth and Smith [4] for the ROSAT orbit (model was for a 535km orbit, 57° inclination). Mission analysis is discussed in section 5.

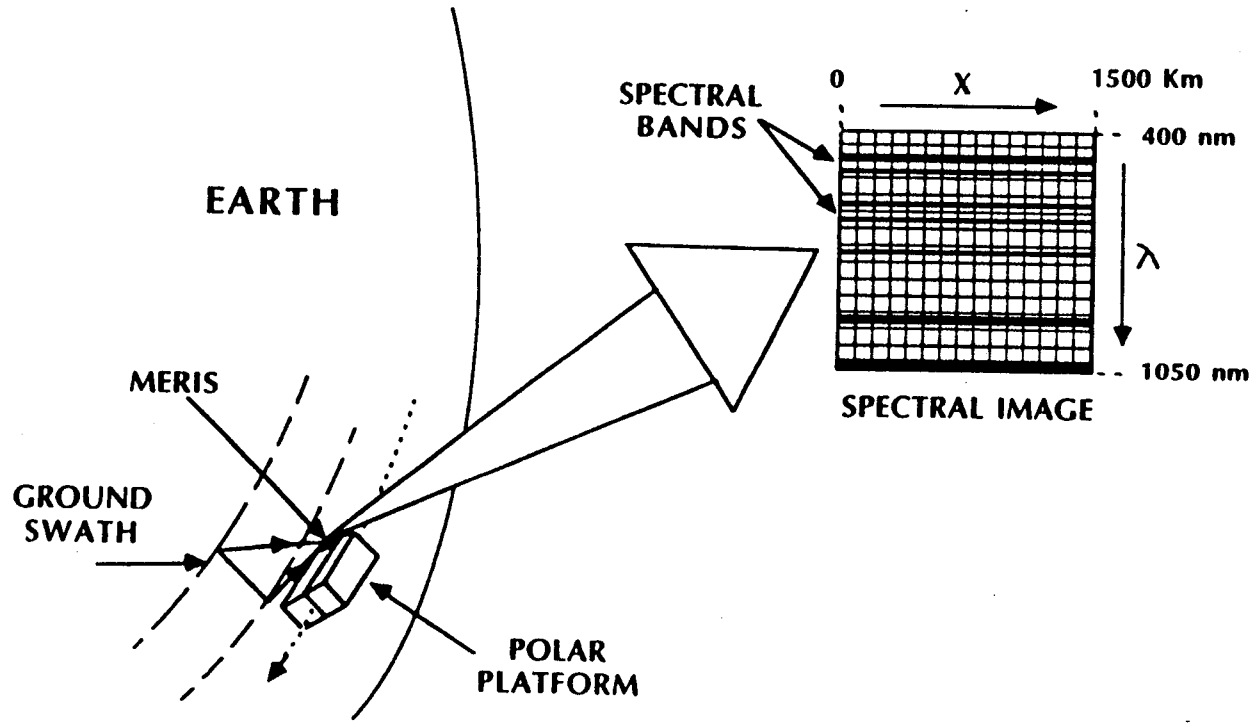


MEDIUM RESOLUTION IMAGING SPECTROMETER (MERIS)

**Figure 1.1-1 Schematic of the MERIS instrument**

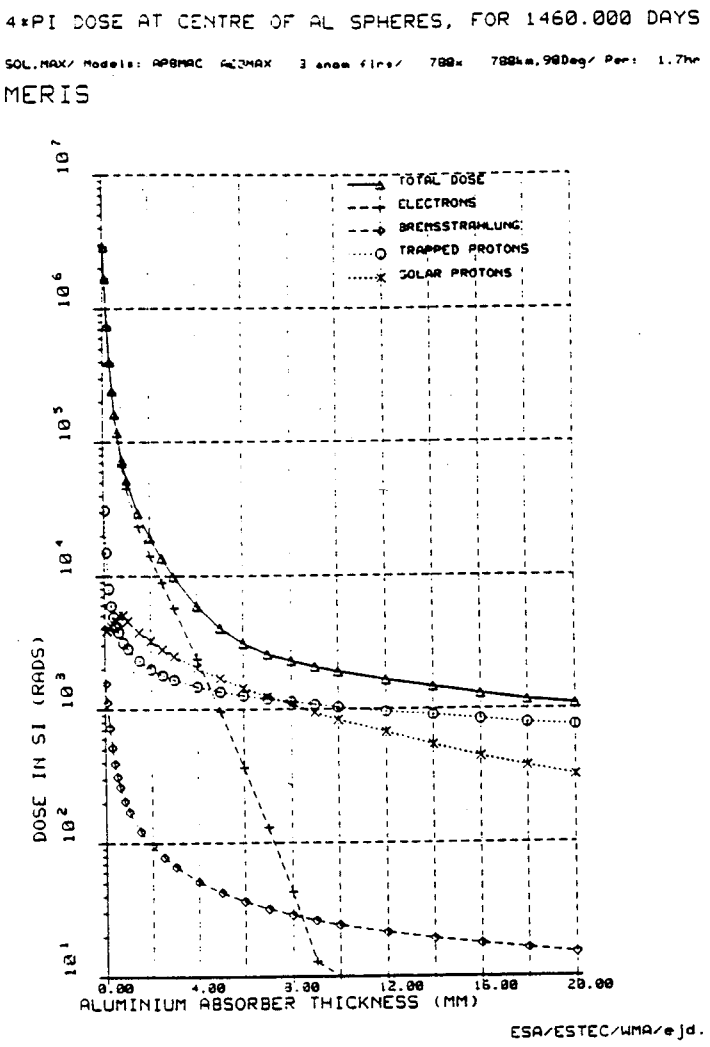


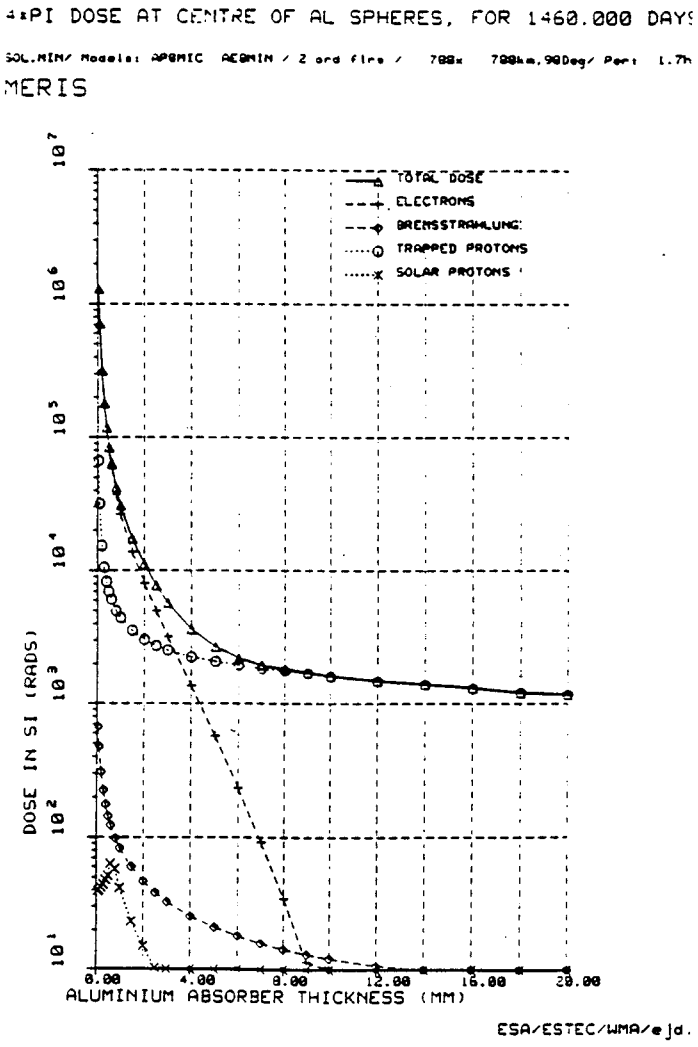


**Figure 1.1-2 Dose depth curves for the MERIS orbit for solar maximum and solar minimum**

## 1.2 CCD Radiation Effects

Radiation effects in buried channel CCDs have been discussed in several reviews ([5] to [9]) and in a recent ESA Contract report [10]. Two recent papers ([11], [12]) by the group at Brunel University (UK) refer to EEV devices and are specifically relevant to this study.

Work for the XMM mission ([13], [14]) also refers to EEV CCDs but for operation under cooled, slow scan conditions (where, in particular, CTE effects are worsened and dark current generation is not important because of the low temperature).

Briefly we summarise by noting the following effects which will be induced by encounter with the space radiation environment:

*i) ionisation damage*

Charge build-up in oxide layers and interface trap generation. Produces shifts in flatband voltage and increases in surface dark current.

The flatband voltage is the gate voltage (in an MOS device) needed to acheive a condition of no band bending at the CCD surface. It is a convenient reference voltage for device effects. Gate voltages other than the flatband voltage willl give accumulation, depletion or inversion, depending on their magnitude and polarity relative to the flatband voltage (figure 1.2-1).

*ii) Bulk displacement damage*

Trapping and dark current generation centres are produced in the buried channel and in the depletion region. This results in a loss in charge transfer efficiency (CTE) and increased dark charge nonuniformity.

*iii) Transient effects*

These result from generation of spurious signals in the silicon by the passage of charged particles or absorbtion/Compton scattering of bremsstrahlung photons (x-rays and gamma rays). The effects are not permanent since the charge is swept out during readout.

In this study $Co^{60}$ and proton irradiation has been used to simulate the space environment and assess the magnitude of these effects for MERIS. We also note that there is another possible effect in that highly energetic particles, such as cosmic rays, could cause localised damage in the CCD electrode structure and reductions in reliability. This has never been investigated however.

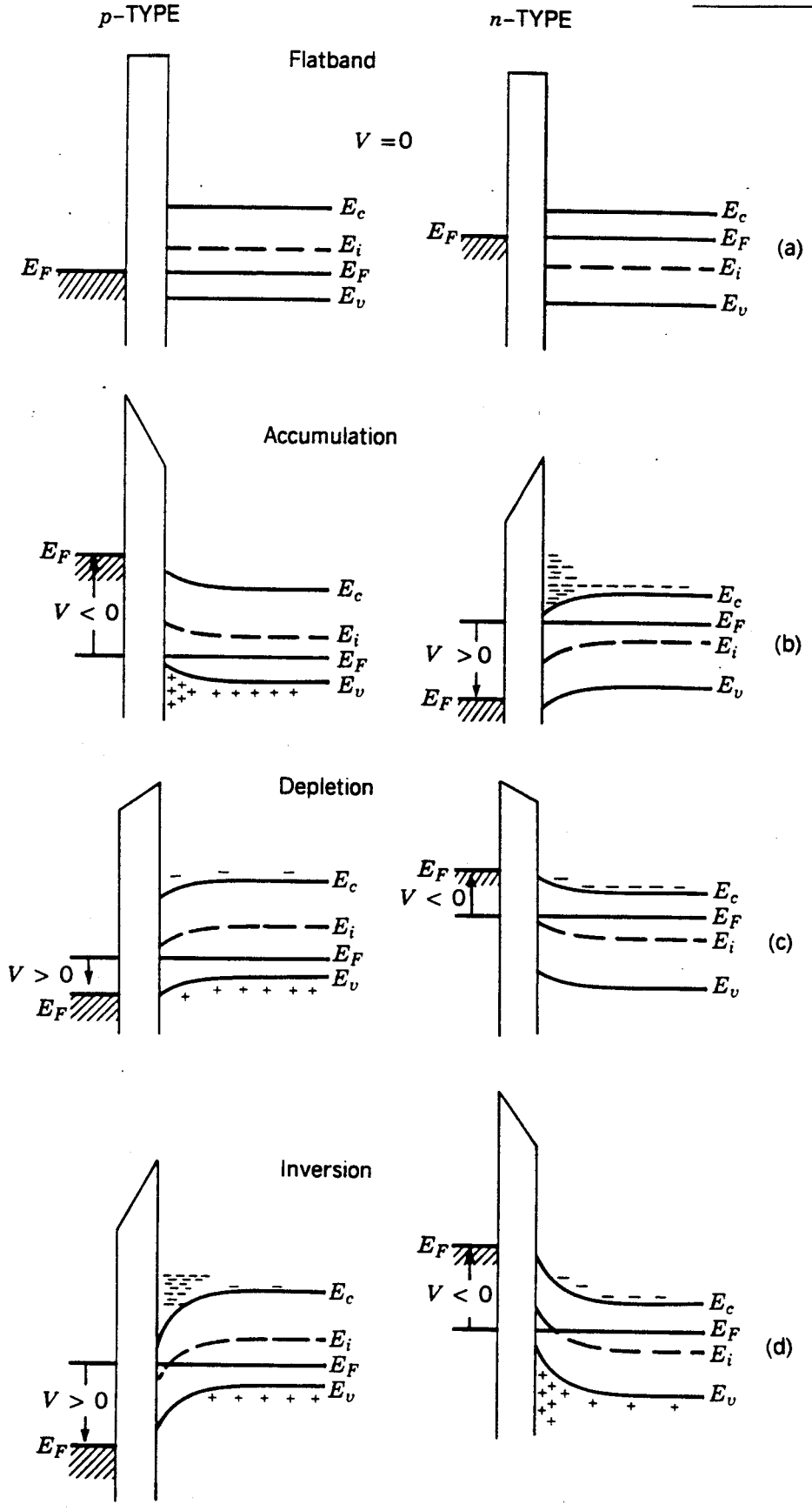


**Figure 1.2-1 Energy band diagrams of ideal MOS capacitors.**

**A/9119/00**

## 1.3 Test Overview

Because representative large area back illuminated devices are at present under development and were not available for this study, the work was carried out on a variety of commercial devices, both front and back illuminated.

Two device formats were used: the CCD05 (780x1152 pixel, 22.5μm square pixels) and the CCD02 (385x576, 22.0μm square pixels). Cobalt 60 irradiations were performed on both powered and unpowered devices at a dose rate of 1.73 krad(Si)/hour at room temperature, to a total accumulated dose of 4 krad(Si). 10 MeV proton irradiation was carried out at 3 fluences amounting to 1, 2 and 4 krad(Si) (ie. 1.79, 3.58 and 7.16 x $10^9$p/cm$^2$). As in a previous investigation [10] the CCD image area was masked by a 1mm thick aluminium plate so as to give (up to) the four different dose regions (0, 1, 2 and 4 krad) on the same chip. All proton irradiations were carried out unpowered. One device was irradiated at four different angles of incidence (22.5°, 45°, 67.5° and 90°). In addition, two EEV 385x576 pixel devices were irradiated during a previous investigation (for the SILEX programme [10]) to 0, 3, 6 and 9 krad on each chip. One device was powered and one not. In all cases post-irradiation measurements of dark current and operating voltage shifts were performed periodically over several months to check for annealing behaviour. One device was given a 24 hour 100°C bake after 3 weeks in order to accelerate the (reverse) annealing of the surface dark current. Measurements on charge transfer efficiency were also made on two of the large area devices, after irradiation. The charge to voltage conversion factor of the CCD output node was also measured for each device.

# 2. EXPERIMENTAL DETAILS

## 2.1 Radiation Facilities

Cobalt 60 testing was performed at AEA Technology, Harwell in one of the Hi-Rad cells at a dose rate of 1.73 krad/hr. Dosimetry was obtained using an ionex monitor mounted adjacent to the arrays. Cables leading into the cell from remote drive electronics allowed the powered (and clocked) operation of CCDs during irradiation (one at a time).

Proton testing was carried out using 10 MeV protons from the Tanden van de Graaff accelerator at Harwell with dosimetry to ~5% carried out using a silicon detector. In addition, two 385x576 pixel CCDs were irradiated by ESA personnel with 100 MeV protons at the SATURNE accelerator in France.

## 2.2 Test Objects

The majority of devices tested were n-buried channel front illuminated frame transfer CCDs of two types:

| | | |
|---|---|---|
| CCD02 | : | 288x385, 22x22μm image area pixels |
| CCD05 | : | 780x576, 22.5x22.5μm image area pixels |

Both types use 3 phase, three level polysilicon electrodes for all clocks. In addition two CCD02 devices were thinned and back illuminated and another two had implanted regions to allow full inversion of the surface:- so called inverted mode operation (IMO) or multiphase pinned (MPP) devices. One of the larger CCD05 devices was fabricated on a 100Ω cm epitaxial layer ie. one with a higher resistivity than standard devices (which are ~20Ω cm) and which is representative of the MERIS CCDs (which will also be 100Ω cm). This device however has an epi thickness of 100μm whereas the MERIS devices will have ~20μm. All devices had temporary glass windows which were removed for proton testing.

## 2.3 CCD Test Electronics and Operating Conditions

CCD test equipment is essentially as described in a previous ESA Contract report [10]. Figure 2.3-1 shows a block diagram of the test set-up.

### 2.3.1 Computer and Frame Grabber

The data capture and analysis was performed using a Solidisk 486 AT-compatible computer with 300 Mbyte hard disk. It was operated under MS-DOS and was attached to two multisync colour monitors, one being used for entering commands the other for display of CCD images. Slotted into the AT-bus was a VS100 framegrabber/image memory card manufactured by Imaging Technology Inc. This is capable of capturing normal CCIR video signals or non-CCIR variable scan rate pictures up to a pixel rate of 10MHz. The image memory is 1024x1024x12 bits deep. A 512x512 window of this memory can be output to the display at any one time.

The variable scan rate pictures can be input either as digital data up to 12 bits deep or, as in this case, as an analogue signal to be digitised with an internal ADC. The internal ADC digitises to 8 bits. The synchronisation of the frame grabber with the variable scan rate outputs from CCDs is controlled from Digital Interface, (para 2.3.6).

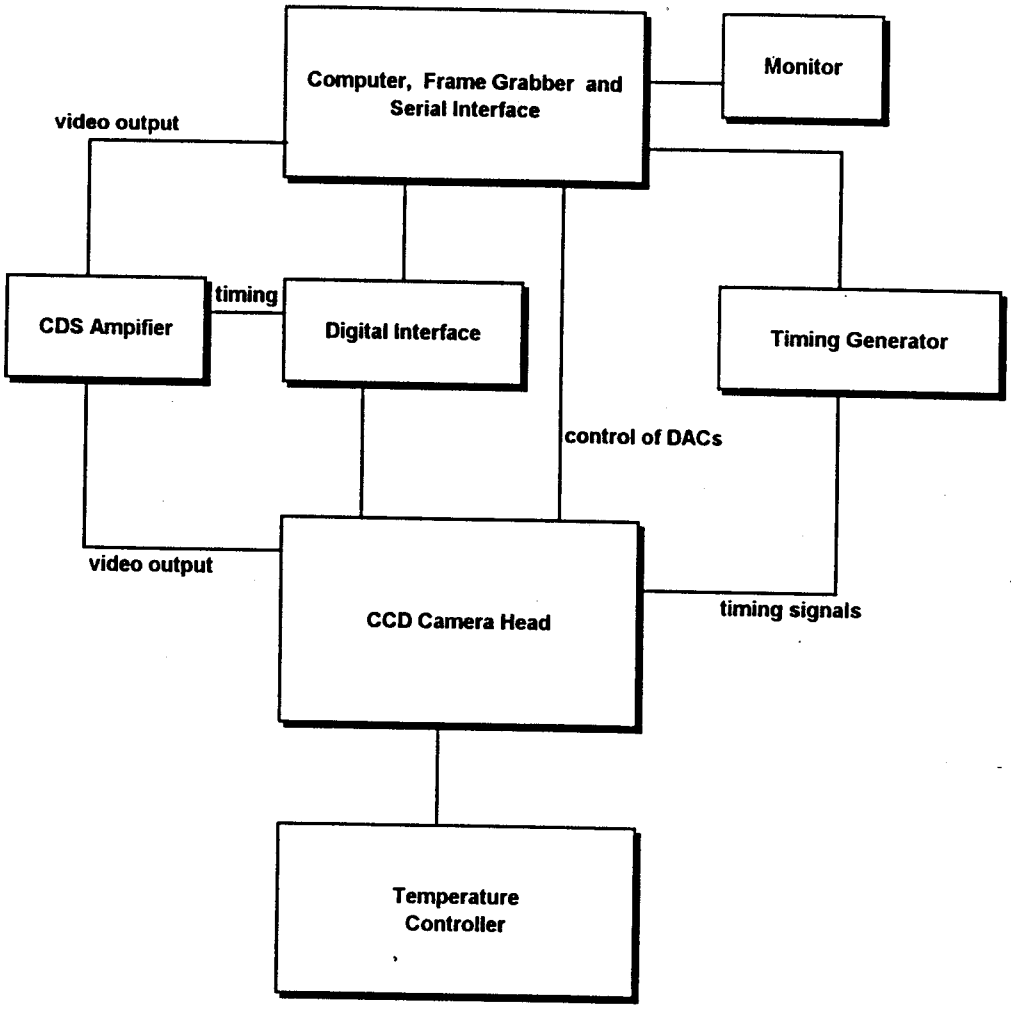


**Figure 2.3-1 Block diagram of the CCD test electronics**

### 2.3.2 Programmable Timing Generator

The Timing Generator produces TTL level clock waveforms for the CCD. It is non-specific and can generate waveforms for any current size of 3 or 2/4 phase device. It consists of a series of RAM-controlled sequencers. The number and frequency of pulses in a train and the grouping together of different trains to form the overall pulse sequence for the CCD are variable. Sequences are generated by typing user-friendly high level statements on the host computer to generate a file containing the sequence information. This file is then down-loaded to the RAM in the Timing Generator via the parallel printer port.

Because the pulse trains are variable, it is simple to generate the sequences necessary for functions such as on-chip binning, pocket pumping, variation of integration time etc.

The Timing Generator operates at clock rates of up to 32MHz, giving a maximum 16MHz pixel rate for devices with 2 phase output registers and 11MHz for 3 phase devices. There are 23 separate output lines, thus allowing for control of external circuitry such as clamps, sample and holds and ADCs, as well as clocking the CCD.

In general it is possible to store several different complete sequences in the timing generator at any one time, though the number depends on their complexity. Hence the operator can switch sequences without reloading from the host computer. This is particularly useful for example when changing integration times.

### 2.3.3 Power Distribution Unit

This was a set of bench power supplies for providing bias to the programmable timing generator and camera head(s).

### 2.3.4 CCD Camera Head and Temperature Controller

This unit enables operation of single CCDs during detailed characterisation of electro-optical properties. In each case the CCD was placed in a zero-insertion-force socket fitted with a copper heatsink bar coupled to a Marlow Industries MI1049T Peltier cooler (two types of socket were used with the same camera so as to accommodate both CCD02 and CCD05 devices). The Peltier cooler was driven by a power amplifier contained in a separate temperature controller box. Servo control of the temperature, as monitored at the heatsink bar, was possible to better then ±0.05°C but note that the actual temperature at the CCD die will differ from the set temperature because of the contact resistance between the copper heatsink bar and the ceramic package and because of the heat dissipation in the CCD. Beneath the CCD socket was a single board containing MOS level clock drivers and a preamplifier. A second board contained DAC controlled bias supply regulators (in turn controlled via a serial interface in the AT computer).

### 2.3.5 Analogue Interface

This contains a variable switched gain amplifier and correlated double sampling circuit of the clamp and sample type. The positions of the sample points were settable using tapped delay lines. The switched gains available were x1, x7.96 and x45.0 (a second switch on the camera units provided an additional gain of x1 or x2). A potentiometer allowed a continuous gain multiplier between 0 and x1. The sampled output was then passed to the 8-bit ADC on the VS100 board.

### 2.3.6 Digital Interface

This unit takes single ended TTL logic signals from the timing generator and camera heads and converts them to the differential TTL signals needed by the VS100 frame grabber; also some signals are inverted at this point.

### 2.3.7 Test Software

Sira has written system-level software which acts as an interpreter for the VS100 image memory board functions and allows these functions to be selected in a user-friendly manner and assembled together to form sequences for automated testing or data analysis. Examples of functions available with simple commands are:

* image acquisition (either continuously or as single frames)
* pan and zoom
* image scaling and off-setting
* display of a cursor on the image display and readout of a 5x5 matrix of pixel values on the computer console
* cursor movement from keyboard or mouse
* selection of points, lines, columns or areas of interest by keyed commands or by mouse
* calculation of mean and standard deviation of areas of interest and display of histograms. Also dumping of this data to a file
* recording of intensity profiles across slices through images
* detection of pixels above or below a set threshold (eg. for analysis of image non-uniformity)
* adding or averaging successive images to reduce random noise
* addition, subtraction, division or multiplication by previously stored images
* statistical analysis of values from one pixel (or a group of pixels) from successive frames for noise analysis
* saving of image data, either in VS100 or standard TIF (tagged image file) format
* operations on input and output look-up tables (LUTs)
* control of Unidex mirror drives
* control of Bentham Instruments monochromator.
* control of bias supply voltages in the CCD camera head.

Examples of sequences of operations are:

* definition of sequences of regions of interest and recording of mean, standard deviation etc.

* repeated searching for pixels above (or below) a threshold in successive images and recording data in a file - as used in analysing data from x-ray events from calibration sources.

* interaction with the programmable timing generator so as to form linearity plots by successive changes in integration time and recording of image values from a specified region of interest.

Data files (such as histograms) can be analysed and plotted using standard spreadsheet or graphics packages. This is made easy since it is possible to flip in and out of the command program without reloading any parameters or losing the screen display.

Built into the command program were safeguards to ensure that files could not be overwritten by giving two files the same name. The database was organised by giving each CCD a unique directory. All files relating to a CCD were stored in its directory. To keep track of the current directory the directory name appears as the prompt from the command program.

### 2.3.8 Operating Voltages

A Device schematic is shown in figure 2.3-2. The CCDs were operated with the following voltages as standard. In some particular cases small adjustments to VOG and VRD were made to get improved performance.

| **Name** | | **Symbol** | **Voltage** |
|---|---|---|---|
| Amplifier output drain | | $V_{OD}$ | 26.49 |
| Reset drain | | $V_{RD}$ | 15.47 |
| Output gate | | $V_{OG}$ | 1.19 |
| Substrate | | $V_{SS}$ | Variable (4 to 9.5V) |
| Image area clock | high | | 10.0 |
| " | low | | -0.49 |
| Storage area clock | high | | 10.0 |
| " | low | | -0.49 |
| Readout area clock | high | | 10.0 |
| " | low | | 0.0 |
| Reset clock high | | | 10.0 |

### 2.3.9 CCD Clocking

The CCDs were operated in frame transfer mode, with a line move time of 2μs (parallel transfer) and a pixel time of 1μs for "normal" (ie. non-dumped) serial readout.

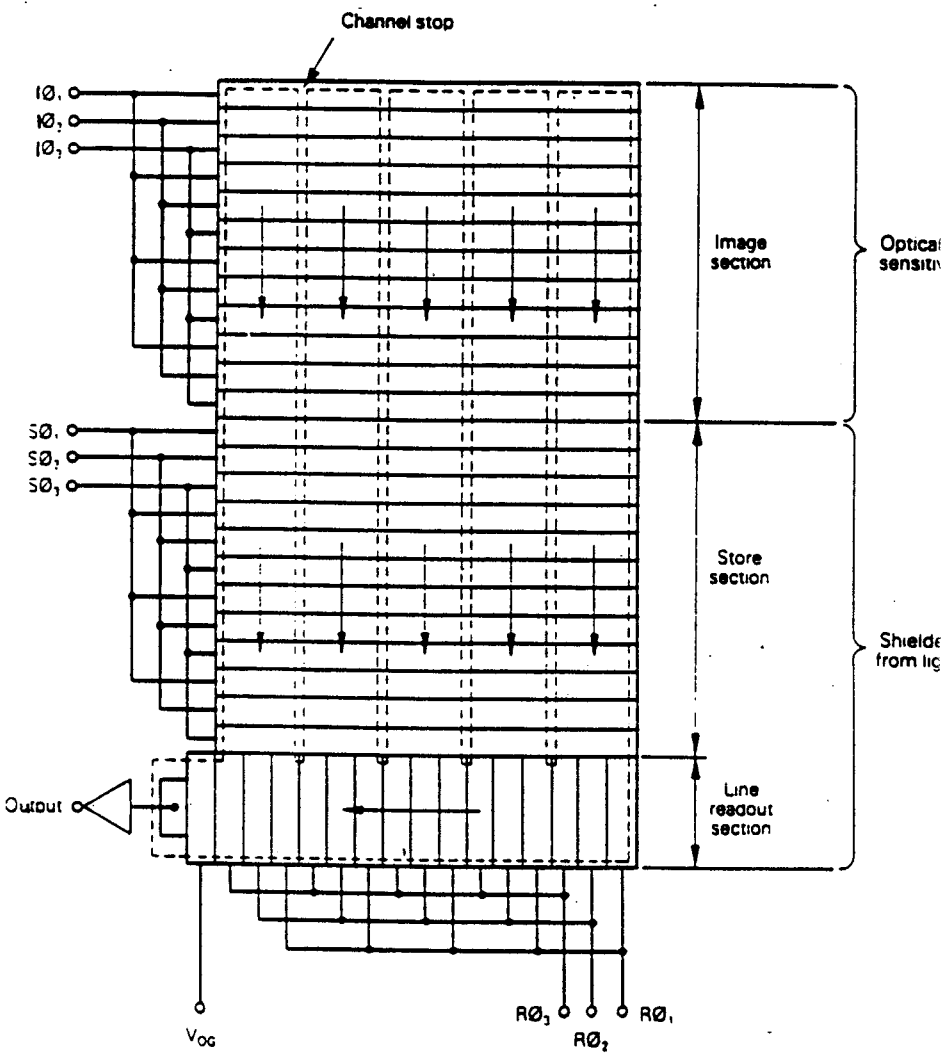


**OUTPUT AMPLIFIER SCHEMATIC**

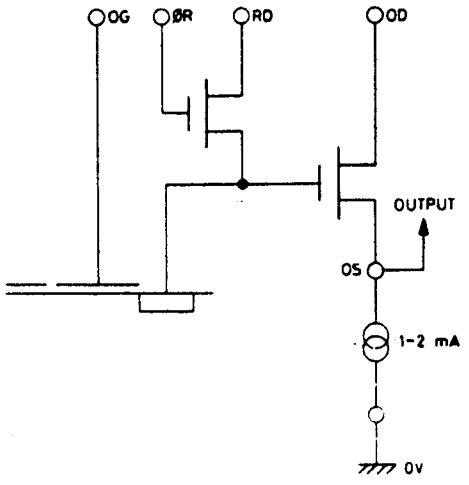


**Figure 2.3-2 Schematic diagram of an EEV CCD02**

## 2.4 Radiation Test Histories

Table 2.4-1 summaries the irradiations given to each device.

**Table 2.4-1**

| Devices: | | Sira Number | dose regions across chip [(krad Si)] | EEV Part Number |
|---|---|---|---|---|
| 2 CCD02-06-5-219 | IMO | 01 | 10 MeV [4,1,0,2] | A0451-62 |
| | | 02 | 100 MeV [1 krad] | A0451-52 |
| 2 CCD02-06-5-206 | Back- | 03 | 10 MeV [4,0,0,2] | A0658-47 |
| | illum. | 04 | Co $^{60}$, Powered | A0658-9 |
| 2 CCD05-20-5-222 | 100Ωcm/100μm | 15 | 10 MeV [4,1,0,2] | A0693-7 |
| | | 16 | spare | A0693-4 |
| 4 CCD05-20-5-202 | standard | 11 | spare | A0576-18-9 |
| | | 12 | 10 MeV [4,1,0,2] | A0577-19-10 |
| | | 13 | Co$^{60}$, Powered | A0576-18-12 |
| | | 14 | Co$^{60}$, not Powered | A0694-9 |
| 3 CCD02-06-5-202 | standard | 05 | 10 MeV [4,0,0,2] | A0354-44 |
| | without | 06 | Co$^{60}$, not powered | A0354-16 |
| | store shield | 07 | Co$^{60}$, not powered | A0354-036 |
| 3 CCD02-06-5-019 | standard | 08 | 10 MeV [4,1,0,2] | 8218-13-27 |
| | store shield | 09 | 10 MeV 45°, 0°, 22.5°, 67.5° incidence [2,2,0,2,2] | 8218-13-9 |
| | | 10 | 100 MeV [2 krad] | 8218-16-50 |

IMO ≡ inverted mode operation (ie. MPP)

All proton irradiations:- not powered. Dose regions across chip indicated: [x,x,x,x] with x = dose in krad(Si)

Co$^{60}$ irradiations 1.73 krad/hr
2, 4 krad(Si)

$Co^{60}$ 1.73 krad/hr 1, 2, 4 krad(Si)

| | | | |
|---|---|---|---|
| 1 | CCD02-06-5-206 | Back illum | Powered |
| 2 | CCD02-06-5-202 | Standard, no store shield | Not powered |
| 1 | CCD05-20-5-202 | " | Powered |
| 1 | CCD05-20-5-202 | " | Not powered |

10 MeV Protons, Not powered

| | | |
|---|---|---|
| 1 | CCD-05-20-5-202 | Standard 10 MeV [4102] |
| 1 | CCD-05-20-5-222 | 100Ωcm 10 MeV [4102] |
| 1 | CCD-02-06-5-206 | Back Illum 10 MeV [4002] |
| 1 | CCD-02-06-5-202 | Standard 10 MeV [4002] |
| 1 | CCD-02-06-5-219 | IMO 10 MeV [4102] |
| 1 | CCD-02-06-5-019 | Standard (SS) 10 MeV [4102] |
| 1 | CCD-02-06-5-019 | Standard (SS) 10 MeV [22022] 45°, 0°, 22.5°, 67.5° incidence |

100 MeV Protons, Not powered

| | |
|---|---|
| 1 | CCD02-06-5-219 |
| 1 | CCD02-06-5-019 |

The proton irradiations were carried out in up to three stages (depending on the dose regions required). For example, one half of the CCD area was masked by a 1mm thick aluminium plate as shown below:

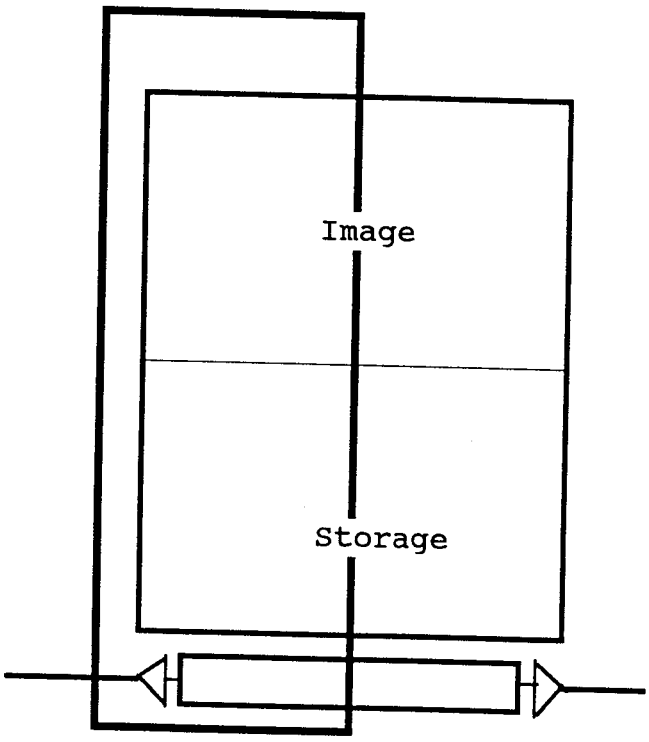

the device was then irradiated to a proton fluence calculated to give an ionising dose of 1 krad(Si), ie:

$1.79 \times 10^9$ p/cm$^2$ at 10 MeV

In step two the aluminium mask was moved to the centre of the CCD:

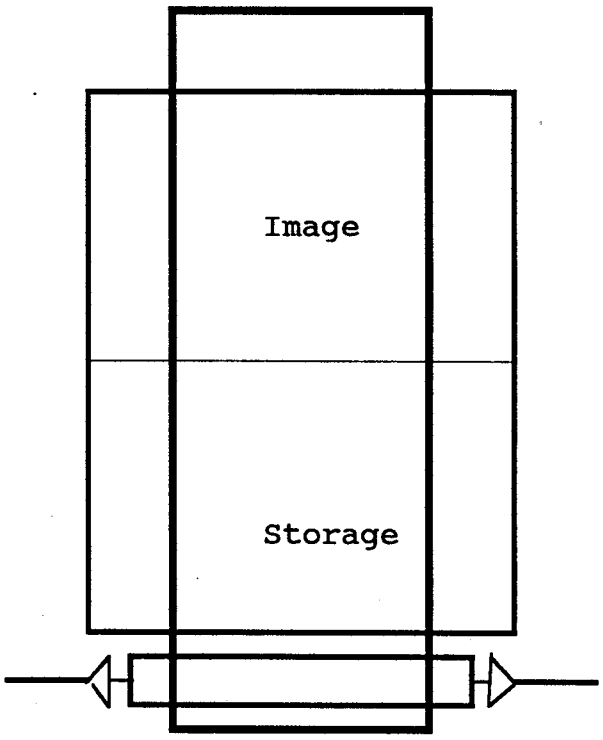


The CCDs were then irradiated so as to give an additional 3 krad(Si) of total ionising dose ie:

$5.37 \times 10^9$ p/cm$^2$ at 10 MeV

In the final step only the right hand quarter of the chip was irradiated to another 1 krad(Si).

In this way four zones with different accumulated doses (for example 0, 1, 2 and 4 krad) could be produced on each CCD as illustrated in figure 2.4-1. Note that the output node received the maximum dose of 4 krad(Si). Typical exposure times were ~2 minutes. The irradiations were carried out at room temperature. Electrical measurements were made before and immediately after each dose step and after unbiased storage at room temperature at Sira.

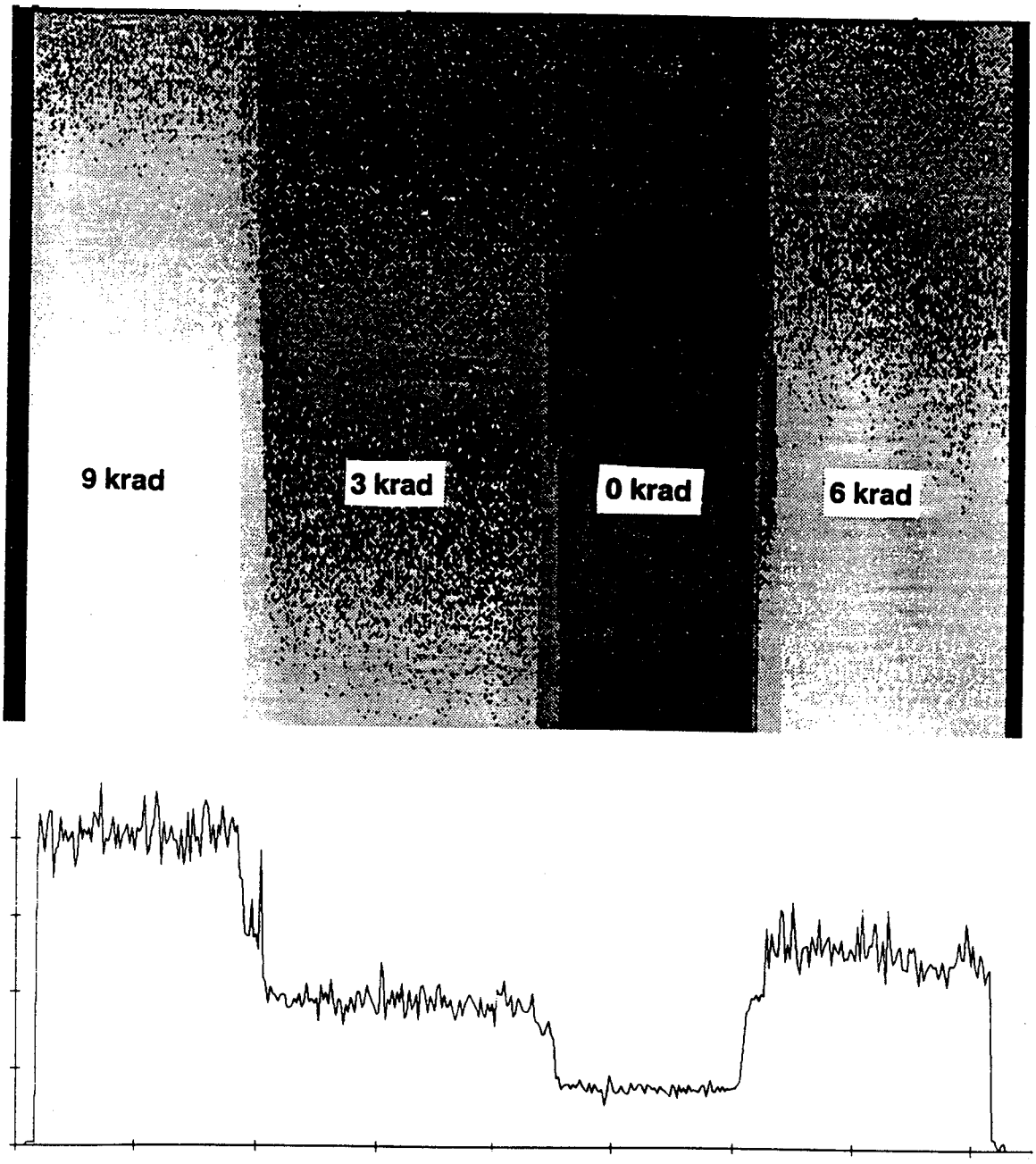


**Figure 2.4-1 CCD image and line trace showing the four dose regions(in this case 0, 3, 6 and 9 krad)**

# 3. IONIZATION DAMAGE

## 3.1 Shifts in Operating Biases

Use of the DAC controlled camera head allowed assessment of the effect of alteration of CCD biases. In particular, changes of signal and offset (overscanned pixel or porch) voltage with respect to $V_{RD}$, $V_{SS}$ and $V_{OG}$ (cf. section 2.3) can indicate shifts in flatband voltage. In addition, the current in the off-chip resistive load ($I_{DD}$) is related to shifts in the average DC level of the output signal.

### 3.1.1 $I_{DD}$ Measurements

Table 3.1.1-1, below, gives $I_{DD}$ currents before irradiation and at various times afterwards. It can be seen that the change for devices 12 and 15 is small or zero: this is because the edge of the proton beam missed the corners of the (large area) CCDs and so the output amplifiers received little or no dose. The change for 03 is also small because this device was back illuminated through the full thickness (~600μm) of the silicon wafer - which is unthinned at the edges. Note that only the cobalt60 irradiated devices were measured after 2 krad and 4 krad. The proton damaged devices received 4 krad at the output amplifier. The changes in current ($\Delta I_{DD}$) are given in table 3.1.1-2.

**Table 3.1.1-1 $I_{DD}$ Currents (mA), 10k load**

| Device number | Type | Irradiation | Pre-irradiation | 2 krad immediate | 4 krad immediate | 4 krad after 3 months |
|---|---|---|---|---|---|---|
| 01 | IMO | Proton | 1.976 | - | - | 1.986 |
| 02 | IMO | Proton | 1.983 | - | - | - |
| 03 | BI | Proton | 2.181 | 2.183 | - | 2.184 |
| 04 | BI | P | 2.113 | 2.135 | 2.156 | 2.156 |
| 05 | | Proton | 2.129 | - | 2.139 | 2.137 |
| 06 | | U | | 2.145 | 2.151 | 2.151 |
| 07 | | U | 2.127 | 2.135 | 2.140 | 2.141 |
| 08 | | Proton | 1.910 | - | 1.918 | 1.917 |
| 09 | | Proton | 1.912 | 1.925 | - | 1.923 |
| 10 | | Proton | 1.929 | - | - | 1.936 |
| 12 | CCD05 | Proton | 2.268 | - | 2.268 | - |
| 13 | CCD05 | P | 2.227 | 2.250 | 2.283 | 2.267 |
| 14 | CCD05 | U | 2.223 | 2.231 | 2.237 | 2.235 |
| 15 | CCD05 | Proton | 2.060 | - | 2.059 | - |

IMO } Inverted Mode Operation
Proton } 10 MeV proton, unpowered
BI } back illuminated

P } cobalt60 powered
U } cobalt60 unpowered

**Table 3.1.1-2 $\Delta I_{DD}$(mA)**

| Device | Condition | 2 krad | 4 krad | Approximate Δ per krad |
|---|---|---|---|---|
| 04 | $Co^{60}$ powered | 0.022 | 0.043 | 0.011 |
| 13 | " | 0.023 | 0.040 | 0.010 |
| 06 | $Co^{60}$ unpowered | 0.006 | - | 0.003 |
| 07 | " | 0.008 | 0.013 | 0.004 |
| 14 | " | 0.008 | 0.014 | 0.004 |
| 01 | Proton, unpowered | - | 0.01 | 0.0025 |
| 02 | " (100 MeV) | 0.0055 (1 krad) | - | 0.0055 |
| 05 | " | - | 0.01 | 0.0025 |
| 08 | " | - | 0.007 | 0.0017 |
| 09* | " | 0.011 | - | 0.004 |
| 10 | " (100 MeV) | 0.007 | - | 0.0035 |

* dose = 2 x $\sqrt{2}$ = 2.83 krad

It is seen that for cobalt 60 irradiation we have:

$\Delta I_{DD}$, powered devices ~0.01mA/krad
$\Delta I_{DD}$, unpowered devices ~0.004mA/krad

Since the load resistor was 10.0kΩ these correspond to voltage changes of 0.1V/krad and 0.04V/krad. Note however that there will be a contribution to $\Delta I_{DD}$ from increased leakage currents and the above values are probably overestimates of the flatband voltage shift in the output amplifier (ie. in the gate oxide of the source follower amplifier). (It would probably be advisable in future measurements to also monitor the output voltage with an oscilloscope.

For the 10 MeV proton irradiations there is a suggestion that the shift is slightly less: on average down by a factor ~40%. This is presumably because of the increased recombination for low energy proton tracks [13]. The difference is less than the factor 2 found for dark current in Thomson-CSF CCDs [10], but this may be due to differences in electric field strength. Reasons why the damage is worse for powered devices, even when the field is negative and drives radiation generated holes towards the gate electrode were discussed in [10]. A possible reason is the effect of the ion implantation (in forming the buried channel). In Thomson-CSF CCDs the field is in fact likely to be positive in the locos channel stop region [14] thus explaining the previous results (in ref [10]).

However EEV devices do not have a locos channel stop technology and so the field is likely to be negative (though possibly not well defined in an unpowered device).

It is interesting to note the large $I_{DD}$ shift for device 09. This received 2.8 krad at the output amplifier, but was irradiated at an angle of 45°. The end result was the same damage per krad as for $Co^{60}$ gamma rays. That irradiation at an angle with low energy protons gives results similar to those obtained with $Co^{60}$ gamma rays has previously been reported by Tallon et al [15] (note that the 2.8 krad figure arises because the proton fluence was increased to 5.06 x $10^9$ p/cm$^2$ to take into account the decreased effective area presented by a device at 45°, but the proton tracks in the oxide are $\sqrt{2}$ larger and so the energy deposited per gram (ie. the dose) is also larger by the same factor).

Note also that the shift for the two devices irradiated with 100 MeV protons is larger than at 10 MeV - as expected from the reduced e-h recombination at higher energies.

### 3.1.2 $V_{RD}$ Voltage Measurements

The CCD dark signal was measured as a function of the voltage on the reset drain transistor ($V_{RD}$). This voltage must be more positive than the potential under the output gate [11] and hence will increase with irradiation due to charge build up in the oxide under the output gate.

For the majority of devices the minimum value for $V_{RD}$ is roughly 15V (though CCD02 device 10 and CCD05 device 15 showed minimum values around 12V). The decrease in signal with decreasing $V_{RD}$ is sharp and can be used as an indicator of flatband shifts. Figure 3.1.2-1 shows results for device 13 (powered) and Figure 3.1.2-2 for device 04 (powered).

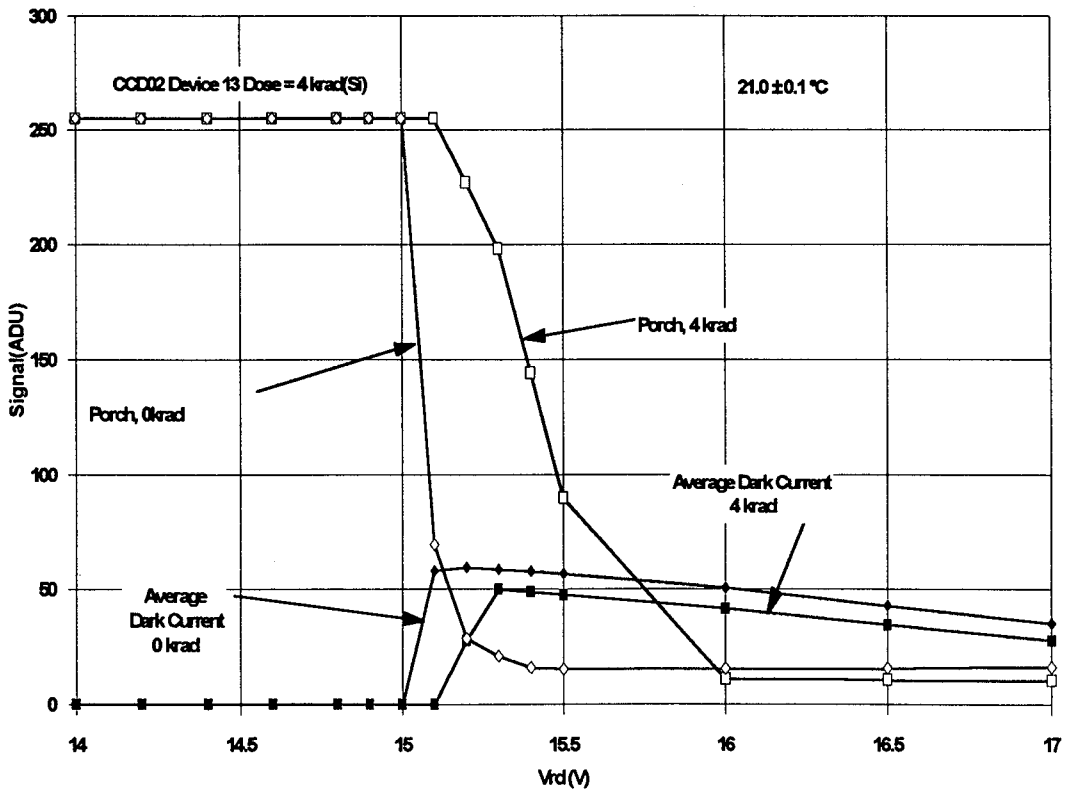


**Figure 3.1.2-1 Results for device 13, 1 ADU ≡ 74.5 μV**

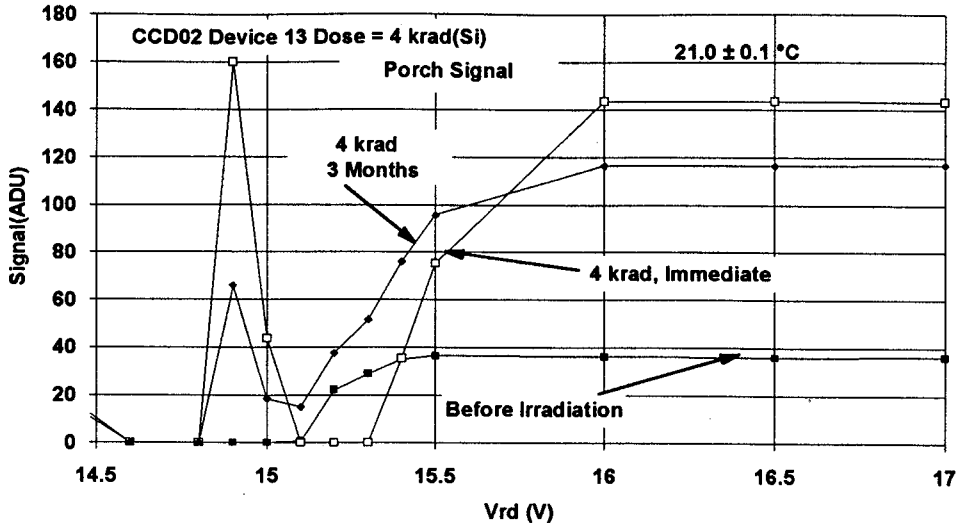


**Figure 3.1.2-2a Results for porch signal, 1ADU ≡ 74.5 μV**

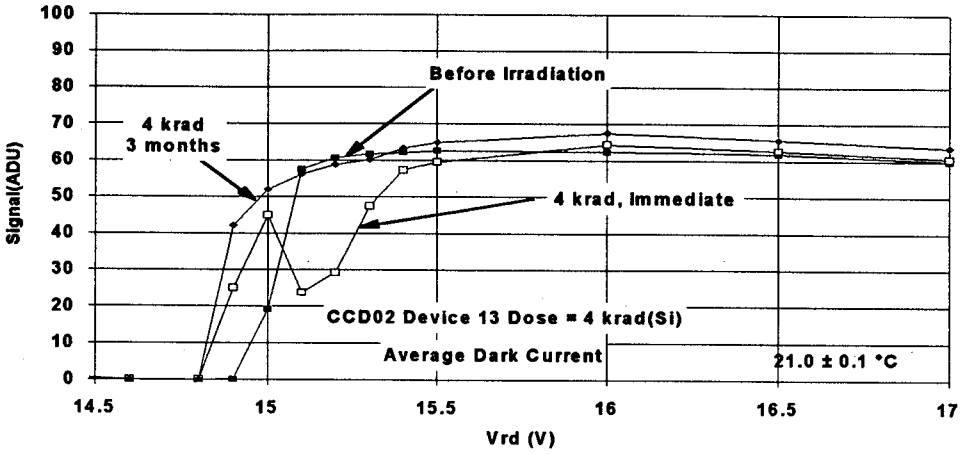


**Figure 3.1.2-2b Results for average dark voltage, 1ADU ≡ 74.5 μV**

In the former case the shift is approximately 0.05V/krad. For device 04 the shift is initially the same (0.2V after 4 krad) but then reduces, after a period of several weeks to 0.1V, thus indicating annealing behaviour: shifts for other (unpowered) devices are less:

| device | $V_{DR}$ shift/krad |
|---|---|
| 06 | 0.0125V |
| 07 | -0.0125V |
| 14 | 0.04V |

As a worst case figure we assume a shift of 0.05V/krad in line with previous measurements [16]. The indication from section 3.1.1 was also that devices not powered during irradiation are likely to show a smaller shift.

### 3.1.3 Measurements of Offset Voltage

The offset voltage is the CCD output signal (after correlated double sampling) for overclocked pixels - ie. pixels formed by artificially continuing the line readout after the 'useful' pixels have been readout. These overclocked pixels do not contain signal charge but there will be a difference between reset and video levels because of Rϕ3 clock breakthrough. This is because, in any feasible clocking scheme to be used for MERIS, sampling of the reset and video levels occurs when the readout register clocks are in different states (eg. Rϕ1 high, other phases low, during the video and Rϕ3 high, others low, during reset) For slower readout applications additional R clock transitions can be inserted so as to have identical Rϕ3 clock states for both samples of the output waveform thus ensuring that any feedthrough is the same for both samples and is cancelled by the correlated double sampling circuit. However the fast readout rate for MERIS precludes this possibility. The breakthrough is reduced by appropriate choice of output gate, and reset transistor biases ($V_{OG}$ and $V_{RD}$). It also varies with the exact pattern of the readout clocks.

The offset is sensitive to substrate voltage. For voltages below about 8V the offset changes little but above 8V can sharply increase or decrease depending on the value of $V_{OG}$, $V_{RD}$ and on the doping concentration of a particular device. Absolute values of offset voltage were not measured in this study but the relative variation with $V_{SS}$ was measured and found to vary with dose. Standard operating voltages for devices in this study were $V_{OG}$ = 1.19V and $V_{RD}$ = 15.5V however these were not always found to give the best performance after irradiation. The largest changes were for devices 04 and 13 (both powered during irradiation). Figure 3.1.3-1 shows the variation of the porch signal (offset) as a function of $V_{SS}$ before irradiation, 2 weeks after irradiation and 3 months after irradiation. Note that the plots have been adjusted vertically so that the offsets are the same for $V_{SS}$ = 4V (absolute values could not be measured as the offset in the off-chip electronics was changed in-between stages). This seems reasonable since measurements after 3 months for various $V_{OG}$ do coincide for low values of $V_{SS}$.

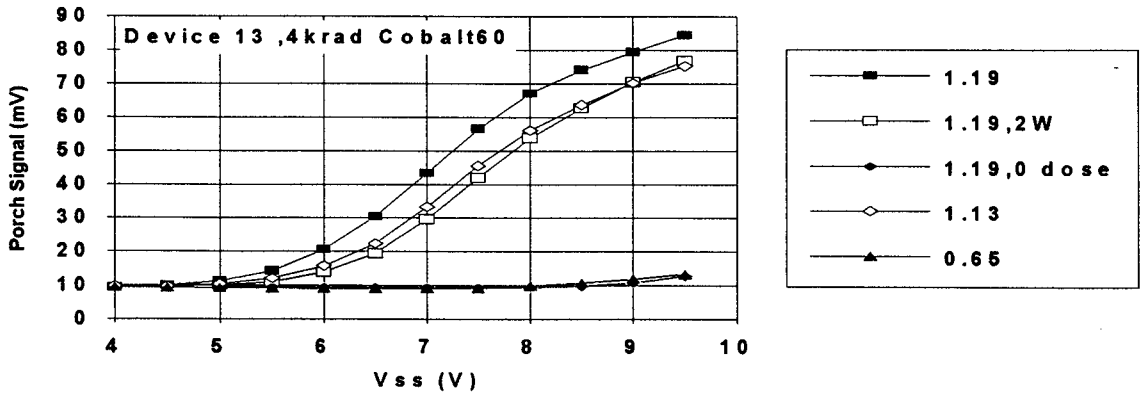


**Figure 3.1.3-1**

It is seen that there is a large difference in the shape of some of the curves. However the plots at 2 weeks and pre-irradiation could be approximated by measurements at 3 months by varying $V_{OG}$ by 0.06V (1.19 changed to 1.13V) and 0.54V (1.19 changed to 0.65V respectively). These shifts will be related to flatband shifts in the output circuit but the relationship with clock breakthrough may be complex. Figure 3.1.3-2 shows porch signals for a larger number of $V_{OG}$ voltages.

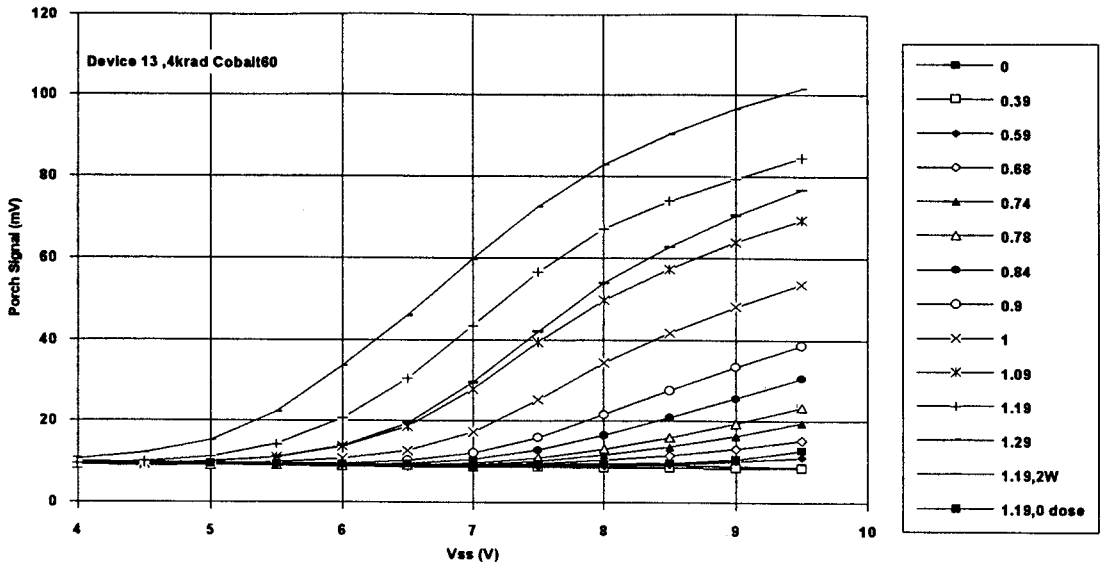


**Figure 3.1.3-2 Porch signal versus $V_{SS}$ for various Vog. Unless stated otherwise (in legend) measurements were made 3 months after irradiation.**

In contrast, Figure 3.1.3-3 shows porch signals after 3 months for device 04 for $V_{OG}$ = 1.19V and 1.6V ($V_{RD}$ = 15.5V in both cases). There is a vertical shift but little change in shape. However if $V_{RD}$ is increased to 16V the sensitivity to $V_{SS}$ is much reduced (figure 3.1.3-4), and is no longer sensitive to $V_{OG}$ (figure 3.1.3-5). The sequence shown in figure 3.1.3-6 ($V_{RD}$ = 15.5V) shows that the change after 2 weeks is the largest and is reduced after 3 months (cf. figure 3.1.3-1 which shows the change in offset steadily increasing for device 13).

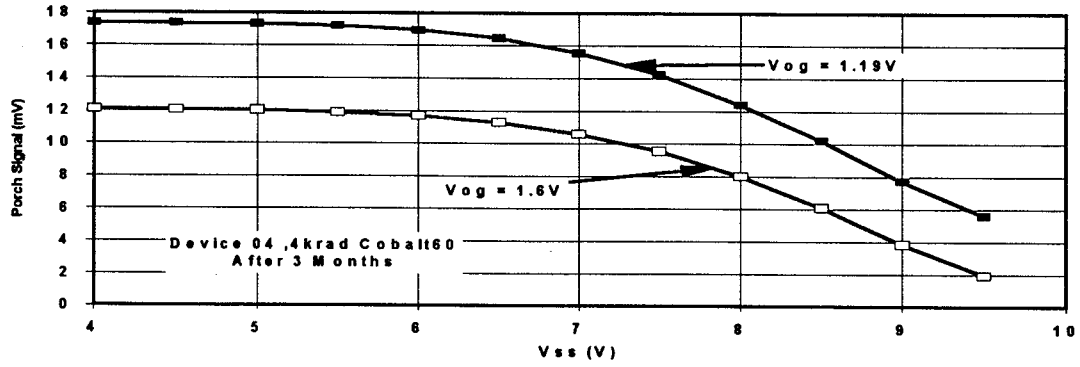


**Figure 3.1.3-3 Porch signal versus $V_{SS}$ for various $V_{OG}$. $V_{RD}$ = 15.5V.**

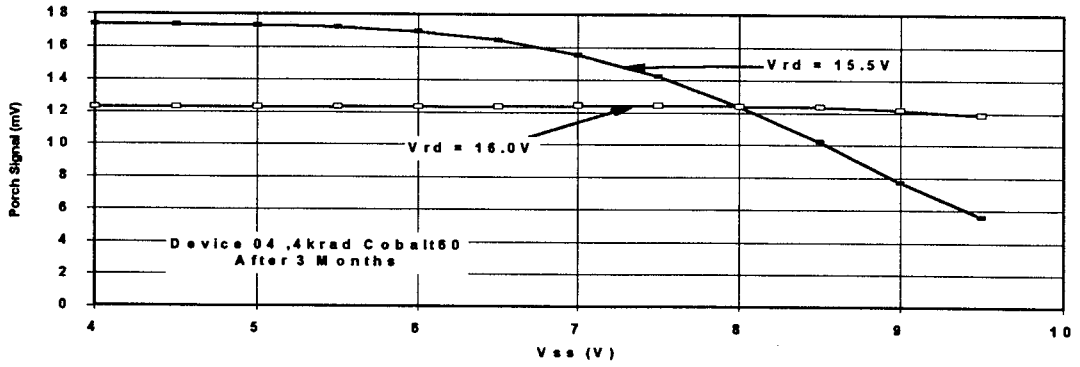


**Figure 3.1.3-4 Porch signal versus $V_{SS}$ for various $V_{RD}$. $V_{OG}$= 1.19V.**

**A/9119/00**

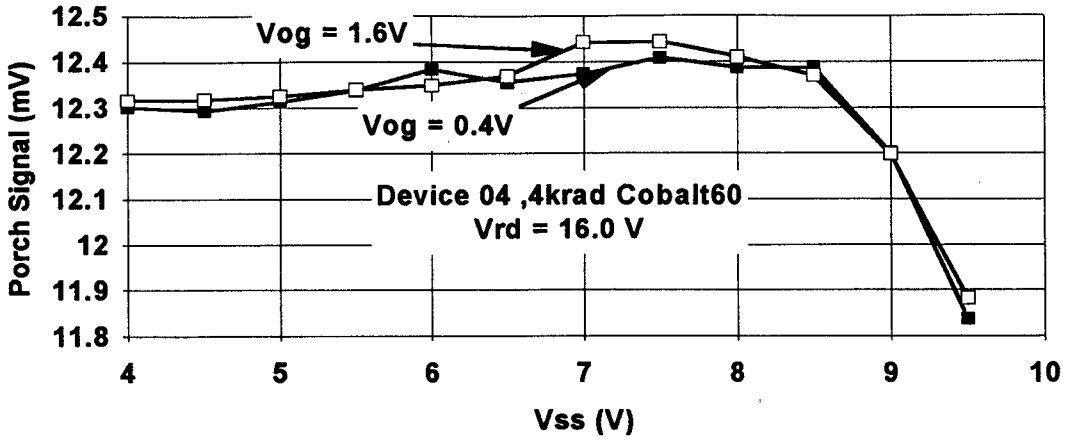


**Figure 3.1.3-5 Porch signal versus $V_{SS}$ for various $V_{OG}$. $V_{RD}$ = 16.0V.**

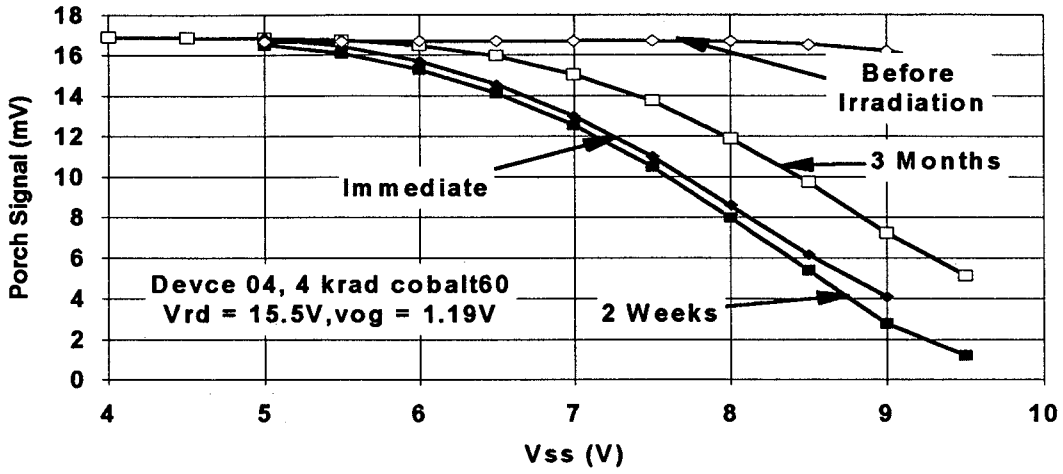


**Figure 3.1.3-6 Rebound effects in device 04.**

Device 06 displays a different characteristic in that the variation of the offset voltage is reduced by increasing $V_{OG}$ (rather than by decreasing it to near zero volts as for device 13), cf. figure 3.1.3-7. With this device the best performance is achieved with $V_{OG}$ = 1.6V and $V_{RD}$ = 15.5V

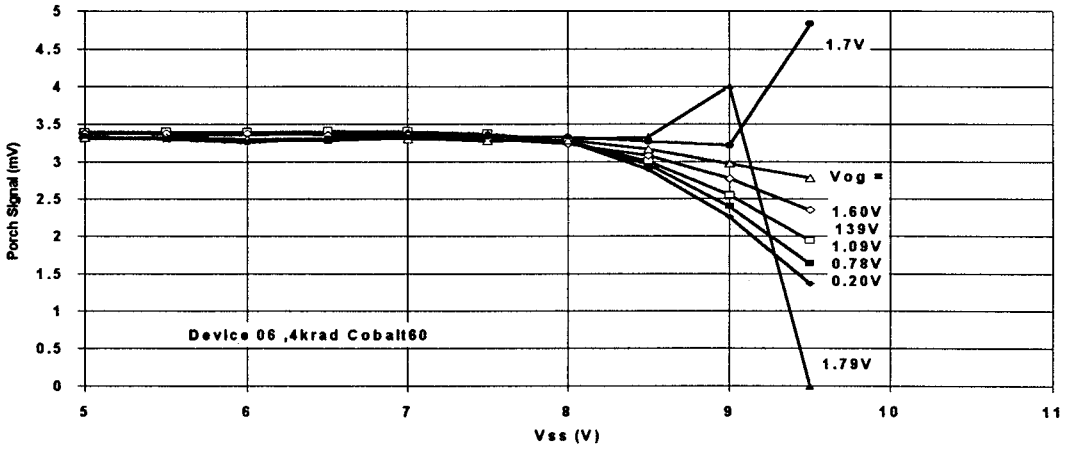


**Figure 3.1.3-7 Porch signal versus $V_{SS}$ for various $V_{OG}$. $V_{RD}$ = 16.0V.**

**A/9119/00**

Device 07 comes from the same wafer as 06 and was irradiated under the same conditions (cobalt 60, not powered). However in this case $V_{RD}$ = 16V gives the best performance and thereafter changes in $V_{OG}$ have no effect (figure 3.1.3-8) - as for device 04.

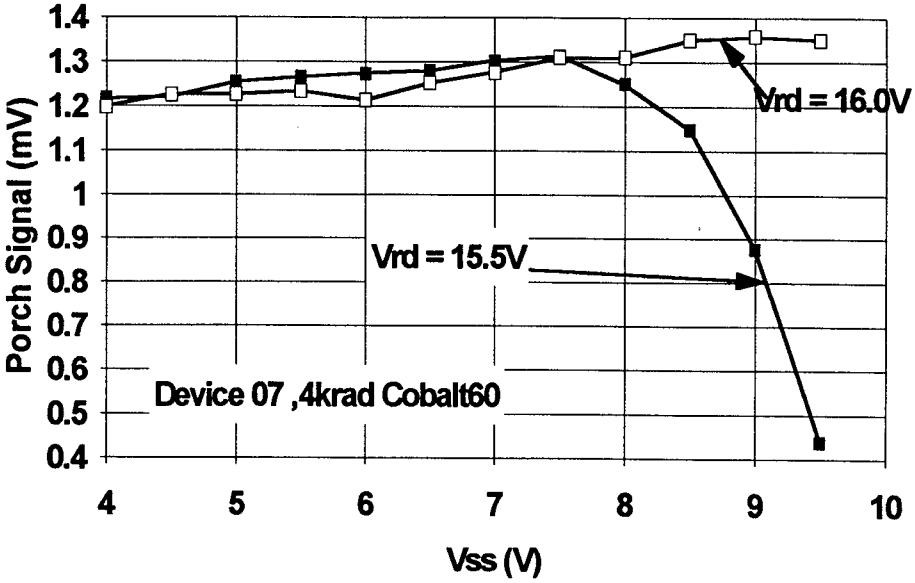


**Figure 3.1.3-8 Porch signal versus $V_{SS}$ for various $V_{RD}$. $V_{OG}$= 1.19V**

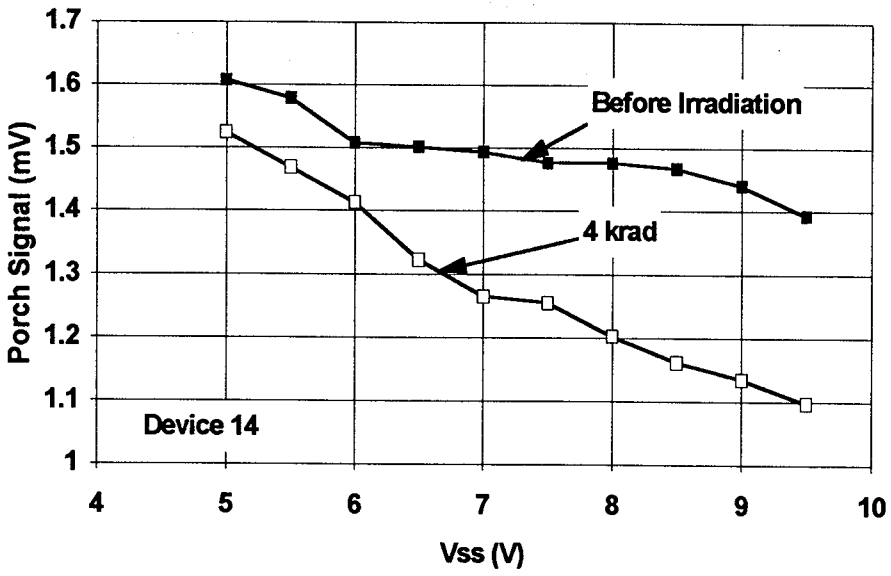


**Figure 3.1.3-9 Porch signal versus $V_{SS}$.**

Recall that device 13, which is a CCD05 with 780x1152 pixels, is the only device where the porch signal increases as $V_{SS}$ increases. This may be due to differences in design - the layout of the output gate is different in the two devices (CCD02 and CCD05), but figure 3.1.3-9 shows results for device 14 which illustrate behaviour for a CCD05 which is similar to the CCD02s. The remaining devices (bombarded by protons) showed small changes in porch signal, such as given in figure 3.1.3-10 for device 08.

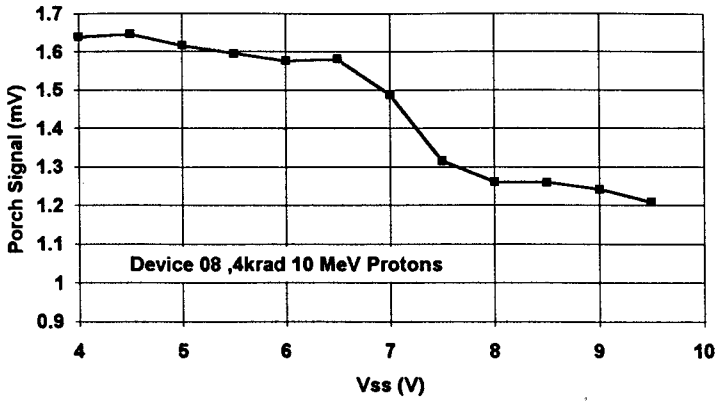


**Figure 3.1.3-10 Porch signal versus $V_{SS}$.**

In summary we conclude that large changes in offset signal can be caused by radiation, especially if the operating point is with $V_{SS}$ greater than 8V (as would be the case for operating the surface in inversion). Appropriate choice of $V_{OG}$ and $V_{RD}$ should however minimise the effects. There is a confusing variety of behaviour with the devices studied here but we note that these come from several batches widely spread in date code. It can be expected that flight devices will show a more uniform behaviour which can be studied by measurements during future radiation evaluations (eg. radiation LAT). Absolute shifts in porch signal were not measured here because of difficulties with offset stability of the off-chip electronics over long periods of time and because the 8 bit system used did not have sufficient dynamic range to accommodate a range of operating conditions without introducing an offset within the off-chip electronics. However measurements of offset will be important during future evaluations. The use of a 12 bit system and care to use control devices to keep a check on offset stability of off-chip electronics should be sufficient to ensure accurate measurements in future.

There are trade-offs with CCD output transistor gain (ie. charge to voltage conversion factor) in setting the optimum values of $V_{OG}$ and $V_{RD}$, but it is to be expected that optimum values can be derived during the future radiation evaluations. A design change to the CCD05 has been made which should decrease the clock breakthrough and reduce effects for flight devices. This involves an increase to the length of the output gate (at the expense of a slight reduction in operating speed - which should not be noticeable at MERIS readout rates, ~1MHz/pixel). With these precautions (design change and measurements during radiation LAT) it is expected that radiation - induced changes in offset would be less than ±0.5mV. At this level the effect on system performance should be small: at maximum gain (ie. worst case) the full range (ADC) signals will be ~200,000 electrons (assuming $2.25 \times 10^6$ CCD amplifier saturation and x10 maximum gain) ie. ~100mV. That is the offset shift is less than 1% of the ADC range. However it could be that the shifts for flight devices are larger - say ±5mV (ie. 10% ADC range at maximum gain) and this will not be known until relatively late in the programme (when representative devices are available). If these offset changes are considered unacceptable then an option is to have a DAC controlled offset stage within the CDS amplifier in the APU (analogue processing unit).

Note that there will in any case be offset changes due to radiation-induced dark current increases (section 3.2).

If the CCDs are operated at 20°C then approximate dark signals are given in table 3.1.3-1 below (were we anticipate results from section 3.2).

**Table 3.1.3-1 Average Dark Currents**

| | $nA/cm^2$ | electrons/pixel | electrons/pixel, 2x2 binning |
|---|---|---|---|
| non-inverted | | | |
| Beginning of life | 2 | 2400 | 9600 |
| End of life (4 krad) | 6 | 7200 | 28800 |
| inverted (and dithered) | | | |
| Beginning of life | 0.5 | 600 | 2400 |
| End of life | 2.5 | 3000 | 12000 |

If we take a nominal conversion factor of 0.7μV/electron then it can be seen that for 2x2 pixel binning the increase in CCD voltage can be as large as 20mV (non-inverted) at 20°C. Even for inverted operation the figure is 8.4mV. These shifts are likely to be greater than the porch offsets. The offsets can be reduced using a DAC offset stage (as above) or by reducing the CCD operating temperature. Note that table 3.1.3-1 above is for average dark current (ie. at the centre of the image). For the last line readout the dark current can be up to a factor 1.3 higher due to the increased dark current from the storage region.

Note: Offset voltage shifts have not been measured in previous known CCD radiation test programmes and it is not known how much other projects will be affected. However any instrument which relies on a critical setting of the ADC range may experience changes in dynamic range with radiation.

### 3.1.4 Dark Signal Versus $V_{SS}$

One way of detecting flatband voltage shifts for the CCD electrodes is to measure the change in output signal with substrate voltage ($V_{SS}$) as shown in figure 3.1.4-1. The change to surface inversion conditions occurs at ~7 V for this CCD(09). As the flatband voltage changes with irradiation this transition voltage will increase [16] (note that, strictly speaking it is the CCD current $I_{RD}$ which should be measured - or the output signal allowing for changes in charge to voltage conversion factor, section 3.1.5). In practise it was found that for the radiation levels used (4 krad) the shifts were too small to measure - especially as the shape of the $V_{SS}$ curve changed (became less sharp) with irradiation.

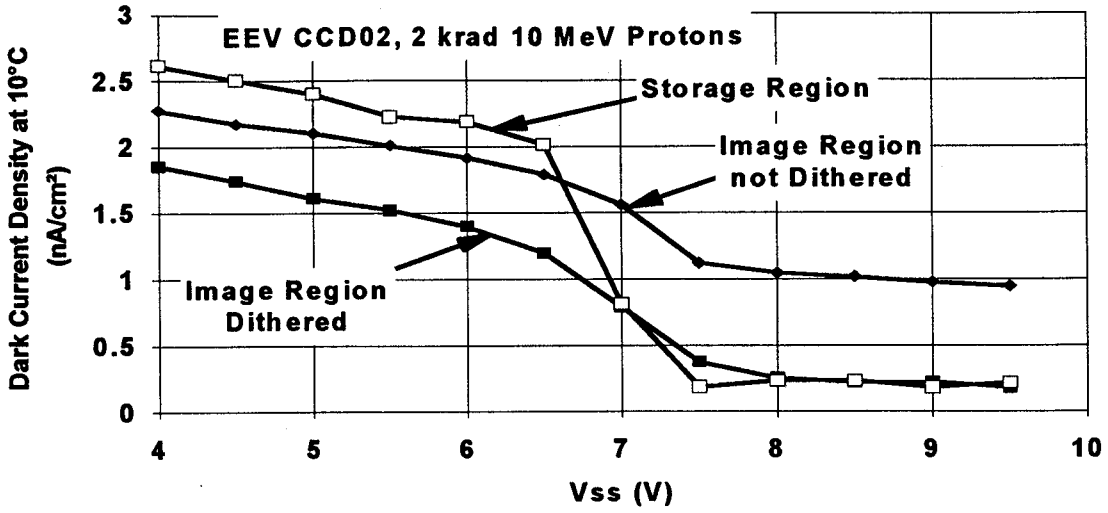


**Figure 3.1.4-1 Dark signal versus $V_{SS}$ for a typical device**

3.1.5 Changes in Charge to Voltage Conversion Factor (CVF)

Flatband shifts in the output amplifier can cause shifts in the operating point and hence changes in gain (and charge to voltage conversion factor, CVF). CVF was measured by recording the CCD output voltage for a given current in the reset transistor bias line ($I_{RD}$). In one device (15) which gave good quality x-ray calibration signals (from a $Cd^{109}$ soft x-ray source) both I/V and x-ray measurements were compared, with good agreement (1.0μV/e compared with 0.96μV/e, respectively). Table 3.1.5-1 shows the values of CVF before and after irradiation.

**Table 3.1.5-1 Values of CVF (in μV/electron) by the I/V Technique, $V_{SS}$ = 7.5V**

| | | after irradiation (4 krad) | | |
|---|---|---|---|---|
| **Device** | **Before irradiation** | **immediate** | **2 weeks** | **3 months** |
| 01 | 0.89 | - | 0.86 | - |
| 02 | - | - | - | 0.70 |
| 03 | - | - | - | 0.71 |
| 04 | 0.75 | 0.60 | 0.68 | 0.68 |
| 05 | 0.89 | - | - | 0.83 |
| 06 | 0.78 | 0.77 | 0.77 | 0.77 |
| 07 | 0.86 | 0.85 | 0.81 | 0.80 |
| 08 | 0.95 | 0.90 | 0.89 | 0.92 |
| 09 (2 krad) | 1.00 | 0.86 | 0.91 | 0.64 |
| 10 | 0.98 | - | 0.91 | - |
| 12* | 0.63 | - | 0.63 | - |
| 13 | 0.61 | - | - | 0.54 |
| 14 | 0.69 | 0.68 | 0.69 | 0.69 |
| 15* | 1.02 | - | 1.03 | - |

* approximately 1 krad 10 MeV protons at output amplifier.

Apart from a somewhat anomalous measurement for device 09 after 3 months, the worst changes are for the two devices (04 and 13) which were irradiated with $Co^{60}$ whilst powered (though device 07 also gives a significant change). These changes can also be seen in relative measurements of CVF as a function of $V_{SS}$. Figure 3.1.5-1 shows curves for devices 04, 07 and 09 (normalised to 1 at $V_{SS}$ = 5V; or 4V in some cases). Note that gain changes will depend on the operating point chosen (values of $V_{SS}$, $V_{RD}$ and $V_{DD}$). Some devices eg. 09 do not change markedly with $V_{SS}$.

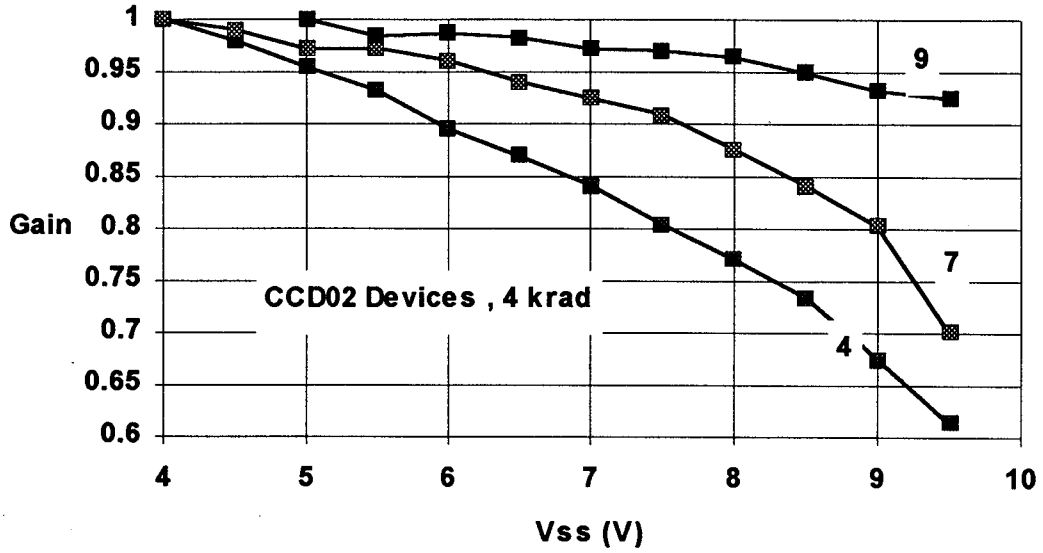


**Figure 3.1.5-1 Relative values of charge to voltage conversion factor for CCD02 devices.**

As a rough order of magnitude it seems that change of order ±5% (2 krad) or ±10% (4 krad) can be expected for powered devices; though a confirmation with more flight representative devices would be useful. If all six flight CCDs change in the same way then these changes can be compensated by changing the overall gain setting. If individual CCDs were to shift gain individually (which is possible depending on the spread in flatband voltage shift for flight CCD batches) then the facility to change the gains of individual CCDs may be needed. This can be achieved by incrementing (or decrementing) the gain switch command values for individual CCDs (provided the necessary hardware is implemented).

### 3.1.6 Summary

We conclude that threshold voltage shifts are worse for powered devices and amount to ~0.05V/krad. Sufficient margins on operating biases for flight devices should be chosen on the basis of radiation LAT results so as to minimise the effect on offset signal and CCD gain. Typical values after 4 krad might be:

| | |
|---|---|
| offset voltage change | ±0.5mV (but could be as much as a factor 10 higher) |
| gain change | ±10% |

We note, in general, that any CCD-based flight instrument which does not employ DAC controlled gains and offsets (or control of individual CCD biases) may suffer from loss in ADC dynamic range, though the implications will vary with application.

## 3.2 Changes in Dark Current

### 3.2.1 Magnitude of Dark Current Increases

In this section we discuss changes in surface dark current due to ionization damage (rather than bulk dark charge caused by displacement damage which is examined in Section 4). Table 3.2-1 below gives the average increase in dark current in $nA/cm^2$ per krad at 21°C for non-inverted conditions ($V_{SS}$ = 5V) and for conditions where the surface is inverted so as to suppress dark current generation. This is achieved by increasing the substrate voltage (to a value in the range 8 to 9.5V) so as to invert the surface under the clock low (0V) electrodes, and by using a technique we call dither clocking to switch the clock high phase periodically so as to invert the surface under the clock high electrode. The switch takes place for a time >40ns (the time needed for surface states to be filled) and the time between switches can be relatively long: of order 1ms, the emission time for the surface states. The technique is described more fully in reference [17] and will be further discussed later in this section. The dark current values in the table have been obtained by first using the appropriate charge to voltage conversion factor for each dose (or annealing) step as measured at 7.5V and then allowing for the change in gain in going to $V_{SS}$ = 5V or 9.5V (using gain versus $V_{SS}$ plots as given in section 3.1.5).

The dark current values in Table 3.2.1-1 are separated into the components from the image and storage regions (figure 3.2.1-1). These components are measured by taking an average of pixels for the first few lines readout (which contain only image region dark charge) and taking an average of those for the last few line readout (which contain both image and storage region components). The average dark current was measured at the centre of the images (and will differ only slightly from the mathematical value of image plus 0.5 times the storage component).

From the table we note:

i) In the cases where a comparison can be made between noninverted (ie. surface) dark current for devices irradiated with protons and $Co^{60}$ gamma rays, both unpowered (eg. comparing device 03 with 06 and 07 and 14 with 12 and 15) it can be seen that there is little difference ie. protons gave the same damage as $Co^{60}$. This is in contrast with the results for Thomson-CSF devices [10] where proton damage was down by a factor ~2. However it has to be said that in both cases the proton data possibly suffers from annealing and/or dose rate effects in that dark current for the different dose regions of proton damaged chips did not follow a strictly linear dependence with dose. This was discussed in [10] for Thomson devices and is illustrated in figures 3.2.1-2 (device 03), 3.2.1-3 (device 05) and 3.2.1-4 (device 08) and 3.2.1-5 (device 21). In fact the devices tested during this campaign (03, 05 and 08) show quite good linearity, apart possibly when inverted and dithered (where dark current can in any case show some slight large scale nonuniformities). Devices 21 and 22 where irradiated during the previous SILEX run. In any case the values chosen to calculate table 3.2.1-1 were for 2 krad (MERIS run) and 3 krad (SILEX run), which should be fairly representative and free from nonlinearity effects. The difference in behaviour compared with Thomson-CSF devices may be due to differences in the oxide field, since this affects the initial e-h recombination rate in the oxide.

## Table 3.2.1-1 Dark current (nA/cm$^2$ at 21°), After 3 months

| | | CCD02 | | | | | | | | | | | | CCD05 | | | |
|---|---|---|---|---|---|---|---|---|---|---|---|---|---|---|---|---|---|
| Device Number | | 01 | 02 | 03 | 04 | 05 | 06 | 07 | 08 | 09 | 10 | 21 | 22 | 12 | 13 | 14 | 15 |
| EEV Number | | A0451-62 | A0451-52 | A0658-47 | A0658-9 | A0354-44 | A0354-16 | A0354-036 | 8218-13 -27 | 8218-13 -9 | 8218-16 -50 | 8232-13 -7 | 8232-13 -9 | A0577- 19-10 | A0576- 18-12 | A0694-9 | A0693- |
| Description* | | IMO | IMO | BI | BI | | | | SS | SS | SS | | | | | | 100Ωcn |
| Irradiation* | | P10 | P100 | P10 | P | P10 | U | U | P10 | P10 | P100 | P10, U | P10, P | P10 | P | U | P10 |
| Non-inverted ($V_{SS}$ = 5V) | | | | | | | | | | | | | | | | | |
| Average | Pre-irradiation value | 1.28 | 1.51 | 2.4 | 1.64 | 1.3 | 1.79 | 1.62 | 1.38 | 1.31 | 1.64 | 2.01 | 2.42 | 1.32 | 1.29 | 1.29 | 1.09 |
| | increase/krad | 0.64 | - | 0.7 | 0.63 | 0.95 | 1.06 | 0.97 | 2.26 | 3.19 | 3.69 | 0.67 | 0.51 | 0.45 | 0.42 | 0.60 | 0.55 |
| Image | Pre-irradiation | 1.0 | - | 1.83 | 1.12 | 0.94 | 1.32 | | | | | 1.23 | 1.55 | 0.96 | 0.95 | 0.95 | 0.79 |
| | increase/krad | 0.5 | - | 0.57 | 0.52 | 0.76 | 0.85 | 0.77 | 1.38 | 1.9 | 2.43 | 0.46 | 0.3 | 0.35 | 0.38 | 0.51 | 0.49 |
| Storage | Pre-irradiation | 0.58 | - | 1.05 | 0.96 | 0.74 | 0.97 | 0.86 | 0.76 | 0.69 | 0.92 | 1.46 | 1.64 | 0.71 | 0.69 | 0.7 | 0.57 |
| | increase/krad | 0.31 | - | 0.24 | 0.08 | 0.41 | 0.43 | 0.39 | 2.0 | 2.7 | 2.6 | 0.49 | 0.4 | 0.06 | 0.1 | 0.17 | 0.16 |
| Inverted ($V_{SS}$ = 9.5V, dithered) | | | | | | | | | | | | | | | | | |
| Average | Pre-irradiation | 0.12 | - | 2.19 | 0.25 | 0.22 | - | 0.59 | 0.1 | 0.09 | - | 0.23 | 0.34 | 0.25 | 0.25 | 0.24 | 0.18 |
| | increase/krad | 0.3 | - | 0.49 | 0.21 | 0.34 | - | 0.31 | 0.44 | 0.53 | 0.65 | 0.20 | 0.24 | 0.24 | 0.25 | 0.16 | 0.24 |
| Image | Pre-irradiation | 0.01 | - | 1.52 | 0.16 | 0.19 | - | 0.39 | 0.08 | 0.02 | - | 0.11 | 0.17 | 0.19 | 0.15 | 0.17 | 0.11 |
| | increase/krad | 0.25 | - | 0.33 | 0.24 | 0.29 | - | 0.25 | 0.23 | 0.36 | 0.38 | 0.14 | 0.17 | 0.21 | 0.17 | 0.12 | 0.18 |
| Storage | Pre-irradiation | 0.17 | - | 0.73 | 0.11 | 0.1 | - | 0.39 | 0.06 | 0.08 | - | 0.15 | 0.19 | 0.20 | 0.22 | 0.17 | 0.12 |
| | increase/krad | 0.14 | - | 0.24 | 0.28 | 0.19 | - | 0.15 | 0.35 | 0.38 | 0.54 | 0.16 | 0.23 | 0.04 | 0.11 | 0.07 | 0.12 |

*IMO = Inverted mode operation
BI = Back illuminated
SS = Store shield
P = Cobalt 60, powered
U = Cobalt 60, unpowered
P10/P100 = Proton irradiation, 10/100 MeV - unpowered

Note: For 10 MeV proton irradiated samples the values include the displacement damage component ≃0.1 nA/cm$^2$ per krad.

Table 3.2.1-1 Dark current (nA/cm$^2$ at 21°C), after 3 months

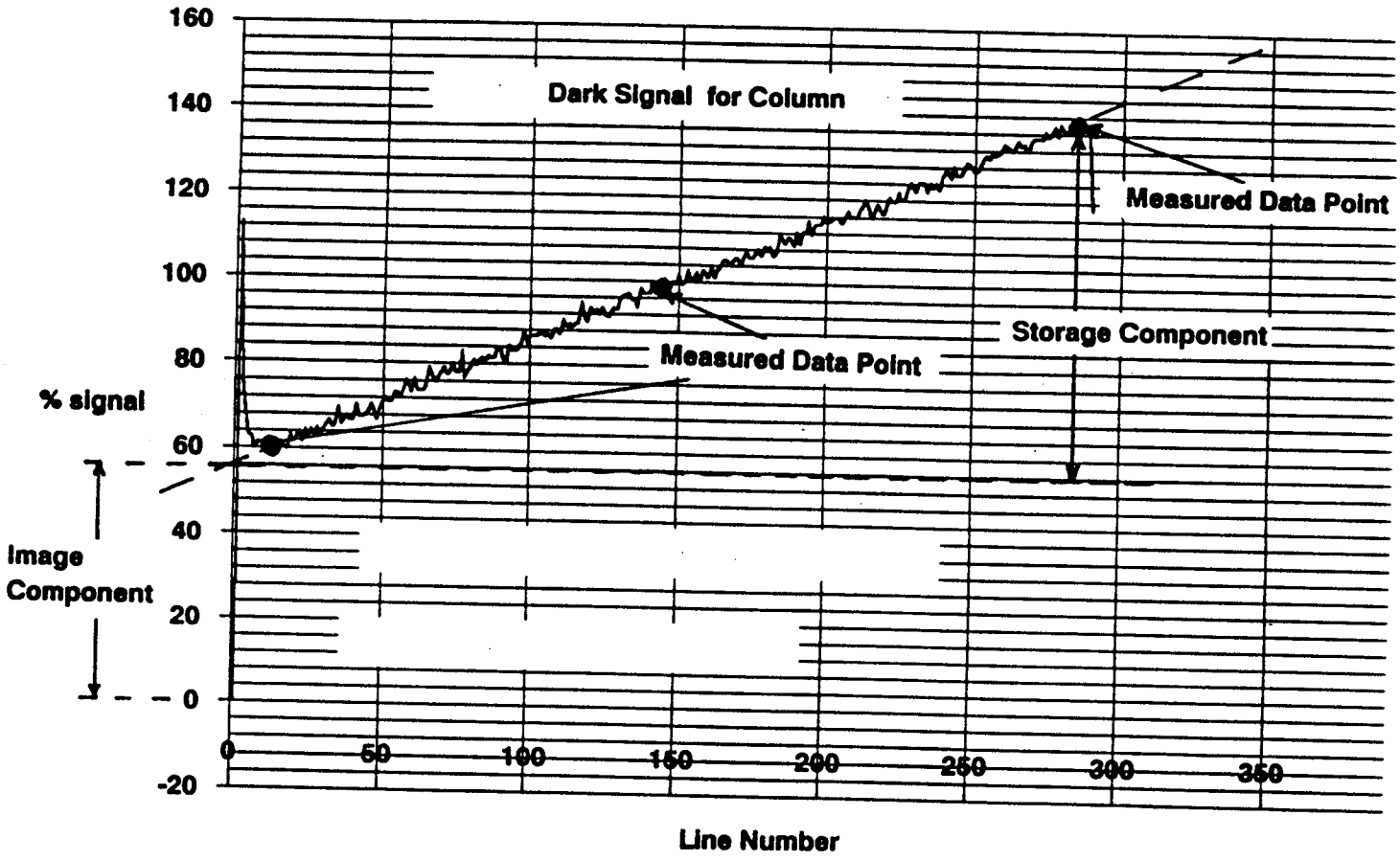


**Figure 3.2.1-1 Image and storage region dark current components**

A/9119/00

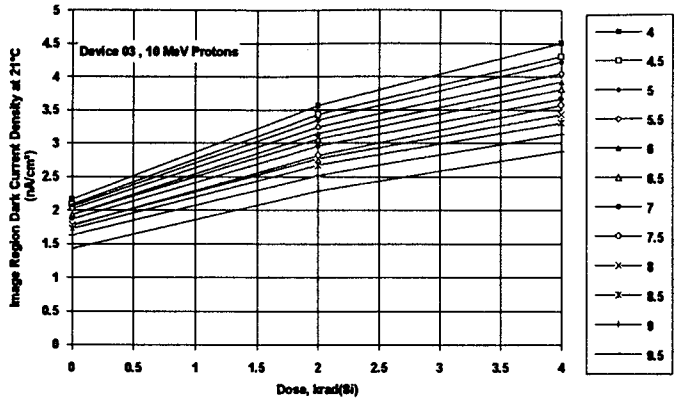


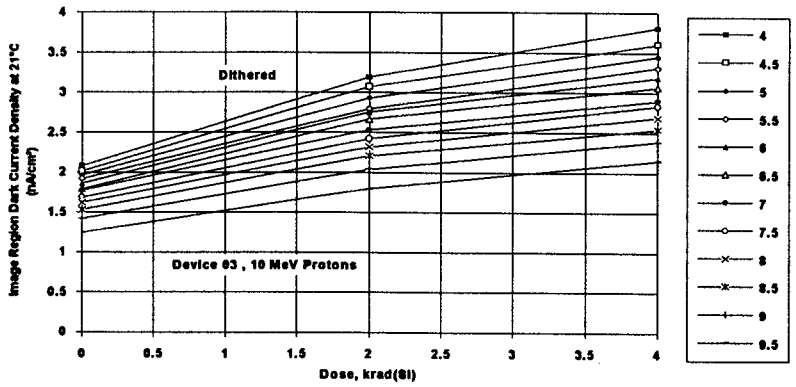


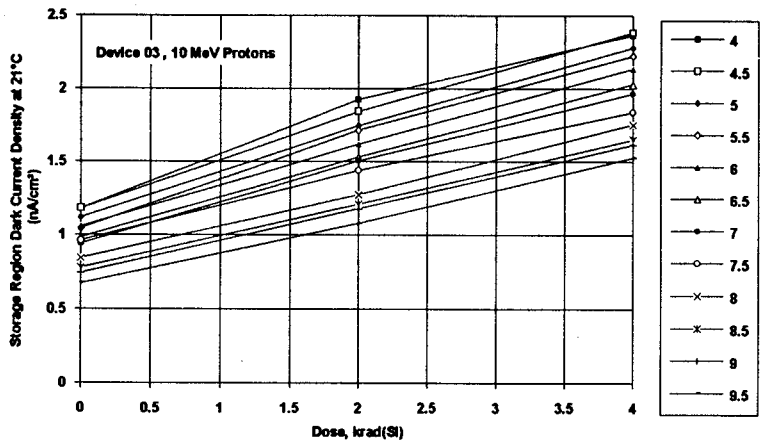


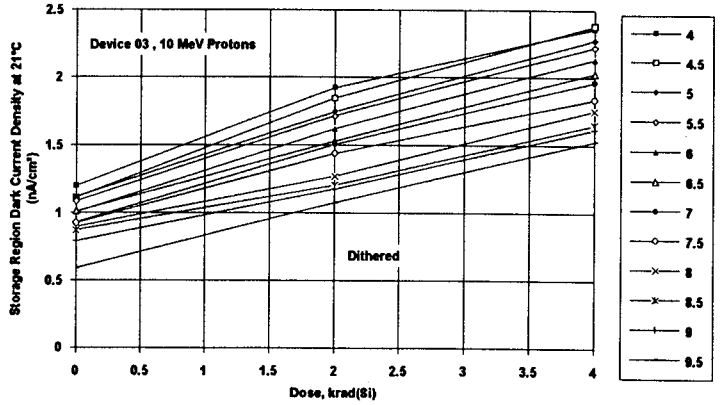


**Figure 3.2.1-2 Dark current for device 03 (10 MeV protons)**

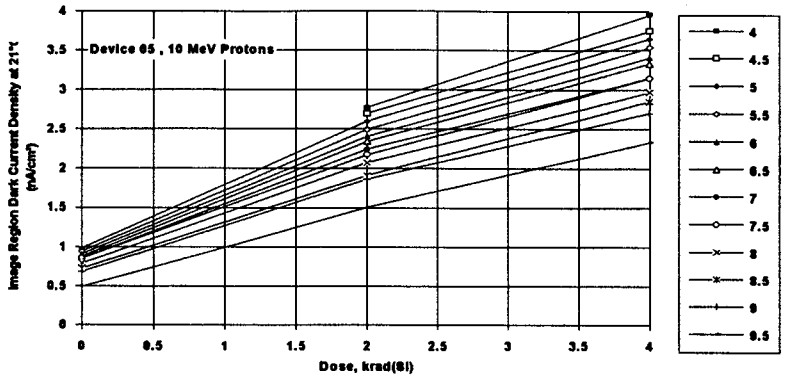


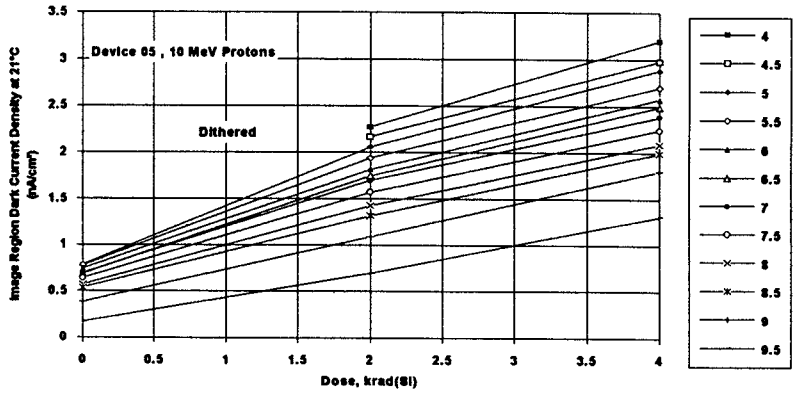


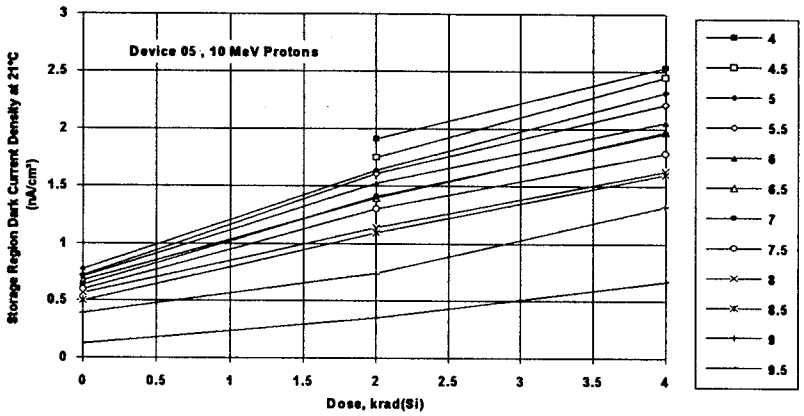


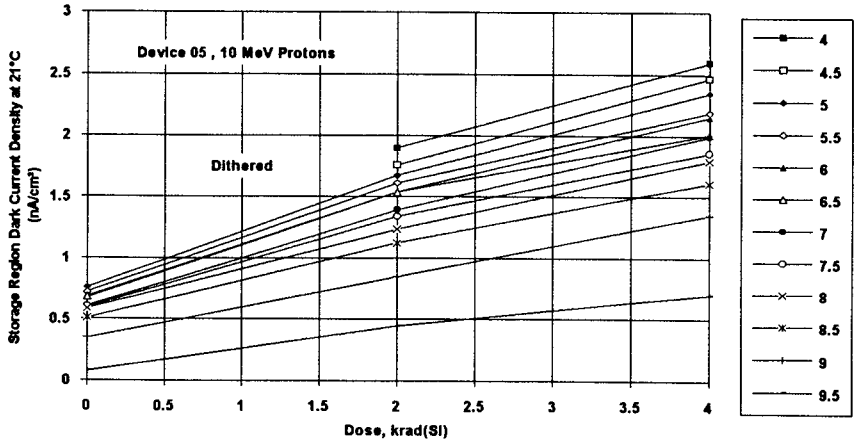


**Figure 3.2.1-3 Dark current for device 05 (10 MeV protons)**

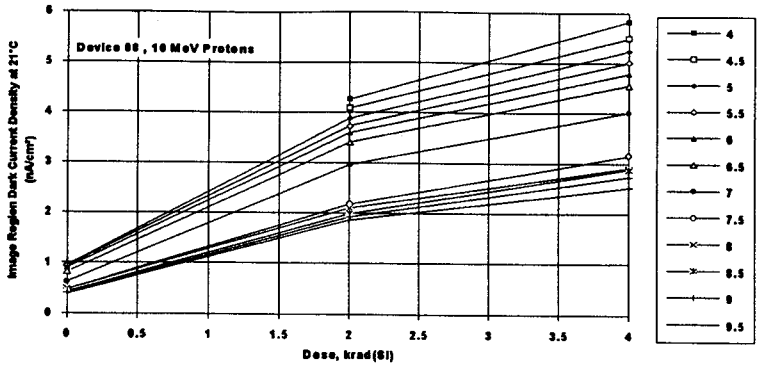


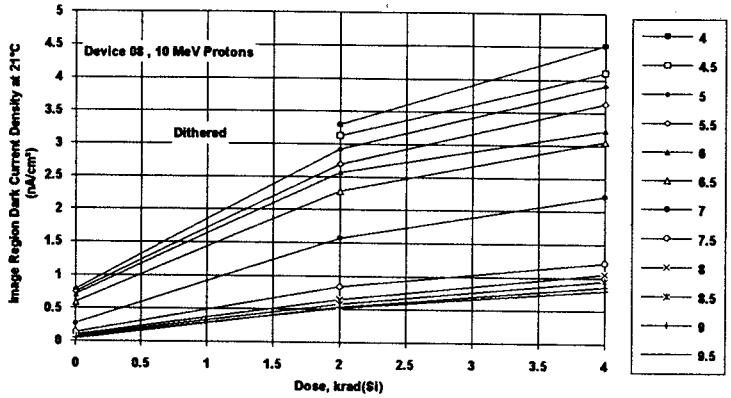


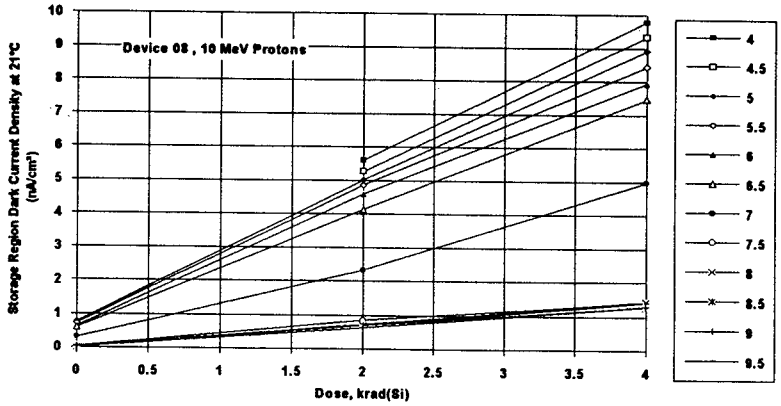


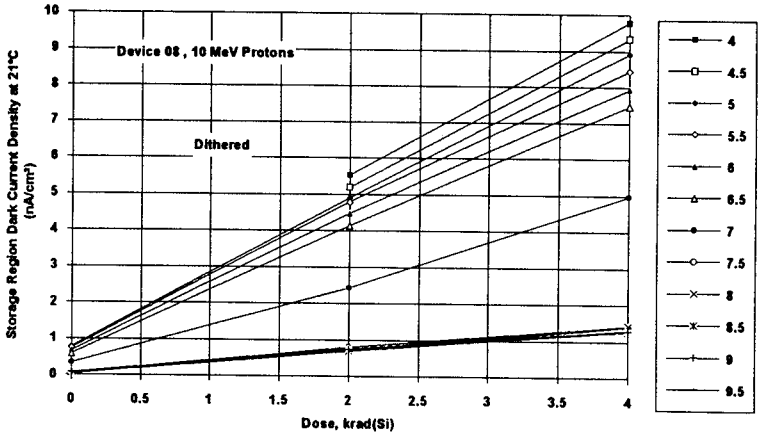


**Figure 3.2.1-4 Dark current for device 08 (10 MeV protons)**

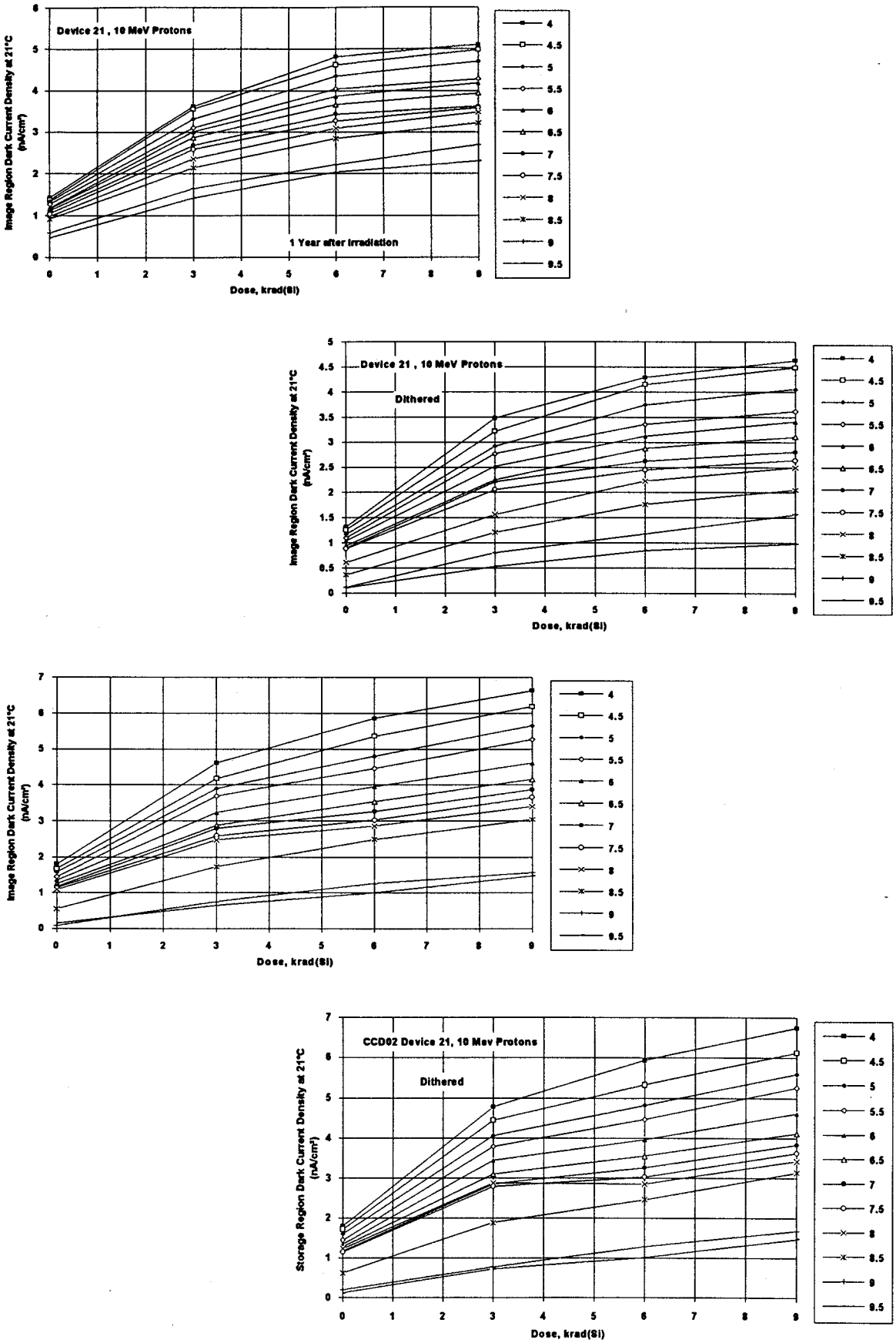


**Figure 3.2.1-5 Dark current for device 21 (10 MeV protons)**

**A/9119/00**

ii) Where a comparison can be made between biased and unbiased devices (04 and 03 - if protons are the same as $Co^{60}$ as in 1; 21 and 22 (protons); 13 and 14) it can be seen that the bias state makes little difference - if anything the dark current increases more (by ~20% more) for unpowered devices. Again the difference compared with Thomson devices may be due to the oxide field. Note that the dark current is mainly generated at the surface (proved by the fact that it is reduced when inverted) and so the damage must be caused by states at the Si/SiO2 interface.

In Thomson devices, it is likely that dark current arises in the 'birds beak' area of the channel stop locos oxide [18] which has 111 silicon and hence a high defect density [19]. EEV devices do not use the same channel stop technology - though it may still be true that dark current is still generated at the pixel edges. Although it can be said that in powered operation the field over the majority of the pixel area (excluding the periphery) is negative - ie. it drives radiation generated holes away from the oxide and towards the gate - and so minimises the damage; the fields when unpowered are undefined. In addition the fields at the pixel edges are positive for Thomson devices [18] but have not been modelled for EEV devices.

iii) Devices 08, 09 and 10 came from a batch of CCD02 devices with an aluminium mask (store shield) deposited over the storage region to shield it from light. The comparison with the other CCDs (which do not have store shields) is somewhat confusing in that 08, 09 and 10 show a generally higher rate of increase in dark current. However the increase for the storage region is particularly high and it is tentatively concluded that, as for Thomson CSF devices [10], having a store shield does increase the ionization induced surface dark current. Note that MERIS flight devices will be back illuminated and the store shield will be deposited onto the back surface and so would not be expected to have any effect on radiation performance.

iv) The reduction in dark current obtained by operating in inversion varied between devices, as can be seen from table 3.2.1-1. Further illustration is given in the plots shown in figure 3.2.1-6. (Note: these plots are not corrected for the small changes in amplifier gain with $V_{SS}$ - cf. section 3.1). When not using dither clocking, increasing $V_{SS}$ reduces the image area dark current by a factor 2-3 as would be expected since the area under two of the three phases will move into inversion. The storage region shows a larger decrease on moving into surface inversion because the action of clocking the region during CCD readout ensures inversion conditions under all phases. This condition is also achieved for the image areas when using dither clocking - in that case the image and storage generation rates are nearly equal.

The shapes of the VSS curves vary markedly between devices, with the sharpness of the transition and the voltage at which it occurs showing considerable variations. For example device 03 shows very little change in dark current whereas devices 08, 09 and 10 (from the same wafer) 12 and 15 show sharp transitions.

It can be seen that the dark current is not totally suppressed during full inversion and that it still increases after irradiation - such that the effectiveness of dither clocking is somewhat reduced. The reasons for this are not clear at this time (but see the discussion in section 3.2.5). It is believed that the dither clocking is as effective as it can be for the following reasons:

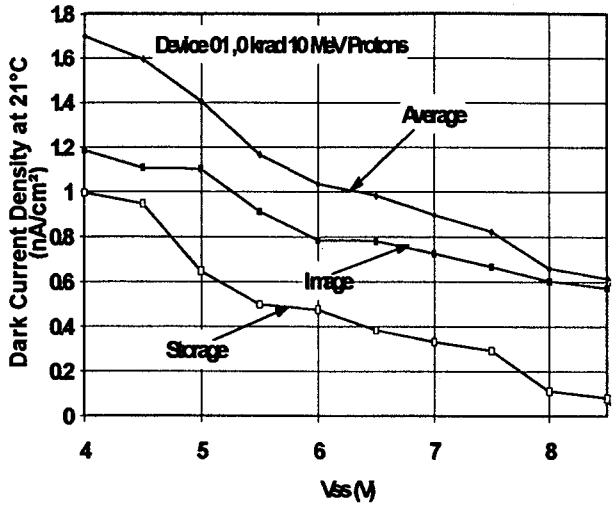


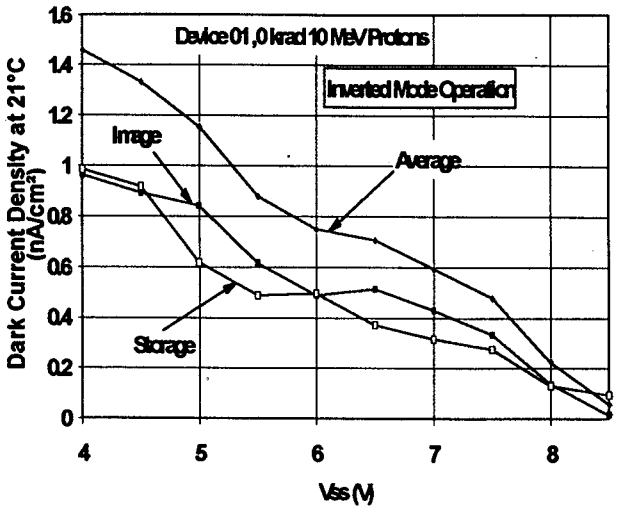


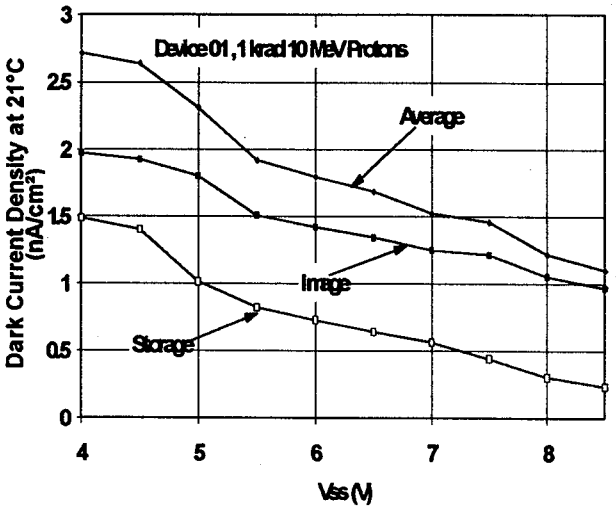


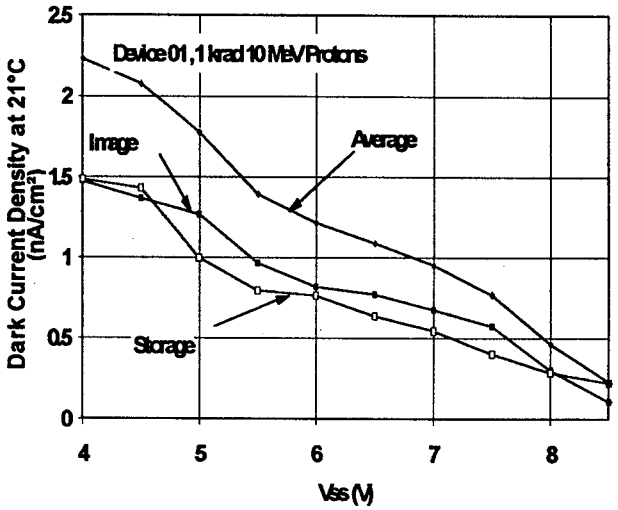


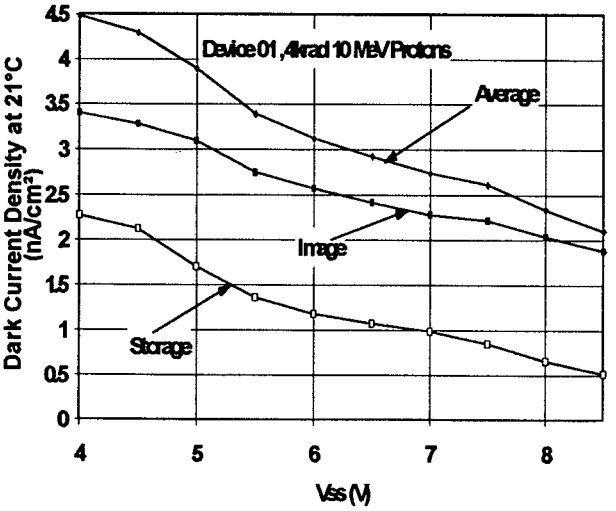


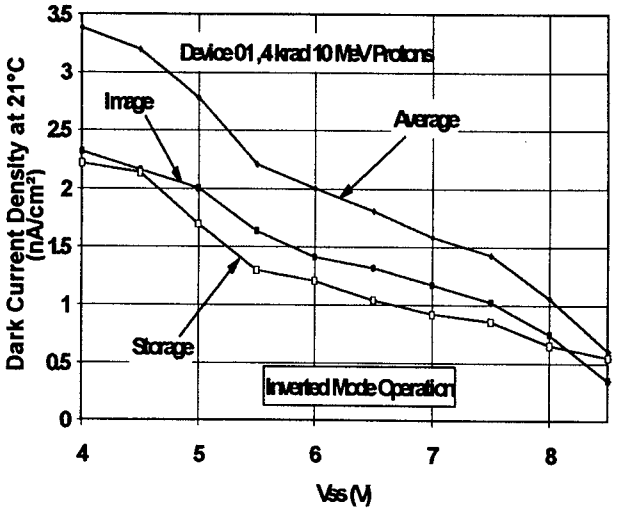


A/9119/00

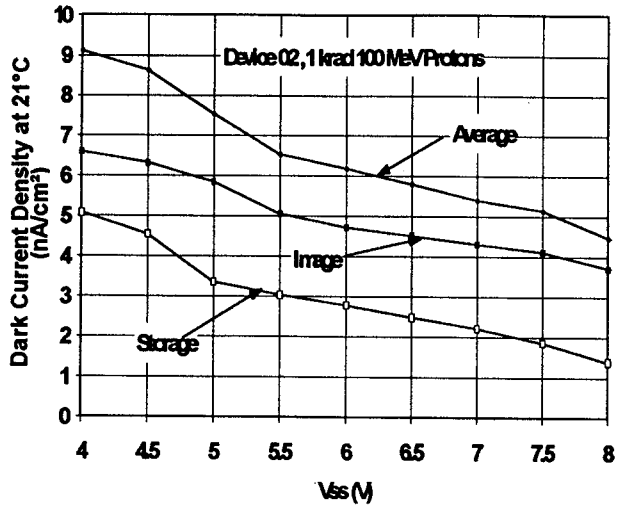


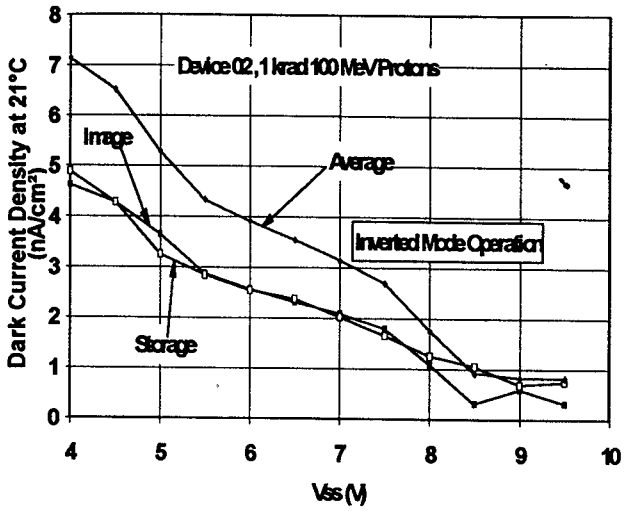


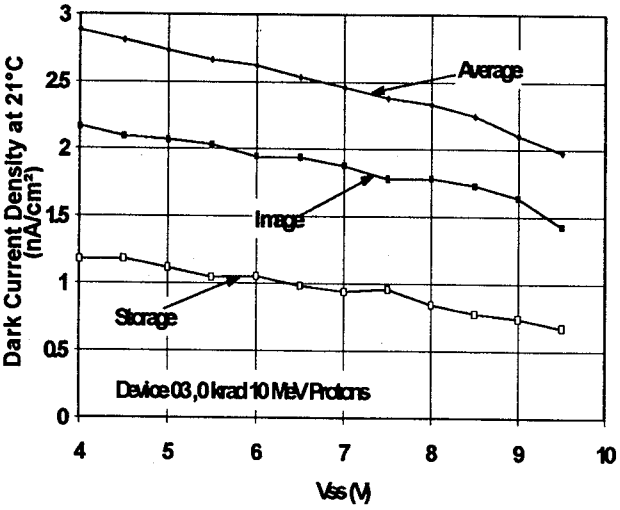


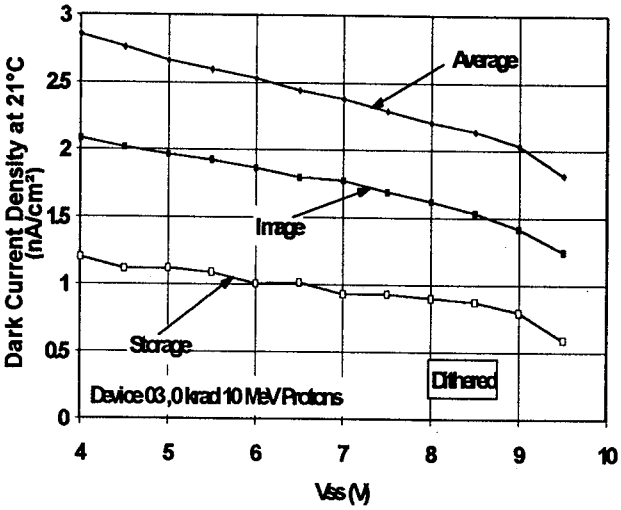


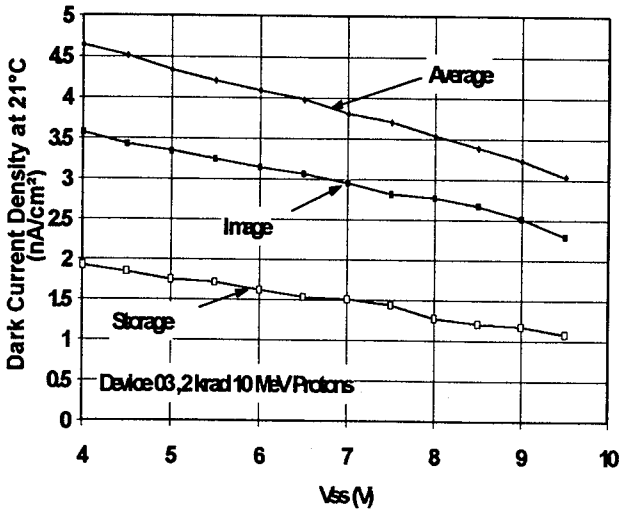


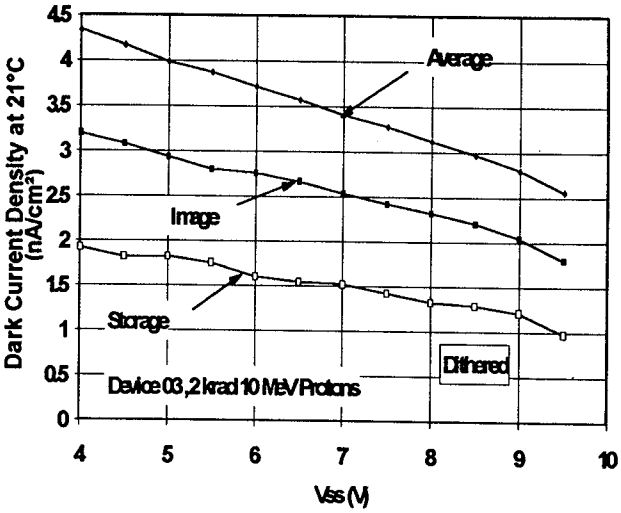


A/9119/00

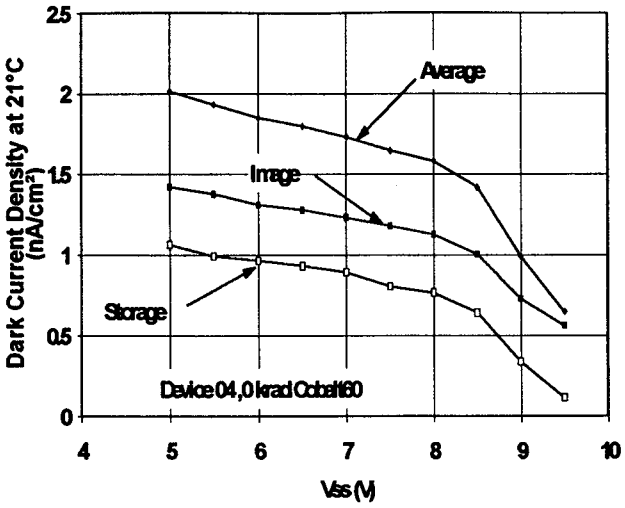


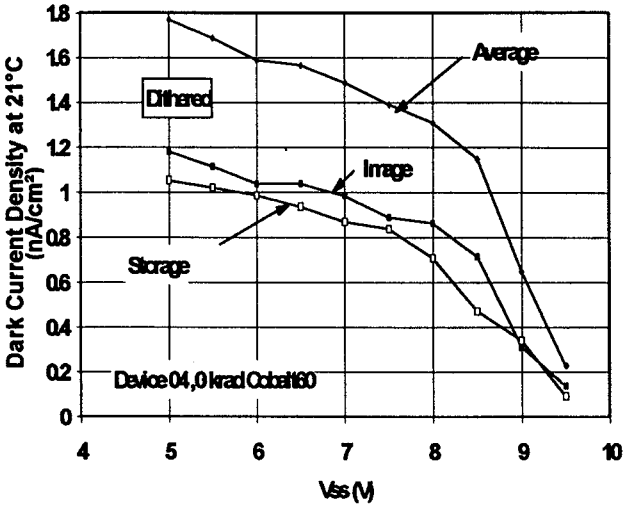


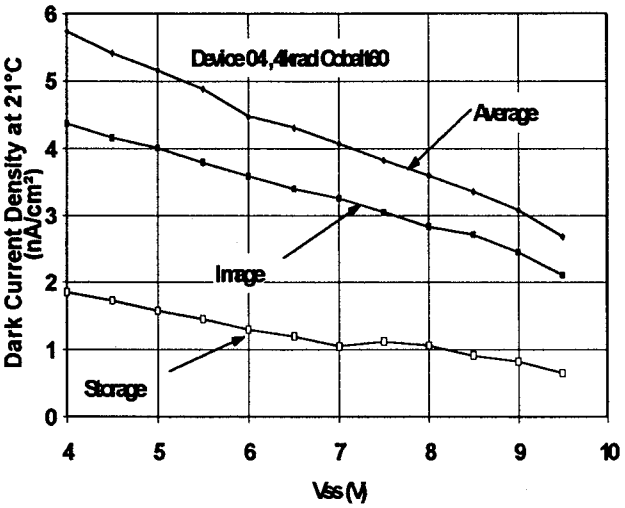


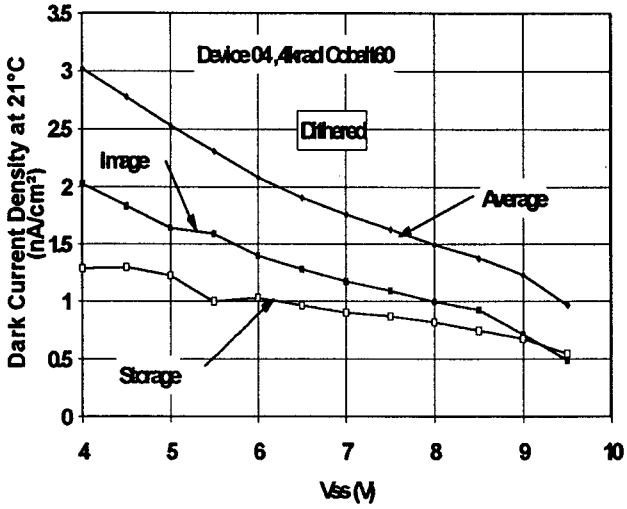


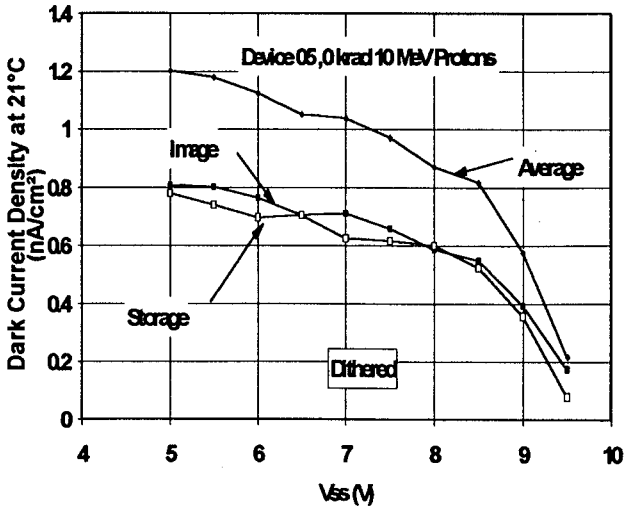


A/9119/00

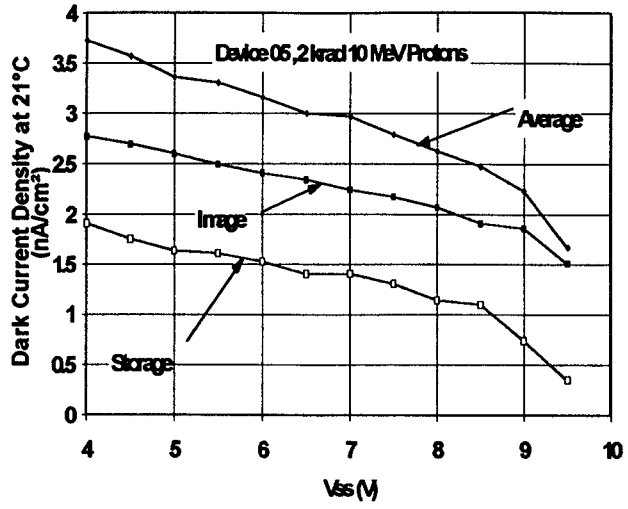


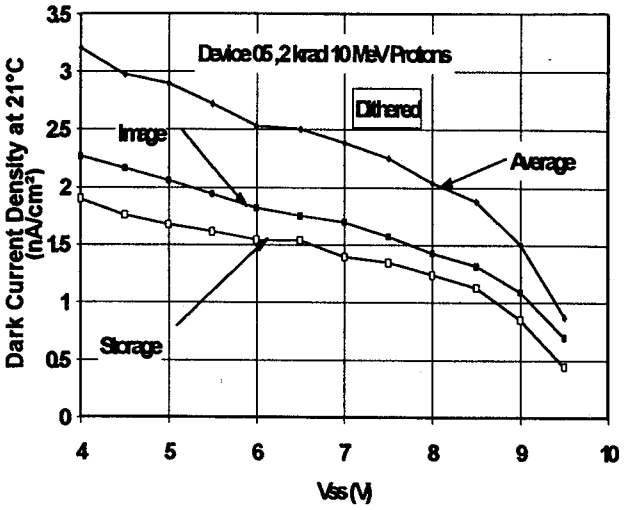


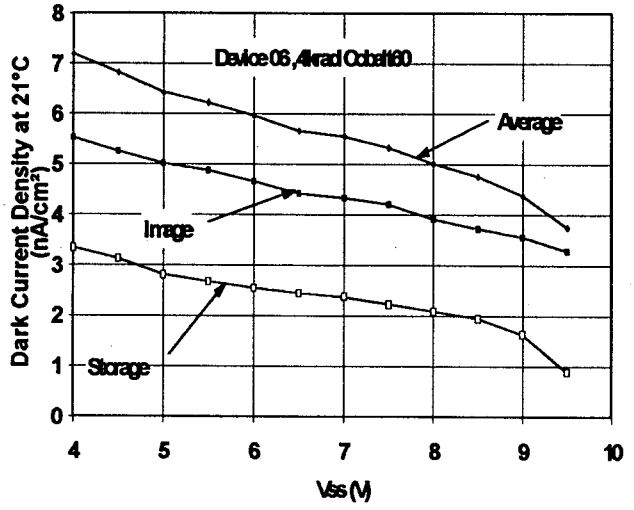


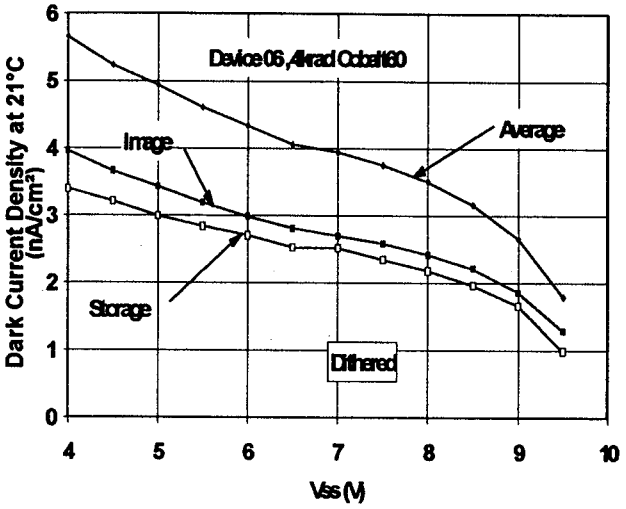


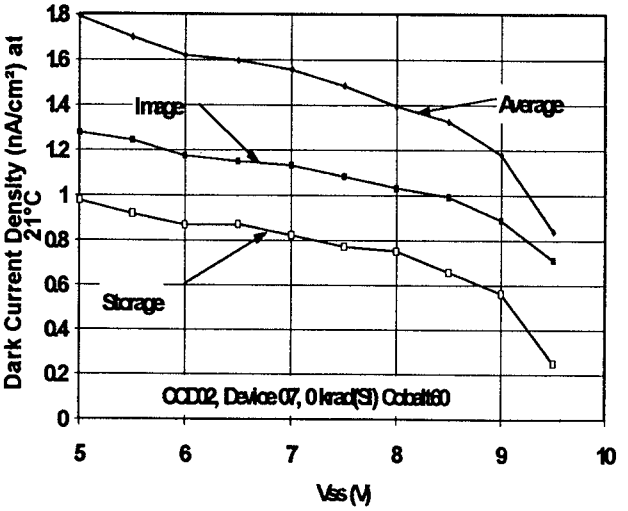


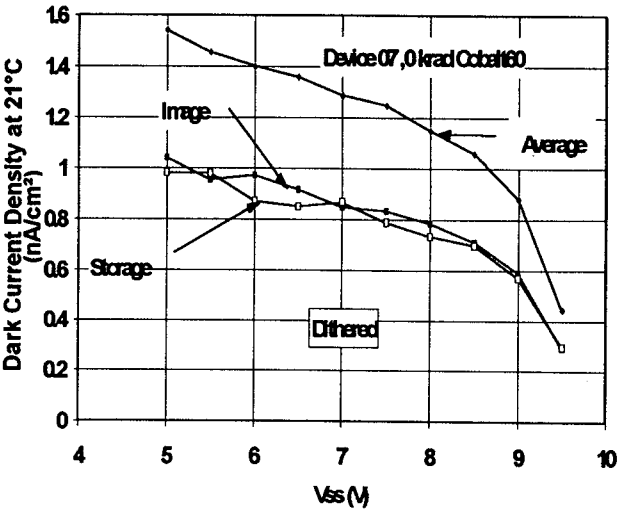


A/9119/00

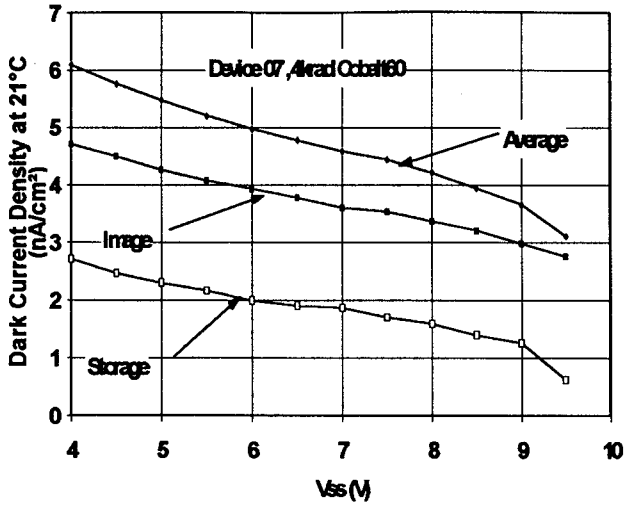


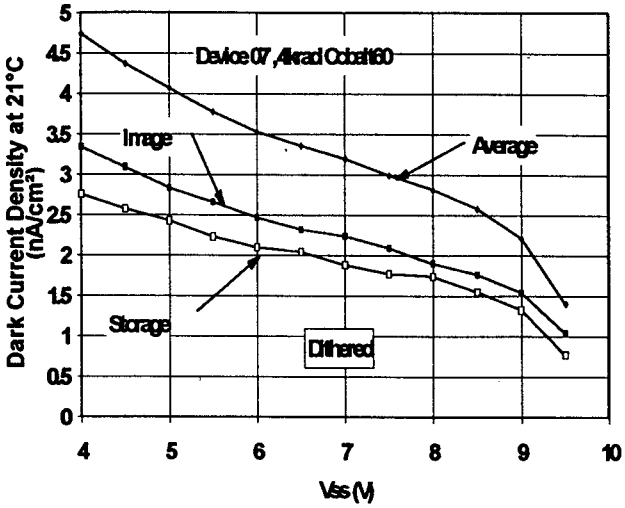


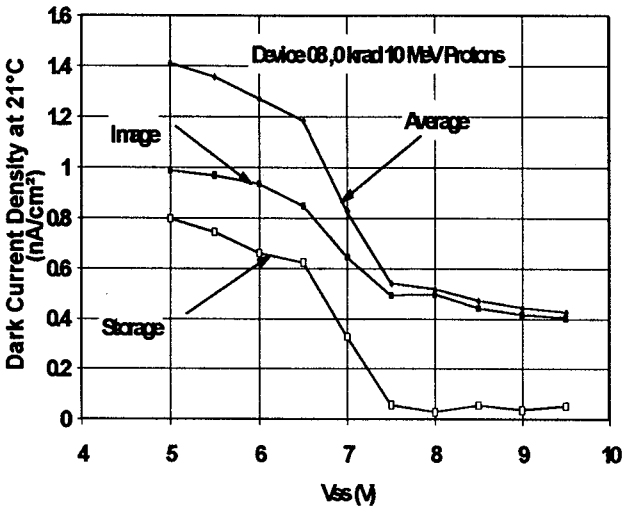


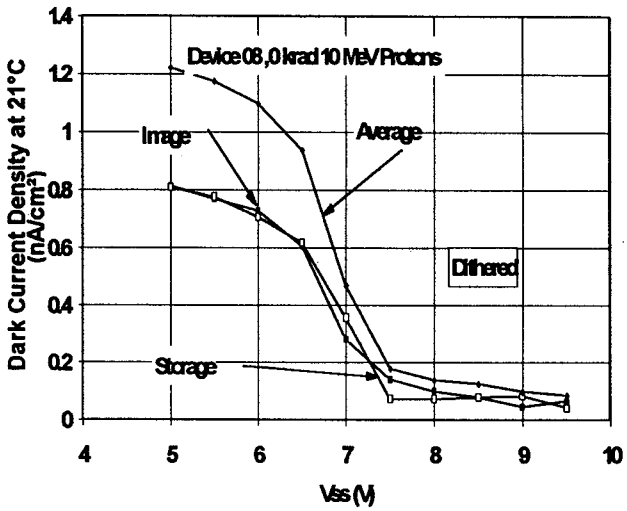


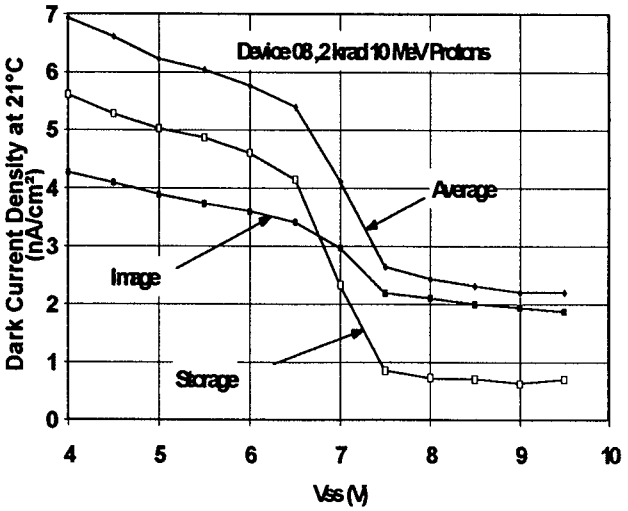


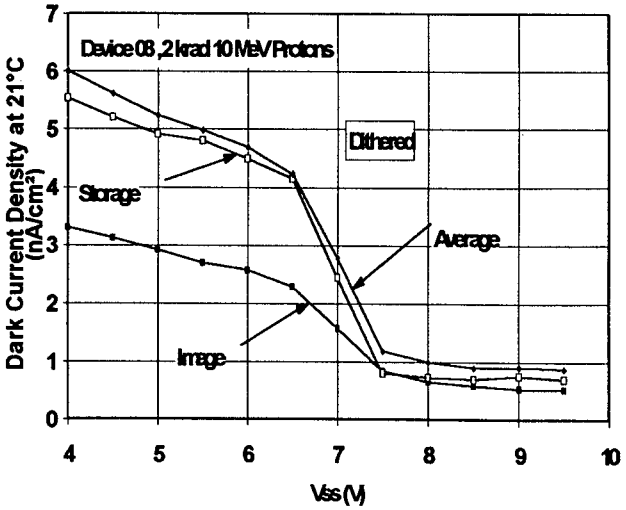


A/9119/00

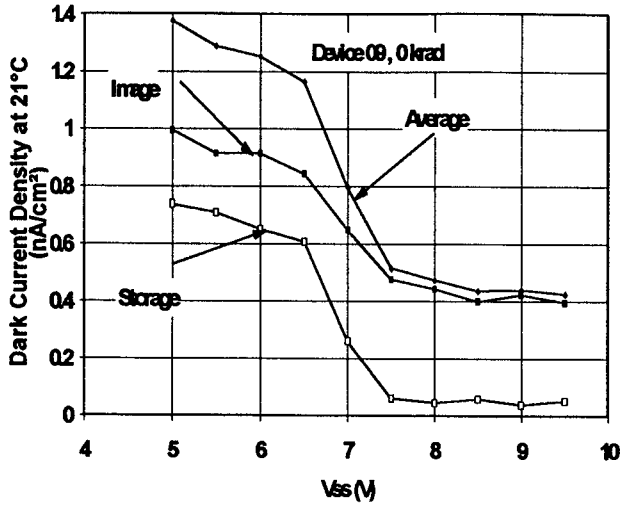


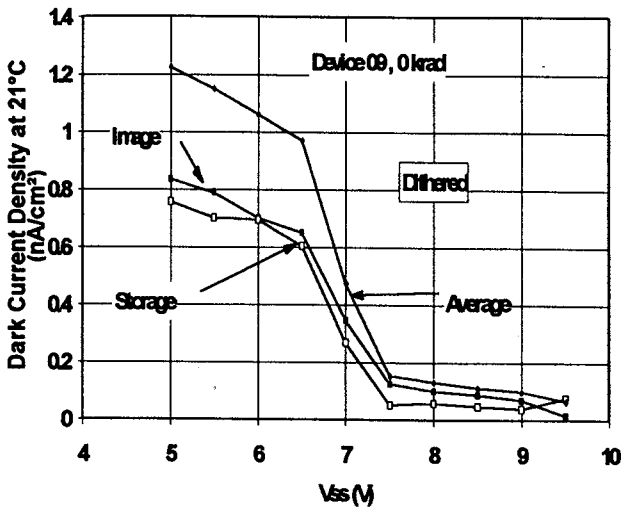


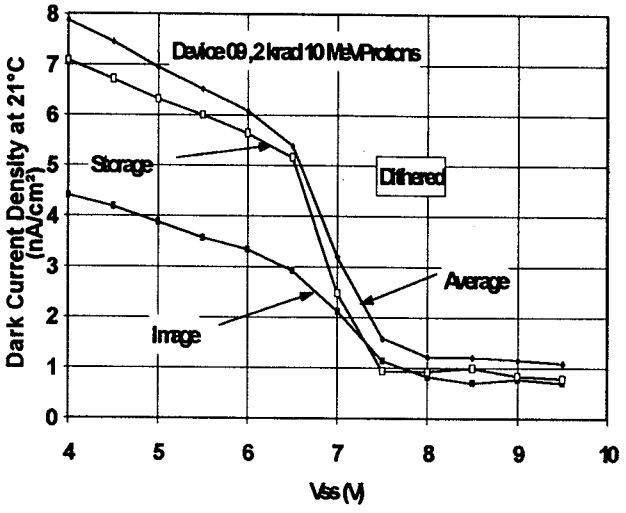


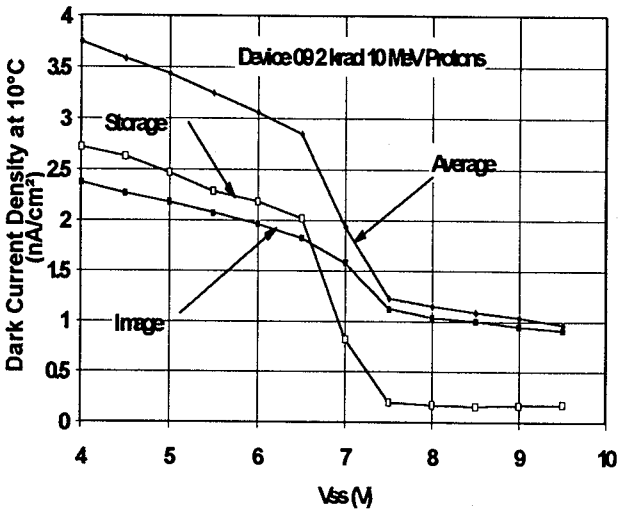


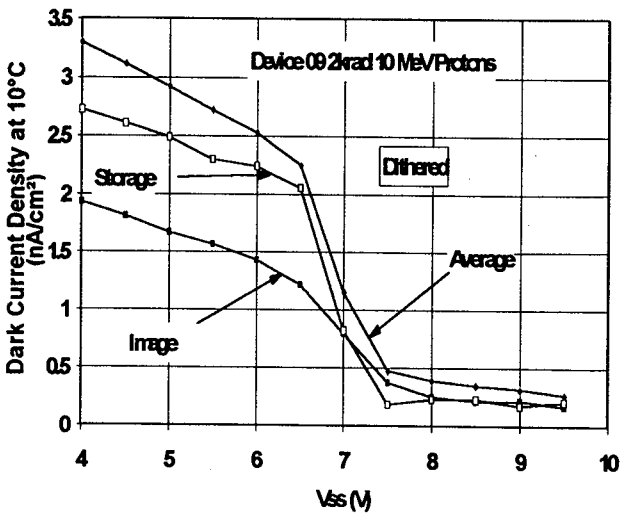


A/9119/00

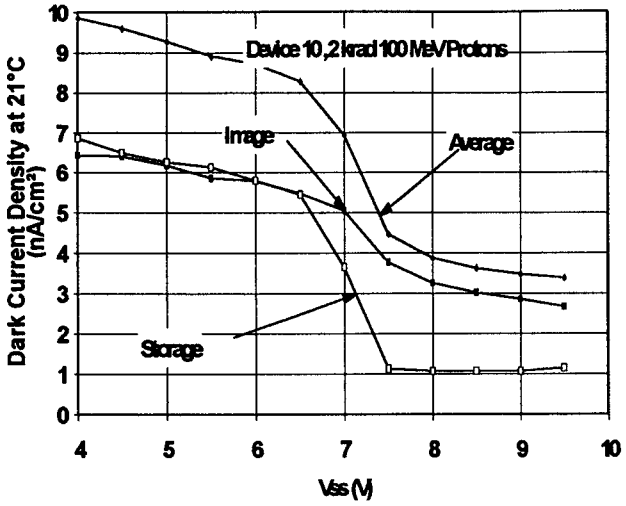


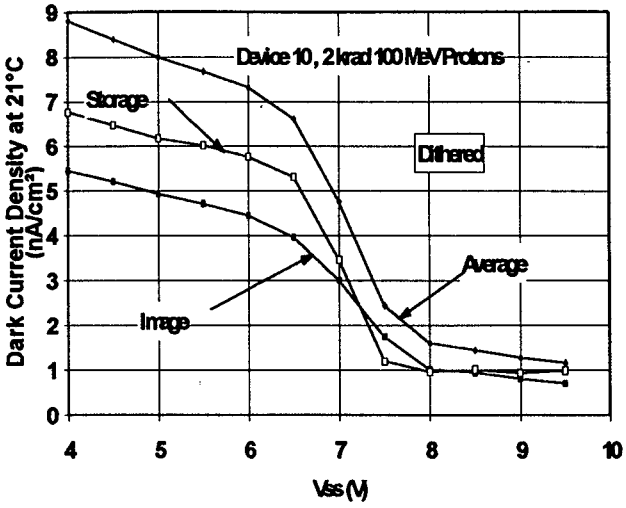


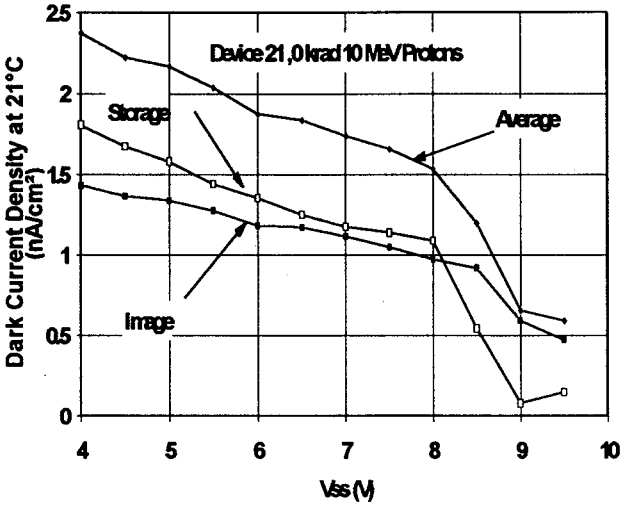


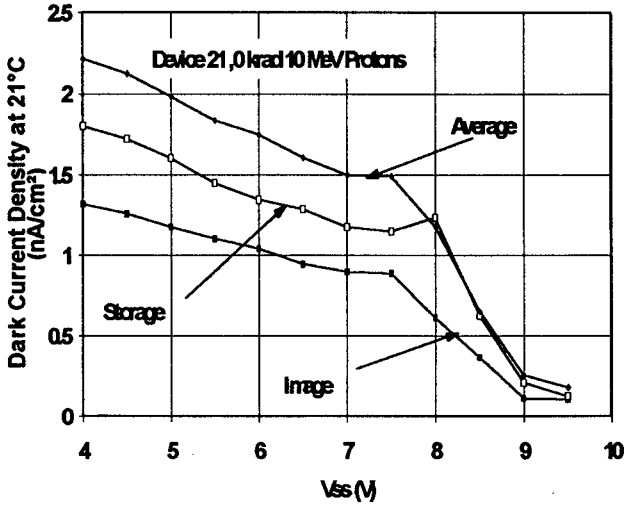


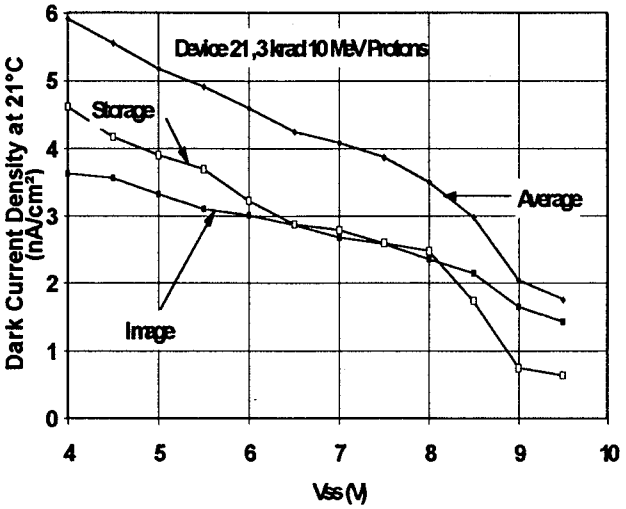


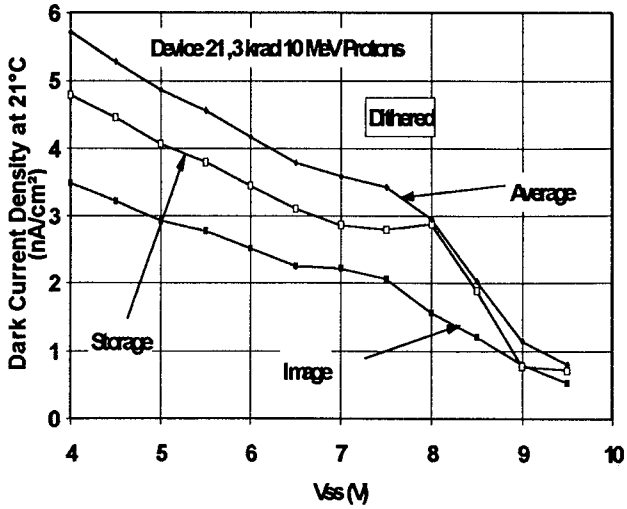


A/9119/00

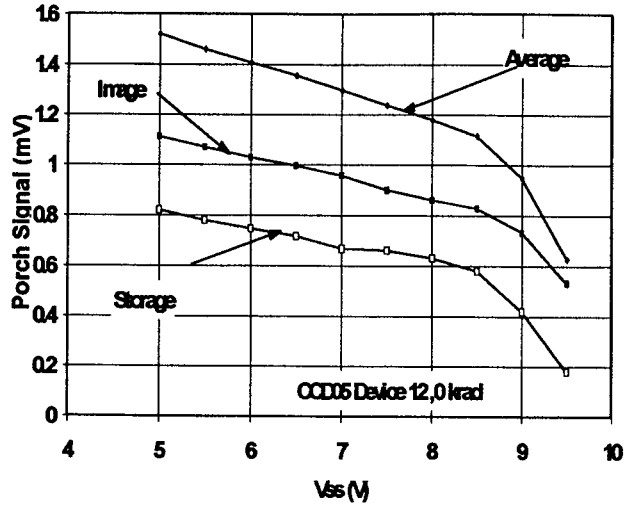


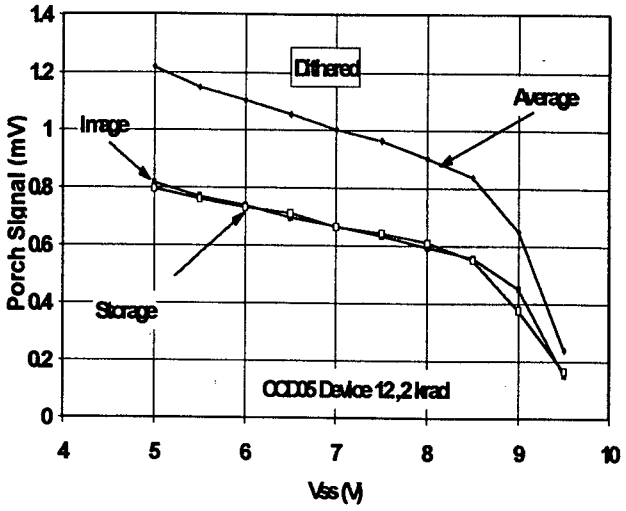


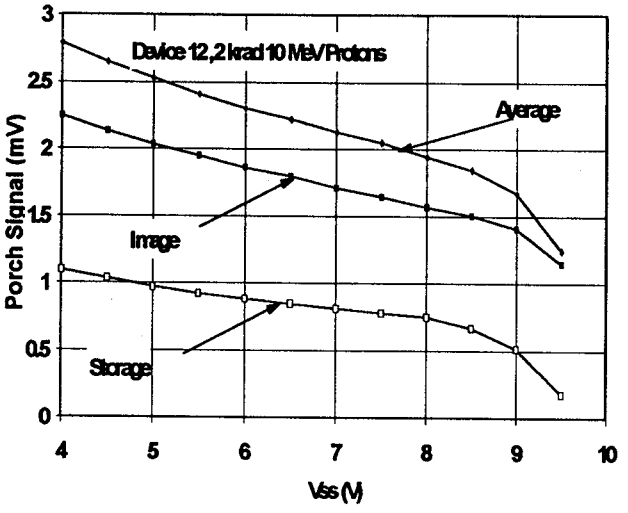


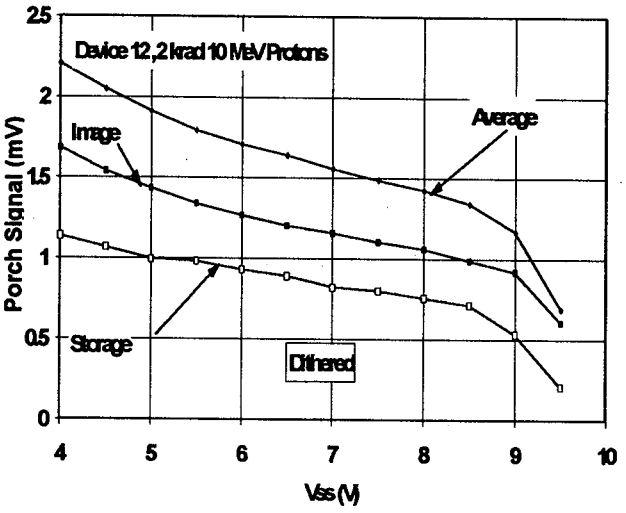


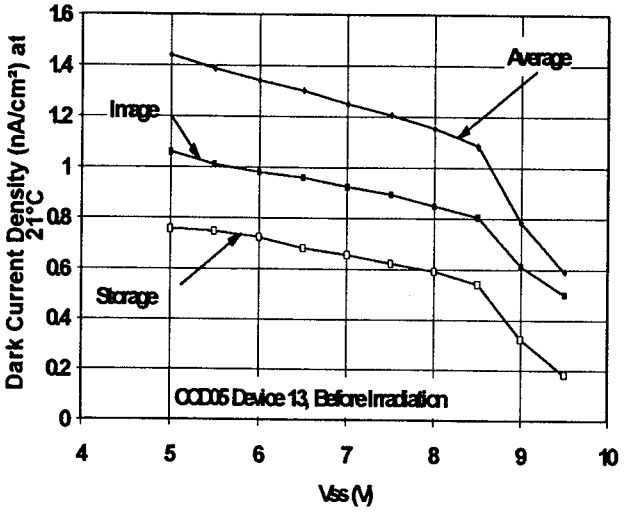


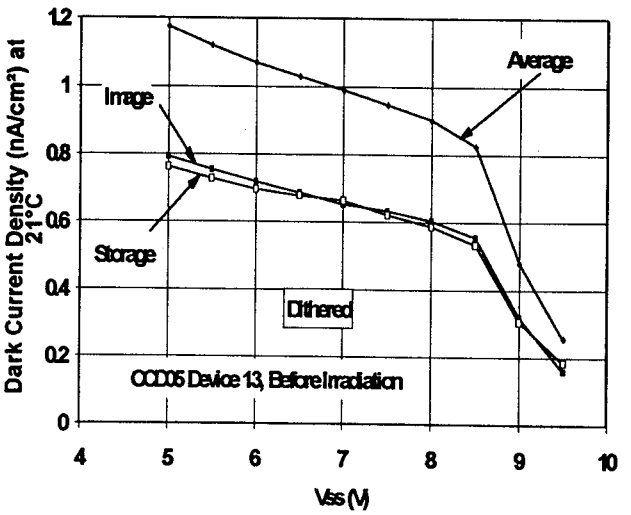


A/9119/00

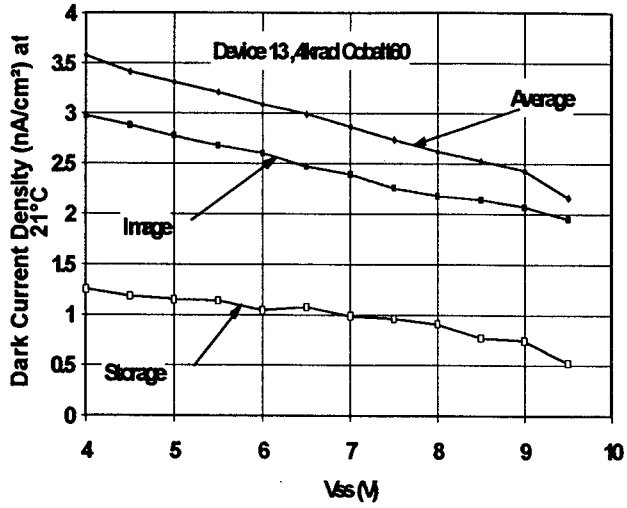


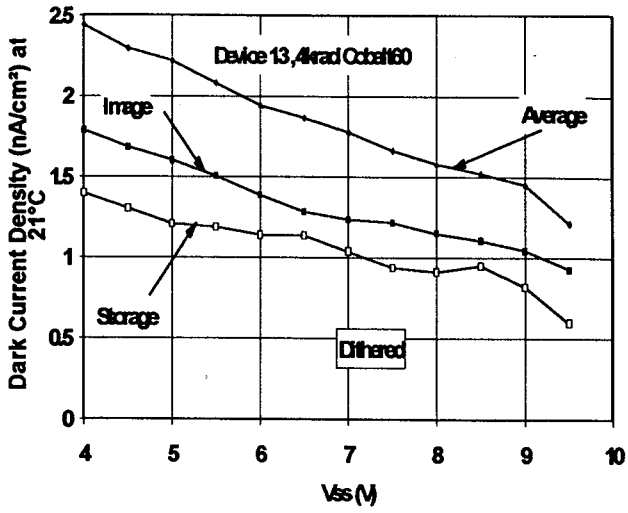


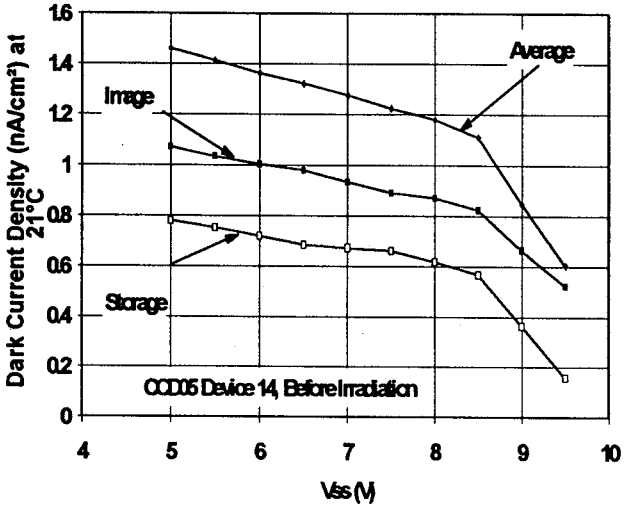


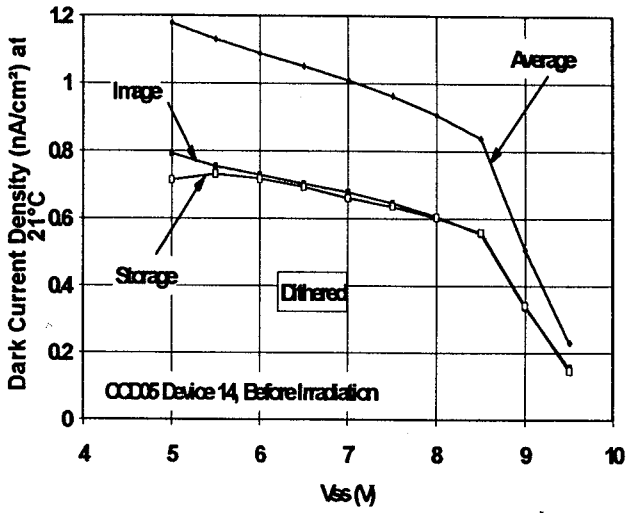


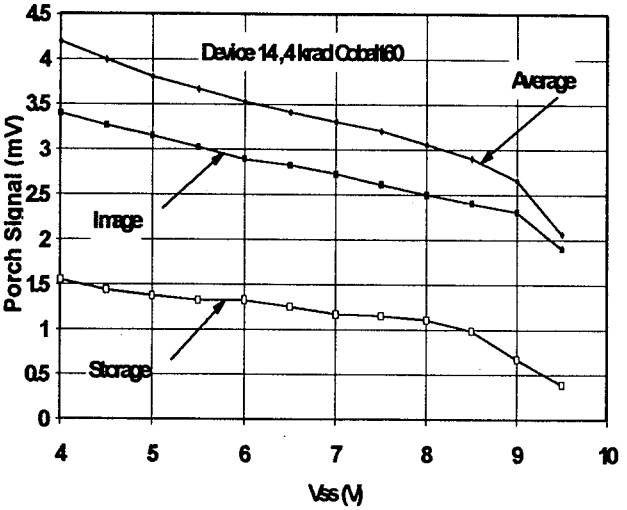


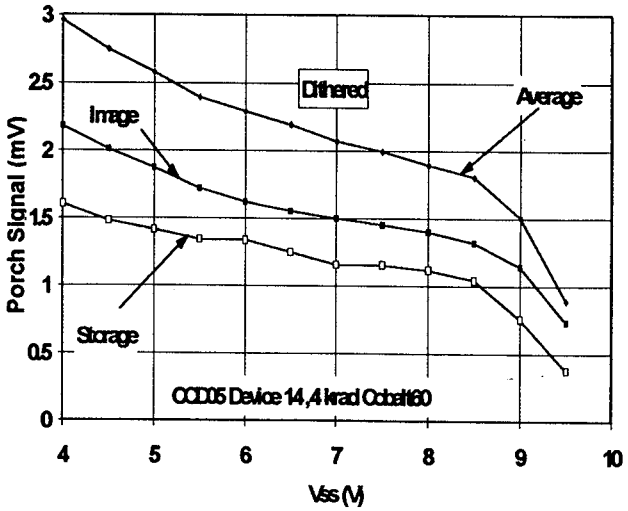


A/9119/00

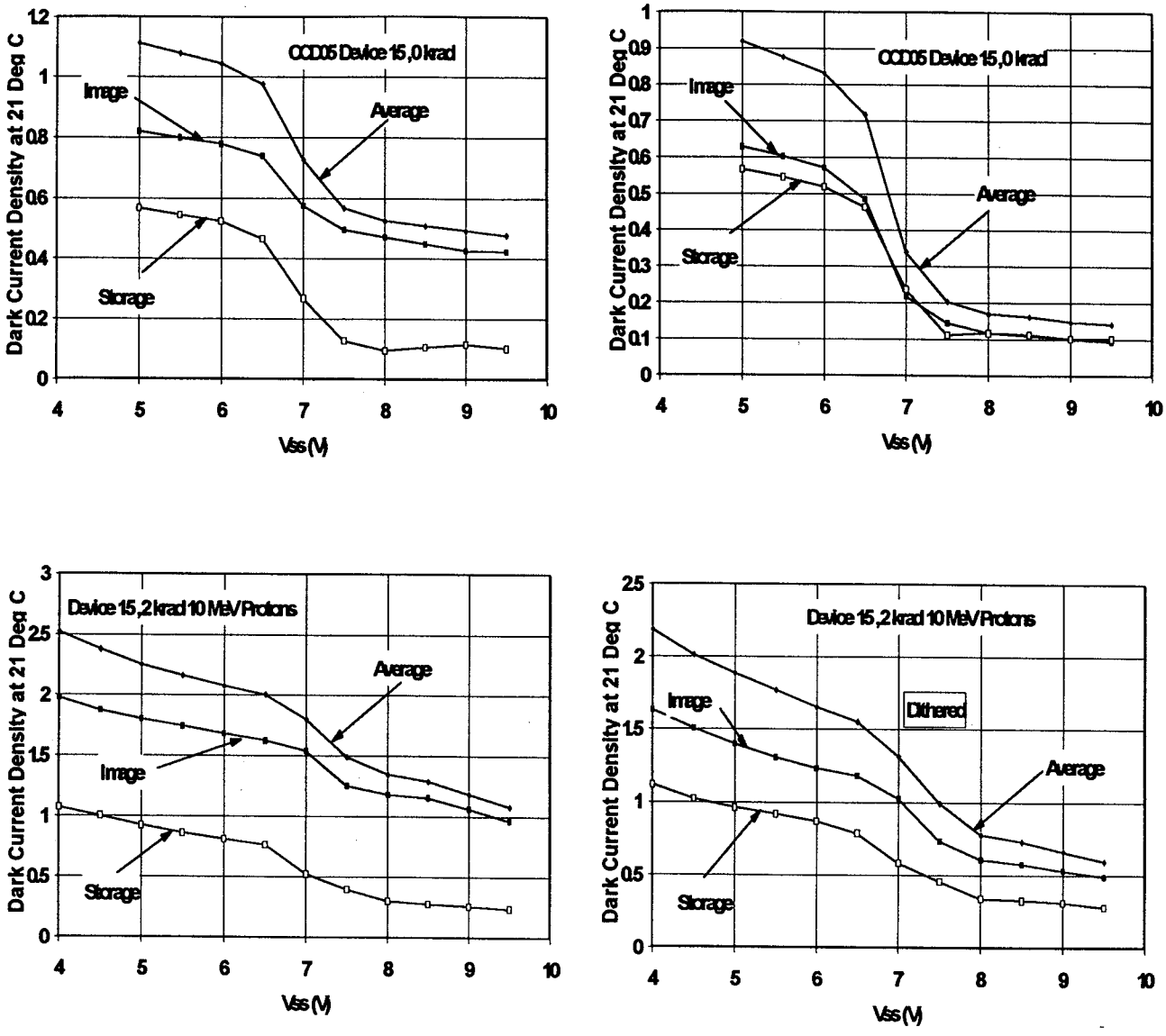


**Figure 3.2.1-6 Dark current versus $V_{SS}$ curves(not corrected for changes in amplifier gain with $V_{SS}$)**

i) The slowest rate of dither clocking (momentarily swapping phases I1 and I2) was for the CCD05 devices and normally occurred once per line readout (ie. once every 850μs). Doubling the rate (to twice per 850μs) made little difference to the dark charge suppression (figure 3.2.1-7), though there is a suggestion that the effect is greater after irradiation, ie. that the emission time from radiation-induced surface traps is less than for pre-existing ones.

ii) Reducing the time for which the clock phases were swapped (ie. the time available for surface trap filling) also had no effect - until times shorter than ~50ns were used (the normal time used was 330ns).

Hence there must be other reasons why the dark current suppression is not totally effective. At this point it maybe appropriate to take a diversion and consider the nature of the various dark current components [20]:

a) *Surface Component*

this is given by

$$J_s = q \int_0^{Eg} U(E_t)\, dE_t \qquad (1)$$

where the generation rate U is given by

$$U = \frac{\sigma_p \sigma_n V_{th} (pn - n_i^2) n_{ss}}{\sigma_n[n + n_i \exp\{(E_t - E_i)/kT\}] + \sigma_p [p + n_i \exp\{-(E_t - E_i)/kT\}]} \qquad (2)$$

where $\sigma_p$ and $\sigma_n$ are the capture cross sections for holes and electrons and n and p are the electron and hole concentrations. $V_{th}$ is the thermal velocity, $n_{ss}$ is the surface trap density and $E_t$ is the trap energy level. For a depleted surface not in inversion $n \gg n_i$ and $p \ll n_i$

$$\text{so} \quad U = \frac{\sigma_p \sigma_n V_{th} n_i n_{ss}}{\sigma_n \exp\{(E_t - E_i)/kT\} + \sigma_p \exp\{-(E_t - E_i)/kT\}} \qquad (3)$$

This function has a sharp maximum for mid-band states.

$$\text{and} \quad J_s = q \sqrt{(\sigma_p \sigma_n)}\, V_{th}\, D_{ss}\, \pi kT\, n_i / 2 \qquad (4)$$

Note that $V_{th}$ is proportional to $T^{1/2}$ and $n_i$ to $T^{3/2} \exp(-Eg/2kT)$. $D_{ss}$ is the trap concentration ($cm^{-2}\, eV^{-1}$) assumed to be uniform across the bandgap.

In inversion $p \gg n_i$ and n is still $\ll n_i$

$$U = \frac{\sigma_n V_{th} n_i^2 n_{ss}}{p} \quad \text{and} \quad J_{surface} = \frac{q \sigma_n V_{th} n_i^2 n_{ss}}{p} \qquad (5)$$

for mid-band states we have a surface dark current multiplied by a factor$(2n_i/p)$ which is normally $\ll 1$ since

$$n_i = 3.1 \times 10^{16}\, T^{3/2}\, e^{-0.603/kT}\ cm^{-3} \quad [20] \qquad (6)$$

$$= 1.4 \times 10^{10}\ cm^{-3} \text{ at } 300K$$

and p should be $\sim 10^{18}\ cm^{-3}$ when inverted. However if p is not so large - ie. we have weak inversion, then we are left with a component with an $n_i^2$ dependence that is defect related (proportional to $n_{ss}$).

b) *Bulk Generation*

$$J_{bulk} = \sqrt{(\sigma_p \sigma_n)}\, V_{th}\, q\, n_i\, W\, n_t \qquad (7)$$

where W is the depletion layer width and $n_t$ is the concentration of deep level traps. Again the dark current is proportional to $V_{th}\, n_i$, that is $T^2 \exp(-Eg/2kT)$.

c) *Diffusion Current*

This arises from random thermal generation of electron-hole pairs within a minority carrier diffusion length (L) of either side of the depletion layer.

$$J_{diffusion} = \frac{e\, D n_i^2}{N_A\, L} \qquad (8)$$

For a device thickness d<<L

$$J_{diffusion} = \frac{e\, D\, d\, n_i^2}{N_A\, L^2} \qquad (9)$$

Hence noninverted surface and bulk components vary as $T^3\, e^{-Eg/2kT}$ and $T^2\, e^{-Eg/2kT}$ respectively, and the inverted surface and diffusion components vary as $T^{7/2}\, e^{-Eg/kT}$.

For a deeply inverted surface we have only the bulk and diffusion dark currents. Dither clocking will be discussed further in the next section. To summarise we can give the following approximate parameters:

**Total dark current at 21°C (nA/cm$^2$) ( = surface + bulk components)**

| | **Pre-irradiation** | **increase/krad(Si)** |
|---|---|---|
| non inverted | 2 | 1.0 |
| inverted and dither clocking (worst case) | 0.5 | 0.5 |
| (typical) | 0.3 | 0.3 |

The value of 0.5 nA/cm$^2$ increase /krad when inverted is something of a worst case - the increase is less for some devices (particularly for the storage region). A value of 0.3 nA/cm$^2$ (21°C) per krad is more typical. Note that it will be seen in section 4.2 that 10 MeV protons induce an increase of 0.1 nA/cm$^2$ per krad so this accounts for some but not all of the effects. From the data in table 3.2-1 there is indeed some indication that the inverted dark charge is slightly higher for proton-irradiation devices. We return to the subject of dark current mechanisms in section 3.2.5 where it will be seen that the temperature dependence gives some clues as to the origin of the ionization-induced dark charge.

Finally we note that mechanisms for dark current damage seem to be the same for both front and back illuminated devices ie. there are no new effects for the back illuminated CCDs.

### 3.2.2 Dither Clocking

Here we look ahead to the results of later sections and note that:

i) from a preliminary examination of linearity for proton damaged CCD05 devices, the full well capacity does not seem to be significantly affected by the increase in $V_{SS}$ (which must necessarily decrease the depth of the depletion region). However this finding will need confirmation by a more comprehensive testing of flight representative devices.

ii) The action of dither clocking moves charge backwards and forwards within a pixel. If trapping states are present in the buried channel (eg. caused by proton displacement damage) then these can give rise to black/white pixel defects as described in section 4.3. It was however found that the number of pixels affected was small (a few tens) and the resulting dark signal non-uniformity was less than that due to displacement damage. If necessary the number of black/white pairs can be greatly reduced by reducing the potential of the barrier phase which is not dithered (in this case I3) - so that charge cannot come into contact with traps at the pixel boundary [21]. This technique was tried with some success.

### 3.2.3 Dependence on angle of incidence

Device 09 was irradiated with 10 MeV protons at 0°, 22.5°, 45° and 67.5° (separate regions of the chip for each angle). The flux was varied so that the number of protons received per $cm^2$ (ie. the fluence) was always $3.58 \times 10^9$ p/$cm^2$ (corresponding to 2 krad(Si) ionizing dose at 0°).

The dependence on angle is shown in figure 3.2.3-1. As might be expected, the dark current increases with secθ (since the dose, in krad, increases as secθ).

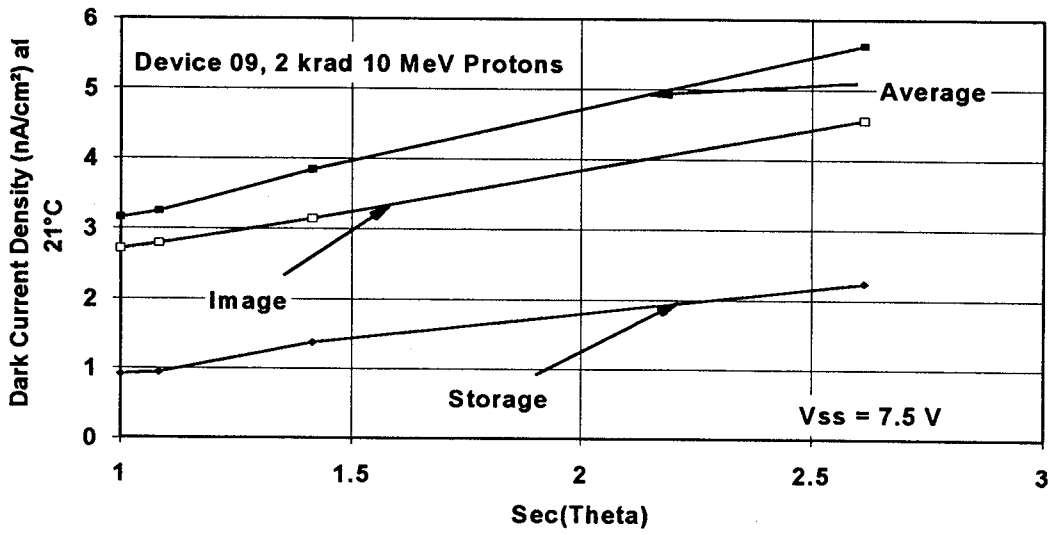


**Figure 3.2.3-1 Dark current versus secθ for device 09**

### 3.2.4 Annealing Behaviour

So far we have discussed measurements made 3 months after irradiation when annealing effects are assumed to have, by and large, taken place. Measurements of dark current, made immediately after irradiation in fact showed lower levels of initial damage, as shown in figure 3.2.4-1. Thus we see a reverse annealing effect, presumably similar to that occurring with Thomson-CSF devices ([9], [10], [18]) and due to the slow build-up of interface states. One device (06) was given a 24 hr 100°C bake 2 weeks after irradiation and, as with Thomson-CSF CCDs, this was found to accelerate the reverse annealing process (though in this case there was a small 'overshoot' and subsequent reduction in dark current).

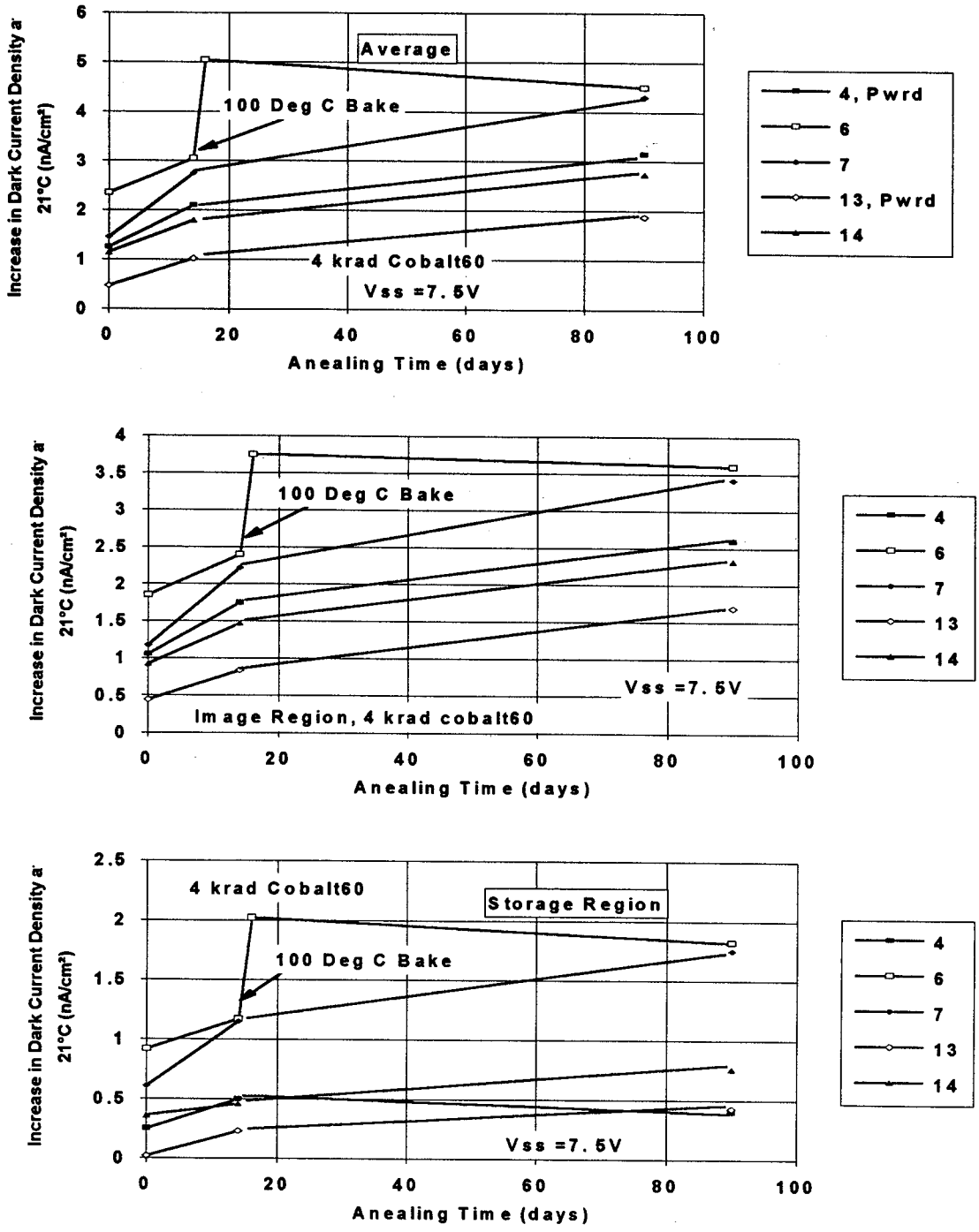


**Figure 3.2.4-1 Reverse annealing behaviour**

### 3.2.5 Temperature Behaviour

Measurements of dark current were made at several temperatures for the two CCD05 devices (12 and 15) that were given proton irradiation. Figure 3.2.5-1 shows plots illustrating the linear behaviour of ln(dark current) with 1/kT. Figures 3.2.5-2 and 3.2.5-3 show the effective activation energy derived from the slope of these plots for various values of $V_{SS}$. It is seen that for the image region of a standard resistivity device (number 12, 20Ωcm) when not inverted or dithered - ie. for surface dark charge, the behaviour is

$$I_{dark} = \text{const. exp } (-E/kT), \text{ where } E = 0.63 \text{ eV}$$

but for the storage region and the image region when using dither clocking the activation energy is roughly 0.7eV at low VSS, jumping to around 0.85 on inversion (at VSS = 9V).

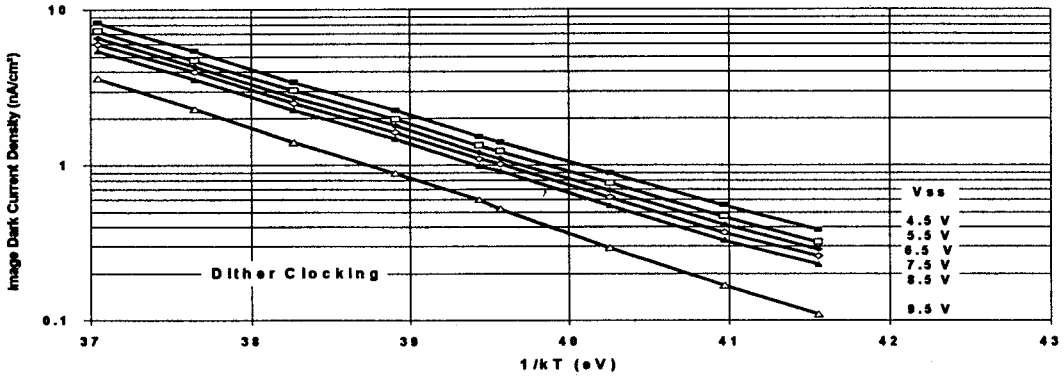


**Figure 3.2.5-1 ln(dark charge) versus 1/kT**

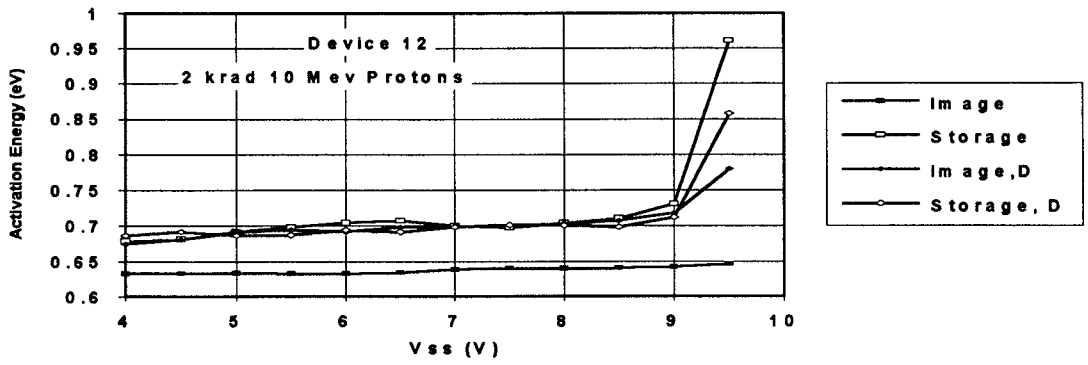


**Figure 3.2.5-2 Effective activation energy versus $V_{SS}$**

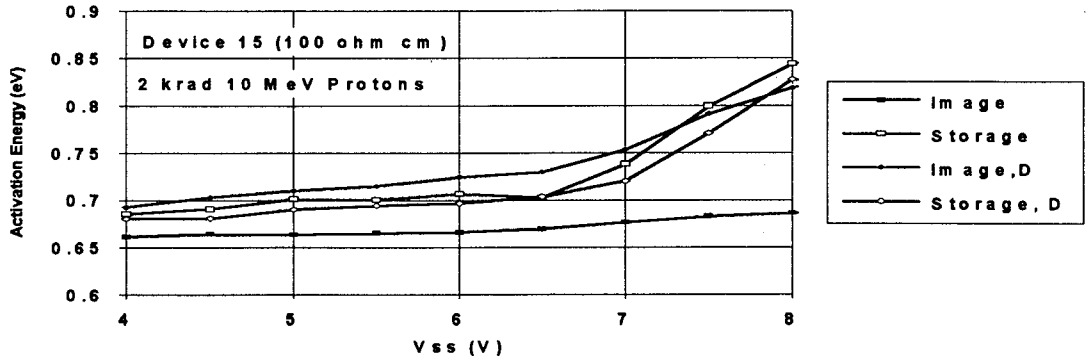


**Figure 3.2.5-3 Effective activation energy versus $V_{SS}$**

For a 100μm epi, 100Ωcm device (number 15) the activation energy for the surface image area component is slightly higher (~0.66eV) but again is higher still for the storage region at low $V_{SS}$ (~0.7 eV) and again jumps to ~0.85eV on inversion (this time occuring at $V_{SS}$ = 0.7V).

The thicker, higher resistivity, device 15 will show an increased diffusion component (equation 9) which will then give a higher activation energy (because of the exp Eg/kT behaviour) and it is possible that the increases in activation energy, in both devices, is due to the diffusion component. This will, however, not be altered by radiation (it is an intrinsic, rather than defect related property). The nature of the radiation-induced increases in dark current, when inverted, could still be due to surface damage if the surface is only weakly inverted. This seems the most plausible explanation at present since it would explain the temperature dependence. The effect of having both a $n_i$ and $n_i^2$ dependence was simulated by plotting the temperature behaviour of the function

$$\text{dark current} = \text{const. } T^2 \quad ( e^{-Eg/2kT} + \beta e^{-Eg/kT} )$$

where β is a constant (termed the dark current ratio). This function is plotted in figure 3.2-4. It is seen that the plots are almost linear (not quite as linear as the experimental data of figures 3.2.5-2 and 3.2.5-3). The effective activation energy is shown in figure 3.2.5-5. To change the effective activation energy from 0.6 eV to 0.8 eV requires a large change in β, ie. a large suppression factor for the $n_i$ component. At 0.6 eV the are roughly comparable in size.

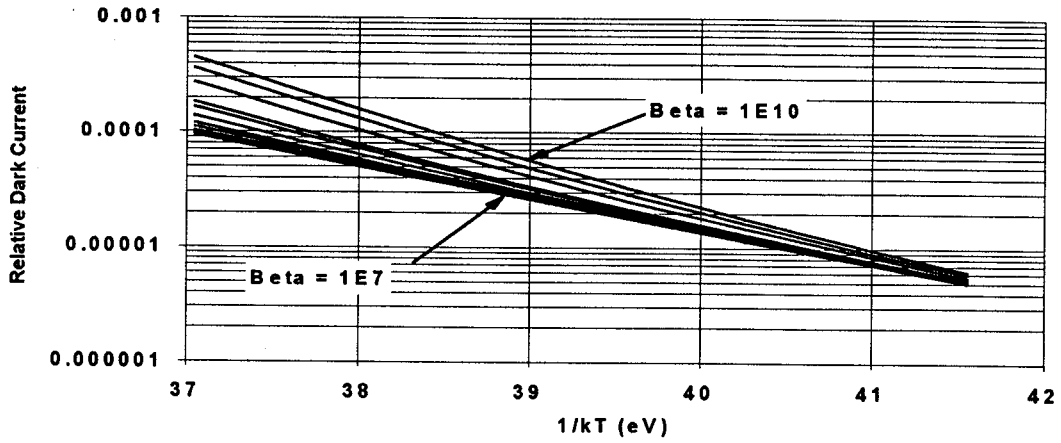


**Figure 3.2.5-4 1n(dark charge) versus 1/kT - simulation**

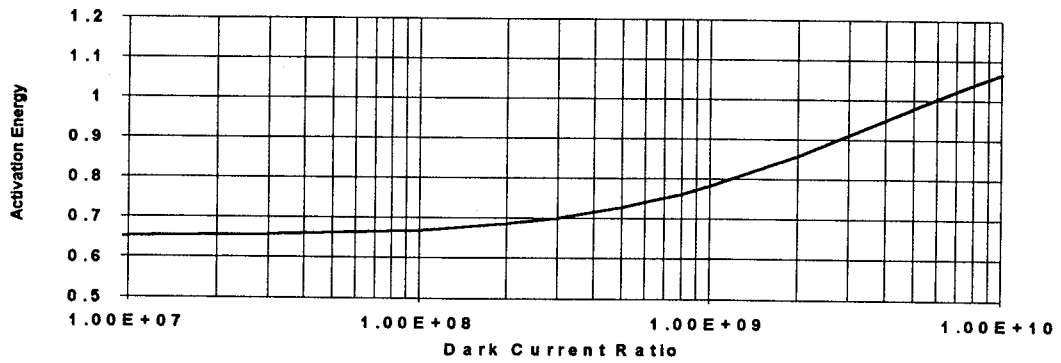


**Figure 3.2.5-5 Effective activation energy versus the ratio betweenexp(-Eg/kT) and exp(-Eg/2kT) dark current components - simulation**

Note that since the dark current under inversion has a high effective activation energy, cooling the CCD is very effective in reducing the CCD dark current. As an illustration we show relative dark charge values (compared with 20°C) at 5°, 10° and 15°C for activation energies of 0.63, 0.7, 0.8, 0.9 and 1.0 eV:

**Relative dark currents (compared with value at 20°C)**

| activation energy (ev) | 5° | 10° | 15° | 20° |
|---|---|---|---|---|
| 0.633 | 0.26 | 0.41 | 0.65 | 1 |
| 0.7 | 0.22 | 0.38 | 0.62 | 1 |
| 0.8 | 0.18 | 0.33 | 0.58 | 1 |
| 0.9 | 0.15 | 0.28 | 0.54 | 1 |
| 1.0 | 0.12 | 0.25 | 0.50 | 1 |

Differences in the temperature behaviour pre- and post-irradiation and inverted compared with non-inverted operation have also been found with Tektronix devices [21a].

### 3.3 Linearity and Full Well Capacity

These are parameters that could conceivably be affected by ionizing radiation and it is especially important to know if increasing the substrate voltage causes any decrease in full well capacity. Measurements were made for CCD05 devices only. Figure 3.3-1 shows a typical linearity plot for a CCD05 device obtained by illuminating the CCD with a slit (image width ~1.5 pixels). The irradiance was kept constant and the plot obtained by varying the integration time. The figure indicates the sharp onset of saturation characteristic of EEV devices (both for uniform and spot illumination).

Late in the project it was found that the clock drivers used in the CCD camera (type TSC430) did not have sufficient drive capability to give the highest full well capacity for the centre of CCD05 images. At the edges (where the clock waveforms are not degraded by the distributed electrode capacitance) there is some confidence that the performance is satisfactory (particularly if clock high voltages of 12V are used), however for the centre (1 krad and 0 krad regions of proton irradiated devices) the full well capacity is reduced by ~10% (even for 12V clock high voltages). For device 12 we have the following full well capacities:

| | | 2 krad | 4 krad |
|---|---|---|---|
| $V_{SS}$ = | 7.5V | $4.1 \times 10^5$ e | $4.4 \times 10^5$ e |
| | 8.5V | $3.9 \times 10^5$ e | $4.4 \times 10^5$ e |
| | 9.5V | $3.7 \times 10^5$ e | $4.0 \times 10^5$ e |

and for device 13 (4 krad cobalt 60)

| | | |
|---|---|---|
| $V_{SS}$ = | 7.5V | $4.0 \times 10^5$ e |
| | 8.5V | $3.9 \times 10^5$ e |
| | 9.5V | $3.5 \times 10^5$ e |

There is a suggestion that increasing Vss to 9.5 (from 7.5V) decreases the full well capacity by about 10%.

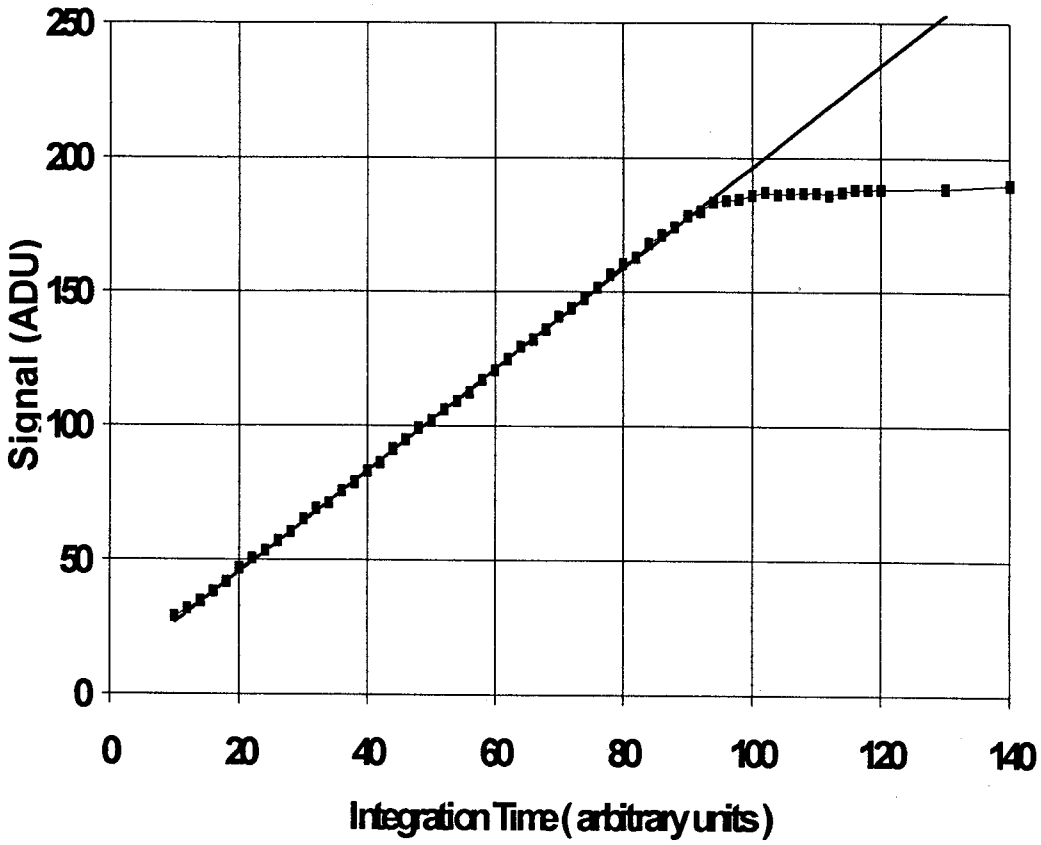


**Figure 3.3-1 Linearity plot for CCD05 device**

# 4. BULK DISPLACEMENT DAMAGE

## 4.1 Effect on Charge Transfer Efficiency (CTE)

In readout, charge is transferred from pixel to pixel and during this process defects within the buried channel can trap charge and release it some time later into a following charge packet - thus giving a loss in CTE. It is also possible that bulk traps can cause a loss in signal due to recombination (especially at room temperature), however no evidence has been found for this ( at the relatively low fluences used) and it will not be discussed further.

The CTE was measured for two proton-irradiated CCD05 devices. Devices 12 and 15 were studied using optical illumination and in addition number 15 was studied using 22 keV x-rays from a $Cd^{109}$ source. The present CCDs do not have an input gate structure and so methods such as the periodic pulse technique ([12], [22]) are not easily applicable.

### 4.1.1 Theory

For simplification, we take a situation where isolated signal packets are being transferred through the CCD and that the time between passages of successive charge packets through a given pixel is longer than the time for a trap to emit. This would be the case for spot (or horizontal line) illumination or illumination by x-rays (with a suitably low event rate).

If there is a background charge in each pixel, due to dark current, or a uniform (or slowly varying) background illumination from the scene this will tend to act as a 'fat zero' and keep a proportion of the traps permanently filled. It is only the isolated peak signals which occupy a larger volume in the buried channel, and hence which are exposed to unfilled traps, which concerns us here. For deep level traps in the n-buried channel, capture and emission are governed by the time constants:

$$\text{capture time} = \tau_c = \frac{1}{\sigma_n \, v_{th} \, n_s} \qquad (1)$$

$$\text{emission time} = \tau_e = \frac{\exp(E/kT)}{\sigma_n \, X_n \, v_{th} \, N_c} \qquad (2)$$

where
- $\sigma_n$ = capture cross section for electrons
- $v_{th}$ = average thermal velocity for mobile electrons
- $n_s$ = signal density (ie. density of electrons in the buried channel)
- $N_c$ = effective density of states in the conduction band
- $T$ = absolute temperature
- $k$ = Boltzmann's constant
- $X_n$ = the 'entropy factor' accounting for the entropy change accompanying electron emission from the trap
- $E$ = energy level of the trap below the conduction band.

The nature of radiation-induced deep level traps was discussed in [10]. The defect likely to be most important for n-buried channel CCDs is the phosphorus-vacancy complex or P-V centre. For this defect we follow Robbins et al [12] and use the data of Brotherton and Bradley [23]:

P-V centre : $X_n = 1.7$; $E = 0.456$ eV; $\sigma_n = 3.7 \pm 0.2 \times 10^{-15}$ cm$^2$

$N_c$ is given by

$$N_c = 2 \left[ \frac{2\pi M_{de}^* kT}{h^2} \right]^{3/2} \quad (3)$$

where h is Planck's constant and $M_{de}^*$ is the density of states effective mass for electrons

and $v_{th} = \sqrt{(3KT/m^*)}$ ,where m* is the effective mass.

Based on data given by Sze [20] to calculate the effective mass, Banghart et al [24] give the relation

$$V_{th}\ N_c = 4.11 \times 10^{25} (T/77)^2 \text{ cm}^{-2}\text{ s}^{-1} \quad (4)$$

with these values we have $\tau_e$ (in μs) as follows:

| E (eV) | 5°C | 10°C | 15°C | 20°C | 25°C |
|---|---|---|---|---|---|
| 0.456 | 53.9 | 37.2 | 26.0 | 18.3 | 13.1 |
| 0.45 | 42.0 | 29.1 | 20.4 | 14.5 | 10.4 |
| 0.44 | 27.7 | 19.3 | 13.6 | 9.7 | 7.0 |

Here we take a range of values for the energy level since the exponential term gives a strong dependence. At 15°C we see that $\tau_e$ ~20μs.

The capture time constant, $\tau_c$, depends on the density of signal electrons in the buried channel. Robbins et al [12] have shown that times of the order of a few hundred nanoseconds are typical. This is much less than the emission time and we can assume that when a packet is transferred into a pixel, charge is quickly trapped and slowly released over periods ~$\tau_e$. Clearly when a trap is full it is not available for further trapping until the electron is released. At any time, $t_o$, measured relative to the last passage of a signal packet, the density of traps available to capture signal is

$$N_a = \text{constant} . (1-\exp(t_o/\tau_e)) \quad (5)$$

In our case of isolated charge packets we have $t_o >> \tau_e$ and $N_a$ is maximised.

If the time spent under a gate electrode, $t_g$, is comparable with or shorter than $\tau_c$ then we have the situation that not all the available traps are filled and the charge lost from the signal packet is given by

$$q_{lost} = \text{constant}\,(1-\exp(-t_g/\tau_e)) \qquad (6)$$

It should be noted that there is an extra complication when the electric fields present are greater then ~$10^4$ V/cm in that Poole-Frenkel emission results in a reduction in $\sigma_e$ (cf. Banghart et al [24]). Robbins et al found good agreement between the basic theory and their measurements on EEV CCDs using the periodic pulse technique. This suggests that the field-enhanced emission is not significant for most of the traps in their devices but the possibility of reduced $\tau_e$ cannot, in general, be ignored.

4.1.2 X-ray Results

4.1.2.1 Parallel CTE

X-ray events from a $Cd^{109}$ source produce signals ~6,000 electrons (one electron for every 3.65 eV of photon energy). Absorbtion events within the depletion layer are confined within one pixel (or split between two adjacent pixels if the event occurs at a boundary). Events within the field-free region below the depletion layer will spread by diffusion and can produce charge in several pixels (depending on the thickness of the epitaxial layer and the depth of the depletion layer). Of the CCD05 devices examined here only CCD number 15 gave good single pixel x-ray events which could be picked out of the distribution of split and diffuse events. This is probably because the high resistivity (100Ωcm) gives a higher depletion depth (~10μm) and hence a greater number of single pixel events. The thick epi-layer (100μm) for this device also gives a large number of diffuse events but these are easily descriminated against. The other CCD05 devices (12, 13 and 14) did not give x-ray signals that gave easily interpretable results, though some data might be obtainable with more effort.

Previous studies using $Cd^{109}$ x-rays ([9], [25]) did not have sufficient accuracy to study CTE effects in detail. Only an approximate upper limit of 0.99996 per pixel transfer for charge deferred into trailing pixels (column direction) was found. In this study the radiation-induced dark charge was small and was further decreased by:

i) using dither clocking and surface inversion

ii) operating at 15°C

iii) reducing the integration time by fast dumping of all apart from 3 bands of 64 lines which were readout normally (fast dumping carried out by line transfer at the normal rate : 0.5MHz but binning 16 lines into the output register and also increasing the pixel rate to 8 MHz and disabling data capture by the frame grabber).

X-ray data were obtained by first taking an image under x-ray illumination and then subtracting an average of 16 dark reference frames (so as to remove pixel dark signal nonuniformity). The difference image was then searched for events greater than 70% of the peak x-ray signal. Data from blocks of 5x5 pixels centred on the event were then stored in the data logging computer. This was done on repeated images until a total 4,000 events had been captured.

The resulting data file was then processed to eliminate events with x-ray signals spread over more than one pixel (discrimination threshold = 10% of peak x-ray signal). This reduced the file size by about half (to ~2,000 events). These data were then sorted by line number and the data summed for each image band (of 64 lines) to form an average 'event' (block of 5x5 pixels).

Figure 4.1.2-1 shows the x-ray signal for single pixel events as a function of position in the CCD image (ie. as a function of the number of transfers in the storage region). It is seen that there is a linear relationship. The slope gives a CTE of 0.99988 per pixel transfer in the parallel direction after 2 krad. The corresponding fluence is $3.58 \times 10^9$ p/cm$^2$ giving a damage constant (CTI divided by fluence) of $3.4 \times 10^{-14}$ cm$^2$ at 15°C.

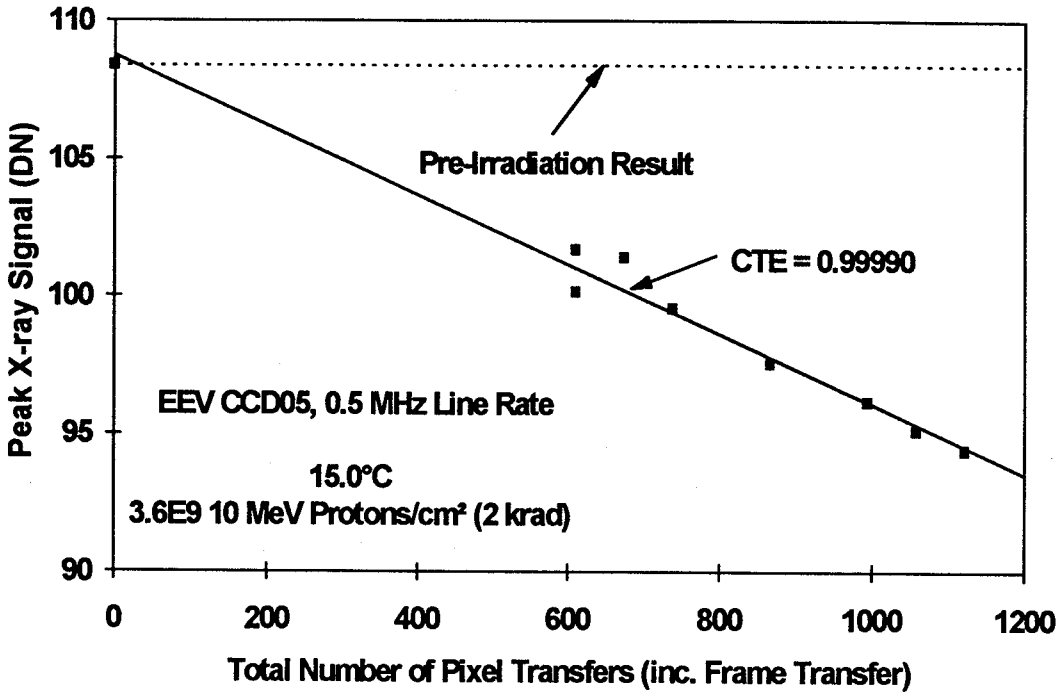


**Figure 4.1.2-1 X-ray measurements of charge loss**

For the unirradiated portion of the devices there was no charge deferred to trailing pixels in either the row or column directions - measured to an accuracy of 0.5% of the peak signal. This indicates a CTE of 0.999995 per pixel for both directions. This result is also shown - plotted for zero transfers since the CTE is so good in comparison with post-irradiation data.

Data for the 1 krad and 4 krad regions of device 15 were not of such good quality because of experimental difficulties in setting gains and thresholds. However the data is consistent with CTE being proportional to fluence (which has also been verified by other workers ([6], [26]).

Figure 4.1.2-2 shows charge deferred into the first trailing pixel in the column direction. It is seen that the plot has a reduced slope compared with figure 4.1.2-1. This is because some of the charge which is trapped (and lost from the peak signal) is re-emitted on a timescale longer than the time between vertical line moves; hence it is spread over several pixels and is not measured as deferred charge. In other words the difference between charge lost and charge deferred into the first trailing pixel is explained in terms of the emission time constant.

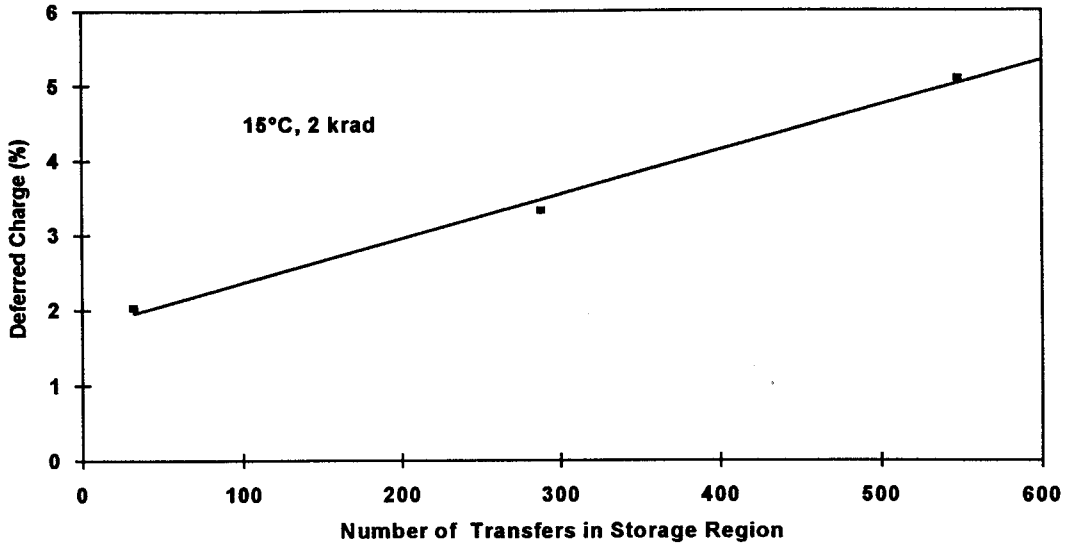


**Figure 4.1.2-2 X-ray measurements of deferred charge**

As we saw in section 4.1.1, we expect the emission time constant at 15°C for the P-V centre (E=0.44 eV) to be 10-20μs. This is much less than the time between line moves during readout (= 850 x 1μs in this case) thus giving charge deferred only to the first trailing pixel. During frame transfer however the time between line moves is 2μs which is much less than $\tau_e$ for the P-V centre and so we expect charge to be spread over several pixels. Interestingly, however, we see from figure 4.1.2-2 that there is significant deferred charge even at the top of the image: ie. immediately at the end of frame transfer. Also there is significant charge deferred to the second trailing pixel. This suggests that there are 'fast' traps present, with time constants comparable with 2μs, either because of reduced energy level (shallower traps) or because of field enhancement. In fact a field strength of only $10^4$ V/cm would give the required reduction in $\tau_e$ [24].

### 4.1.2.2 Serial CTE

The x-ray technique was extended in an attempt to obtain an accurate measure of the serial CTE. The readout register was operated as a linear CCD by using a timing waveform that reverse clocked the image and storage regions and allowed the readout register to integrate charge before readout. To measure CTE an additional feature was to readout the first 400 pixels and then repeatedly shuffle the remainder sideways by 400 pixels (ie. move it sequentially to the left and then to the right, as shown in figure 4.1.2-2a). X-ray events were recorded as in the previous section. Results for the peak signal (in single pixel events) is given in figure 4.1.2-3 for 8 shuffles (corresponding to an additional 18 x 400 transfers). It can be seen that there is a pronounced discontinuity at column 400 - corresponding to the charge loss for the additional transfers. The discontinuity in average peak height was 8.2% of the peak signal corresponding to a CTI of 0.000011 per pixel. It was found that the charge loss was proportional to the number of shuffles as expected. The dose is somewhat uncertain since for part of the irradiation the proton beam did not cover the readout register. However it is estimated that the average dose was ~1 krad so we have a CTI/krad of ~0.00001 per pixel which is a factor 5 less than for the parallel direction.

Figure 4.1.2-3 was for a pattern of readout clocks which was uneven; ie. the R clocks did not have equal mark-space ratios. Changing to a clock pattern with even mark space ratios did not significantly affect the results (figure 4.1.2-4). The reduced value of CTI for the readout register is presumably because of the fast readout time compared with the capture time constant: Figure 4.1.2-5 shows R clock patterns for uneven clocking. It is seen that the clock overlap time is ~20ns and the dwell time for both the $R_2$ and $R_1$ clocks is ~45ns. These are comparable or less than the capture time constant (cf. Robbins et al [12]). For the remaining $R_2$ phase the dwell time will be ~900ns. Thus trapping is most likely under the $R_2$ phase. For even clocking the times will be ~300ns for each phase.

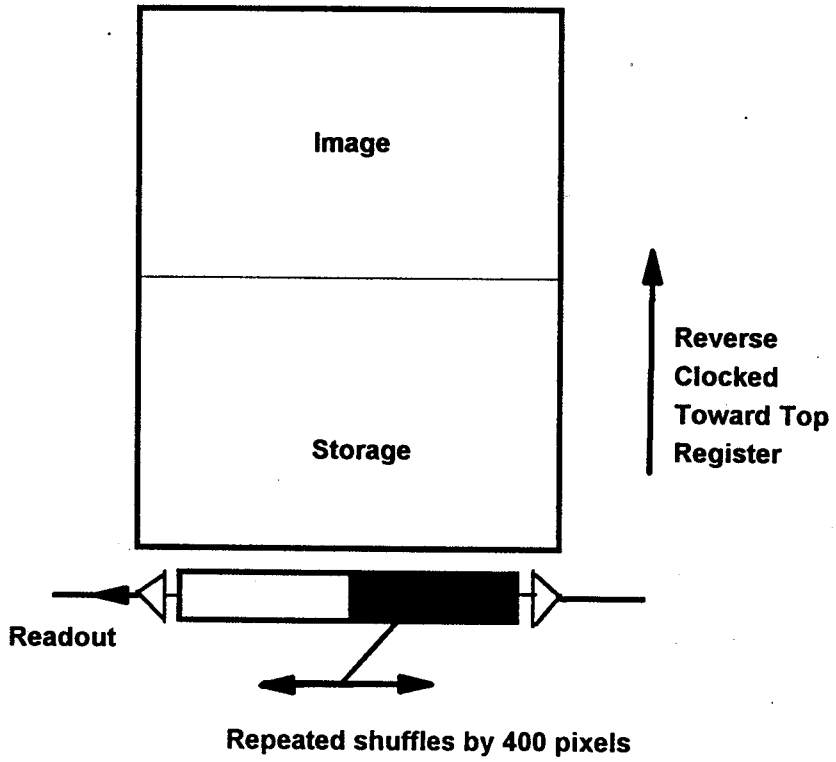


**Figure 4.1.2-2a Clocking scheme for serial CTE measurement.**

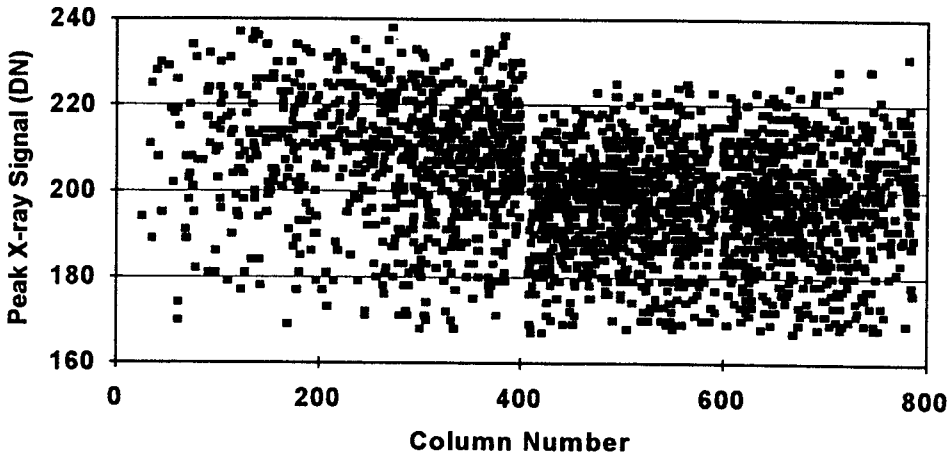


**Figure 4.1.2-3 Peak x-ray signals for the readout register operated as a linear CCD and with charge shuffling for columns 400 to 800. (unequal R clocks).**

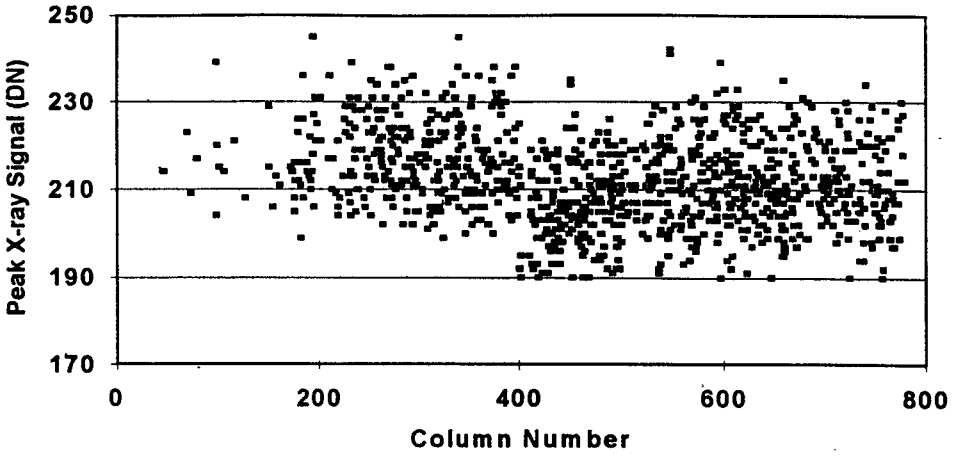


**Figure 4.1.2-4 Peak x-ray signals for the readout register operated as a linear CCD and with charge shuffling for columns 400 to 800. (equal R clocks).**

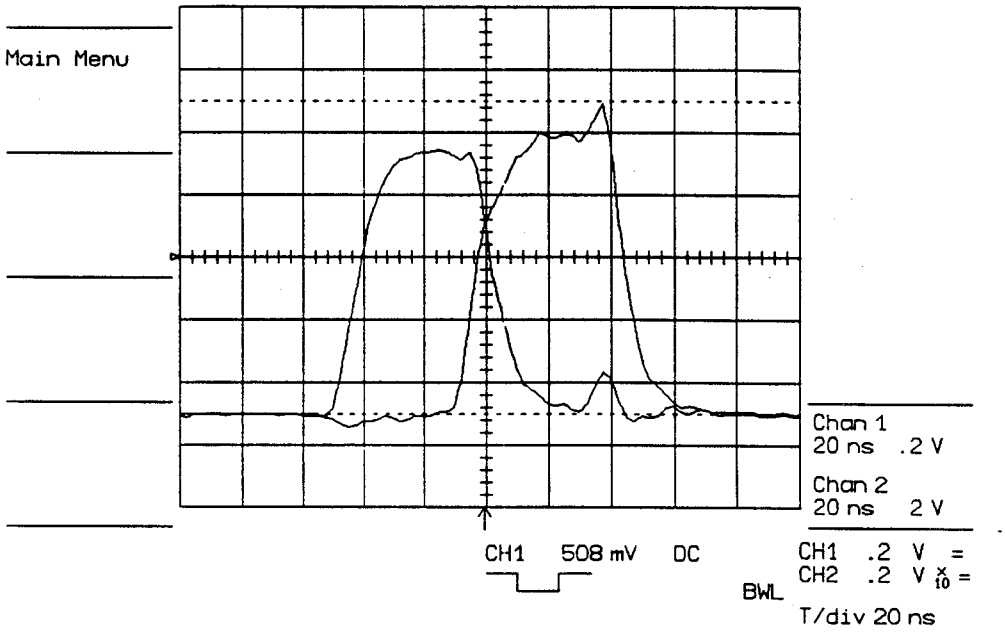


**Figure 4.1.2-5 R clock waveforms for uneven clocking**

4.1.2.3 Interpretation of x-ray data

The value of 3.4 x $10^{-14}$ $cm^2$ for the damage constant for parallel CTE is a factor 10 less than that reported for CCDs developed for the XMM mission ([13]). This is presumably because the clocking speeds are higher for these measurements and hence $t_g$ in equation (6) is a smaller fraction of the capture time constant $\tau_c$. However if we take $t_g$ as 700ns - the time under each gate for these measurements during parallel transfer, then this implies a $\tau_c$ > 1500ns. This value is very much higher than suggested by Robbins et al [12] for signals of several thousand electrons. An alternative is that the CTE is governed more by the overlap time. For serial transfer the CTE is a factor 5 less again for maximum gate times of 900ns (uneven clocks) or 200ns (even clocks). Again this suggests that the overlap time is more important.

4.1.3 Optical Measurements

The x-ray measurements described in 4.1.2 only give CTE data at one signal value (= x-ray energy eV/3.65 electrons) and are only obtainable with devices with an architecture giving good single-pixel events. In this section we consider preliminary results from an optical method designed to give CTE measurements as a function of signal for any device.

The technique relies on imaging a slit illuminated with a broadband Tungsten halogen lamp onto the CCD surface. The slit being oriented along the CCD line direction and the image being ~1 pixel wide for this preliminary investigation (ideally an improved optical arrangement would be used to give slit images narrower than 1 pixel width). After forming an image the charge packets were frame transferred into the storage region in the usual way but were then transferred back into the image region by reverse clocking and again moved back into the storage region. This process could be repeated several times before reading out the charge. Note that each transfer into the image area (from the store) and back to the store involves 1152 pixel transfers. In practice no more than two such charge shuffles were made in order to avoid overheating the clock drivers. The average difference image was formed by subtracting an image with standard readout from one with charge shuffles 256 times. This difference image represents the charge lost due to CTE effects during the shuffling process. It was arranged that the slit illumination was nonuniform along its length. Hence the difference image gives charge loss data as a function of signal.

Figure 4.1.3-1 shows data for device 12. This is for the 4 krad (10 MeV proton) dose region of the device for 2, 1 and 0 shuffles showing that the loss is proportional to the number of shuffles (each of 1152 pixels) and to signal. Figure 4.1.3-2 shows data for the 1, 2 and 4 krad regions of the same device showing that charge loss is essentially proportional to fluence - as we expect. From this data (point x of figure 4.1.3-1) we get a CTI/krad (= charge loss/signal x number of transfers x dose) given by:

$$\text{CTI/krad} = 4.6/30 \times 1/(2 \times 1152) \times 1/4$$

$$= 0.000017 \text{ per pixel transfer (15°C)}$$

ie. for 2 krad CTE = 0.99997 per pixel transfer. Since 1 krad is equivalent to a fluence of $1.79 \times 10^9$ p/cm$^2$ we have a damage constant of $9.3 \times 10^{-15}$ cm$^2$ at 15°C. Note that in this method all the line transfers are at a fast (0.5 MHz rate). From this data there was no evidence for fast traps - ie. no charge deferred into the first trailing pixel.

Figure 4.1.3-3 shows data for device 15 (the device for which we have x-ray data) for 4, 2 and 1 krad. Taking the 4 krad data we have (point x)

$$\text{CTI/krad} = 4.0/20 \times 1/(2 \times 1152) \times 1/4$$

$$= 0.000022 \text{ per pixel transfer (15°C)}$$

ie. for 2 krad CTE = 0.99996 per pixel transfer (15°C) and damage constant = $1.2 \times 10^{-14}$ cm$^2$ at 15°C. Again there was no evidence for fast traps. However the 2 krad data for low signals (<20,000 electrons) gives a charge loss similar to the 4 krad data ie. a CTI/krad of 0.000044 per pixel and a damage constant of $2.4 \times 10^{-14}$ cm$^2$ at 15°C. This is very close to

the x-ray value for the same device (3.4 x $10^{-14}$ $cm^2$ at 15°C). It could be that existence of the fast traps (which give the deferred charge on fast transfers) is signal dependent and that they only have an effect at low signals, for this device - and not for the 4 krad region (left hand side) of the CCD.

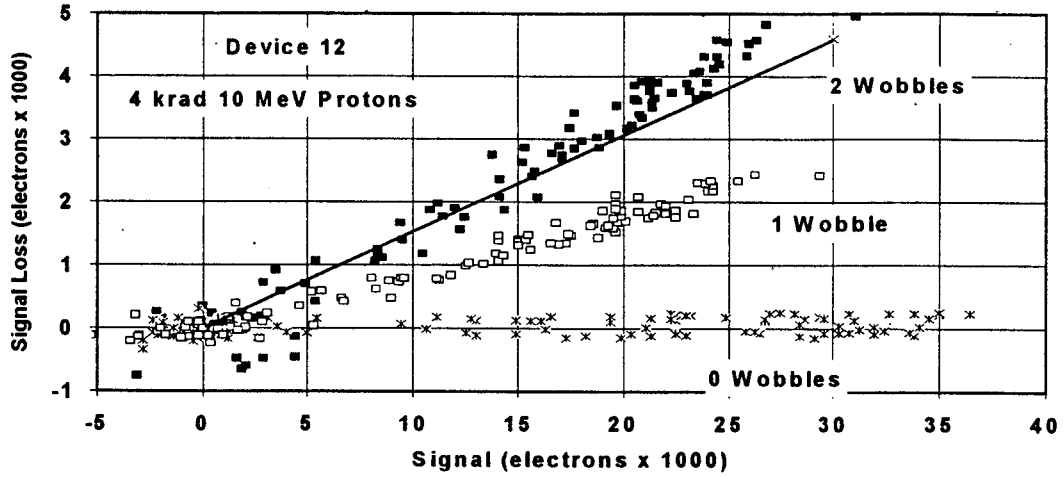


**Figure 4.1.3-1 Signal loss versus signal for device 12 after 2 krad**

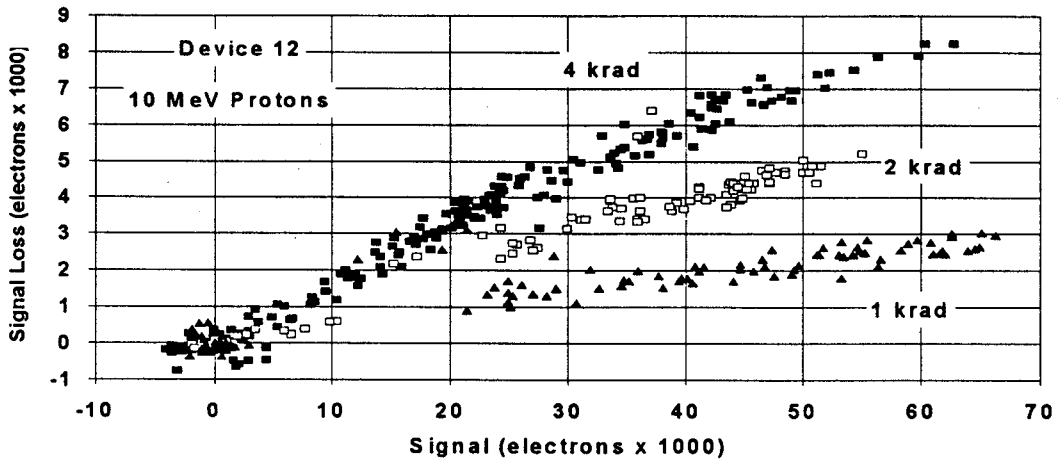


**Figure 4.1.3-2 Signal loss versus signal for device 12 after 4, 2 and 1 krad**

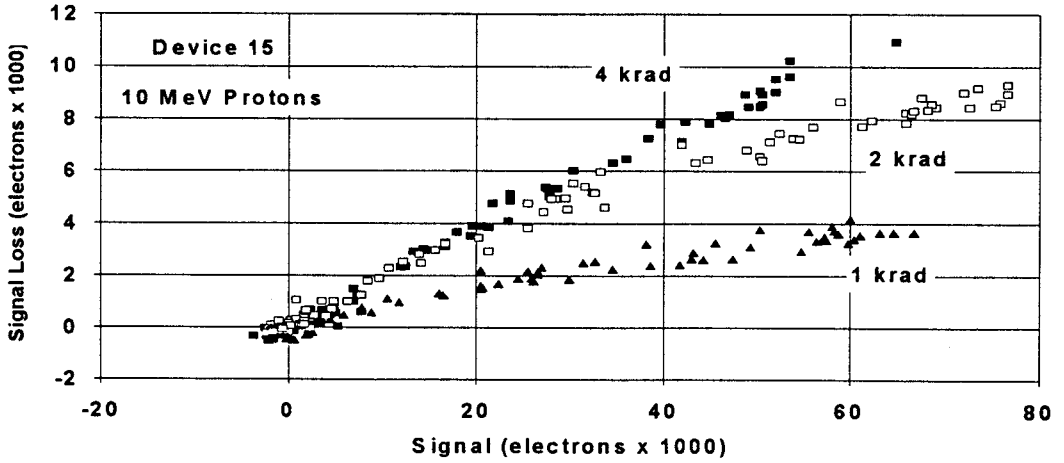


**Figure 4.1.3-3 Signal loss versus signal for device 15 after 4, 2 and 1 krad**

## 4.2 Effect on Dark Charge

Bulk displacement damage causes the production of dark charge generating states within the depletion layer. The effect for low fluences (eg. as experienced for MERIS) is a small increase in average dark current and an increase in dark current nonuniformity - seen as a 'tail' on histograms of dark charge for each pixel.

In this section the majority of results were obtained using dither clocking so as to reduce the contribution due to surface leakage. In this section we make the distinction between average effects (resulting from the majority of pixels) and anomalous effects due to the small number of large dark current spikes (believed to be due to field-enhanced emission).

### 4.2.1 Average Effects

The following points can be noted:

i) The shape of the dark charge histograms is similar for all the devices tested. Figure 4.2.1-1 shows results for CCD05 devices 12 and 15 and figure 4.2.1-2 for all proton damaged devices (at $V_{SS}$ = 7.5V). Note that device 03, which has the widest histogram in figure 4.2.1-2 had relatively poor surface dark charge suppression when using dither clocking. The above histograms were obtained after 3 months storage. Note that device 15 has a high resistivity (100Ωcm) and hence a larger depletion depth (~10μm).

ii) The shape of the histograms - ie. the bulk dark charge is not affected by dither clocking - except for a slight broadening (device dependent) due to the presence of surface dark charge - cf. figure 4.2.1-3.

iii) The bulk dark charge reduces with time after annealing (figure 4.2.1-4).

iv) The effect of fluence can be seen in figure 4.2.1-5. Increased fluence causes a broadening in the histogram, as might be expected.

The shape of the histograms can be modelled using the theory of Marshall et al [27]. These authors give data for nuclear cross sections, damage energies and damage variances at 12 MeV. If this is used in our 10 MeV case then the theory predicts histograms as shown in figures 4.2.1-1 and 4.2.1-6, for a damage constant given by:

damage constant = 2.38 nA/cm$^2$ (21°C) per MeV of damage energy deposited.

The plots are labelled with the number of elastic and inelastic collisions per pixel and the sum distribution is also shown. It is seen that the fit to the data is good apart from at high dark currents. The results are dependent on the interaction volume chosen for the device. Here we assume a depletion area of 22.5 x 16.5μm$^2$ (6μm channel stops) with a 4μm depth (1500μ$^3$ active volume). The same parameters were used for all the plots so it appears that the theory gives a good explanation of the dark current distribution at any fluence. Figure 4.2.1-7 gives another plot (same theory) for the 3 krad region of devices irradiated during the previous SILEX programme [9]. Again

the fit is good. Figure 4.2.1-8 shows histograms for each device 09 for which low regions were each irradiated at 0°, 22.5°, 45° and 67.5° angles of incidence. In each case the fluence (in p/cm$^2$) was kept constant (at 3.58x10$^9$ p/cm$^2$). It is seen that the distributions broaden as the incidence angle increases - as would be expected from the increased track length. Figure 4.2.1-9 shows a theoretical fit assuming a track length increased by a factor sec (67.5°).

Note that the 4μm depth assumed here is not the same as the depletion depth (or the epi thickness). It can be taken as an effective diffusion length for vacancies (and/or interstitials). A similar value (3-6 μm) was found by Wang etal. [27a] in electon irradiated silicon.

v) Figure 4.2.1-7 also shows that the damage is independent of CCD bias.
Data for 2.24x10$^{10}$ 100MeV protons is shown in figure 4.2.1-10. This device was irradiated at the SATURNE accelerator by ESA personnel. It is seen that in this case the fit with theory (63MeV data is the closest available) is not good. However the fit improves dramatically if we choose a damage constant reduced by a factor 1.8 (to 1.3 nA/cm$^2$ per MeV). We suggest that the reduced variance may be due to the escape of fast recoils from the interaction volume (ie. departure from recoil equilibrium) which can occurr at high energies - as discussed previously by Marshall et al [27].

vii) Given a damage constant (K) of 2.4 nA/cm$^2$ at 21°C per MeV, we can calculate the change in <u>average</u> dark current due to bulk damage. This is given by

$$\text{average bulk dark current} = K(n_e E_e + n_i E_i)$$

Where n is the number of collisions and E the average energy deposited (in MeV). The e's and i's refer to elastic and inelastic collisions respectively.

For a fluence of 1.79x10$^9$ p/cm$^2$ (1 krad) we have:

$$\text{average bulk dark current} = 2.4 \times (206.2 \times 1.76 \times 10^{-4} + 0.089 \times 0.0765)$$

$$= 0.10 \text{ nA/cm}^2 \text{ per krad.}$$

This can be compared with the average increases in dark current (including ionization damage) found in section 3.

viii) The temperature dependence of the dark current was examined by first studying the behaviour of the image region dark charge (not dithered)- which arises mainly from the surface ionization damage. Figure 4.2.1-11 shows data for device 15. The slope of the plots for the irradiated regions gives an effective activation energy of 0.633 eV, ie. the following relative values (normalised at 21°C):

| Temperature (°C): | 6 | 10 | 15 | 20 | 21 | 25 | 30 | 35 | 40 |
|---|---|---|---|---|---|---|---|---|---|
| relative dark current | 0.266 | 0.381 | 0.596 | 0.922 | 1 | 1.428 | 2.068 | 3.162 | 4.634 |

These factors were used to scale the dark current histograms shown in figure 4.2.1-12 (for devices 12 and 15, 2 krad) ie. to normalise them all to the size they would have at 21°C if the bulk dark current behaves as exp (-0.633/kT). It is seen that the plots are accurately superimposed, indicating that 0.63 eV is indeed the activation energy for the bulk, depletion layer, component. Figure 4.2.1-13 shows the same for the 1 krad and 4 krad regions of device 12.

The dark current histograms presented so far have a vertical axis expressed as a relative count, that is the shapes of the distributions are correct but the actual (absolute) number of pixels with a given dark current value involves a scaling factor. Figure 4.2.1-13 shows a histogram for device 12 showing the actual number of pixels (out of a total of 770x576) having a dark current within a bin (bin size = 0.0186 nA/cm2). Figure 4.2.1-14 shows the corresponding cumulative distribution (the percentage of pixels with a dark current - mean greater than a given value) - assuming all 770x576 pixels are uniformly bombarded by 2 krad of 10MeV protons ($3.58.10^9$ p/cm$^2$).

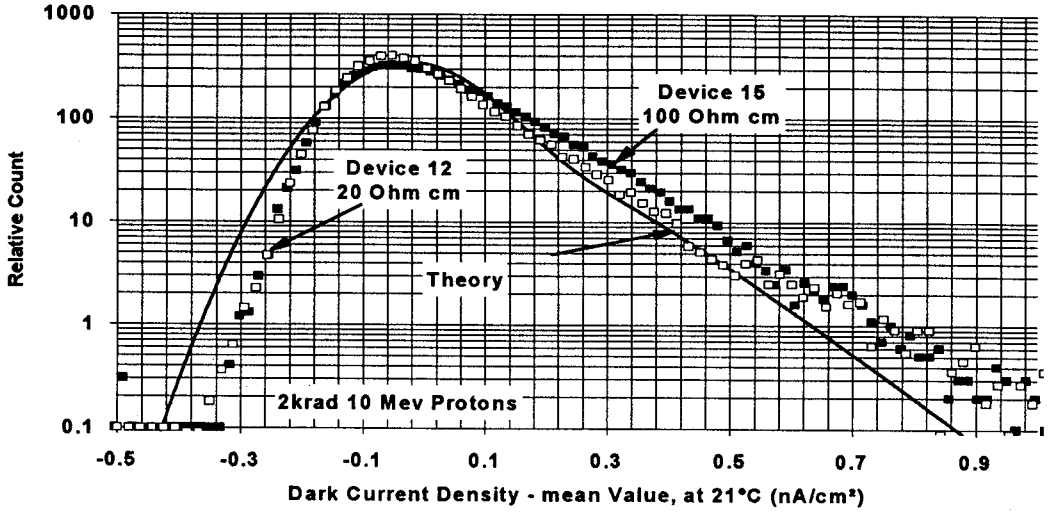


**Figure 4.2.1-1 Dark current density histograms for CCD05 devices 12 and 15 ($V_{SS}$ = 7.5V)**

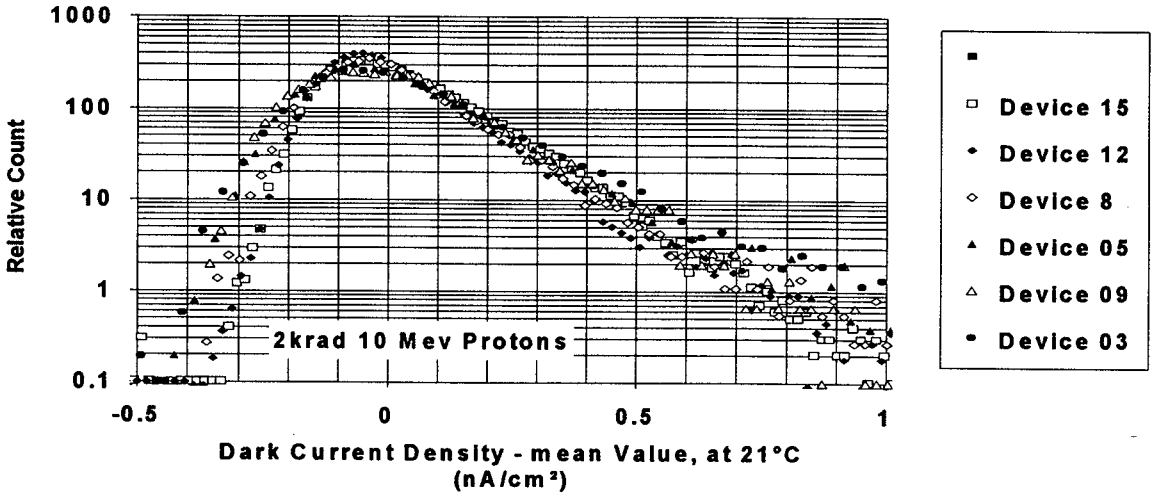


**Figure 4.2.1-2 Dark current density histograms for all proton damaged devices ($V_{SS}$ =7 .5V)**

A/9119/00

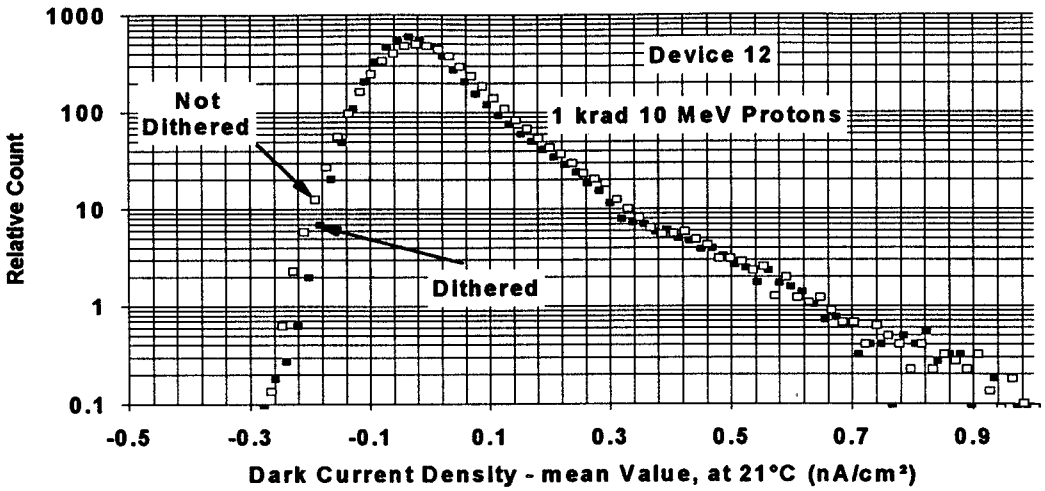


**Figure 4.2.1-3 Dark current density histograms for device 12 (dithered and not dithered, $V_{SS}$ = 7.5V)**

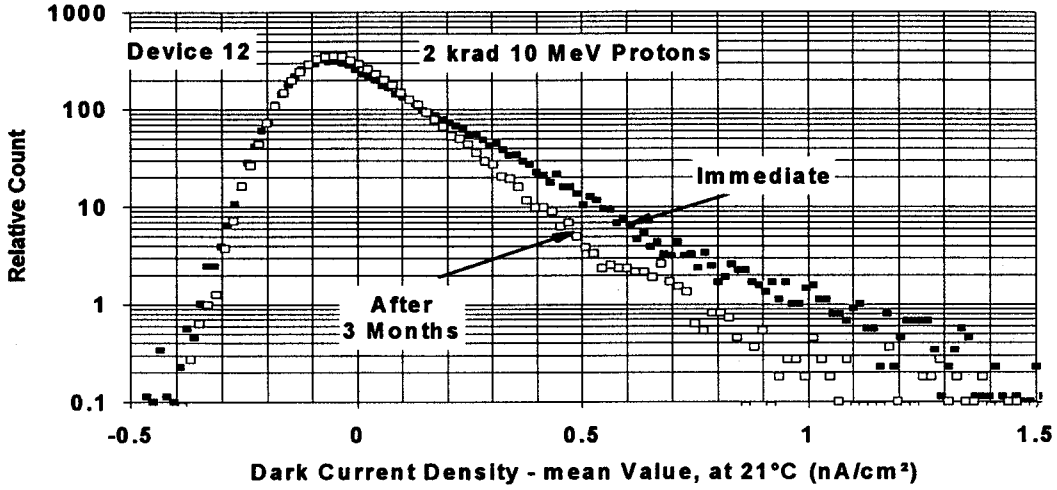


**Figure 4.2.1-4 Dark current density histograms for device 12 immediately and 3 months after irradiation**

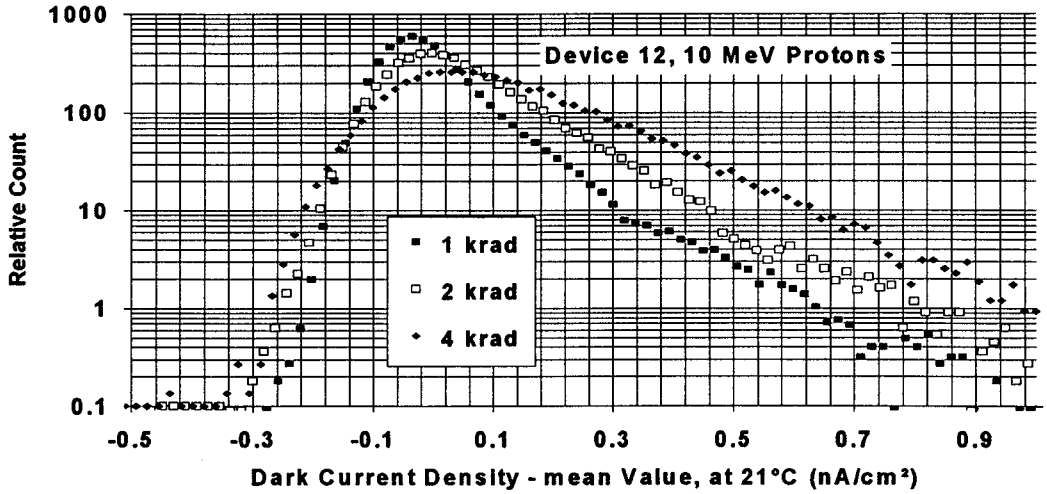


**Figure 4.2.1-5 Dark current density histograms for 1, 2 and 4 krad 10 MeV protons**

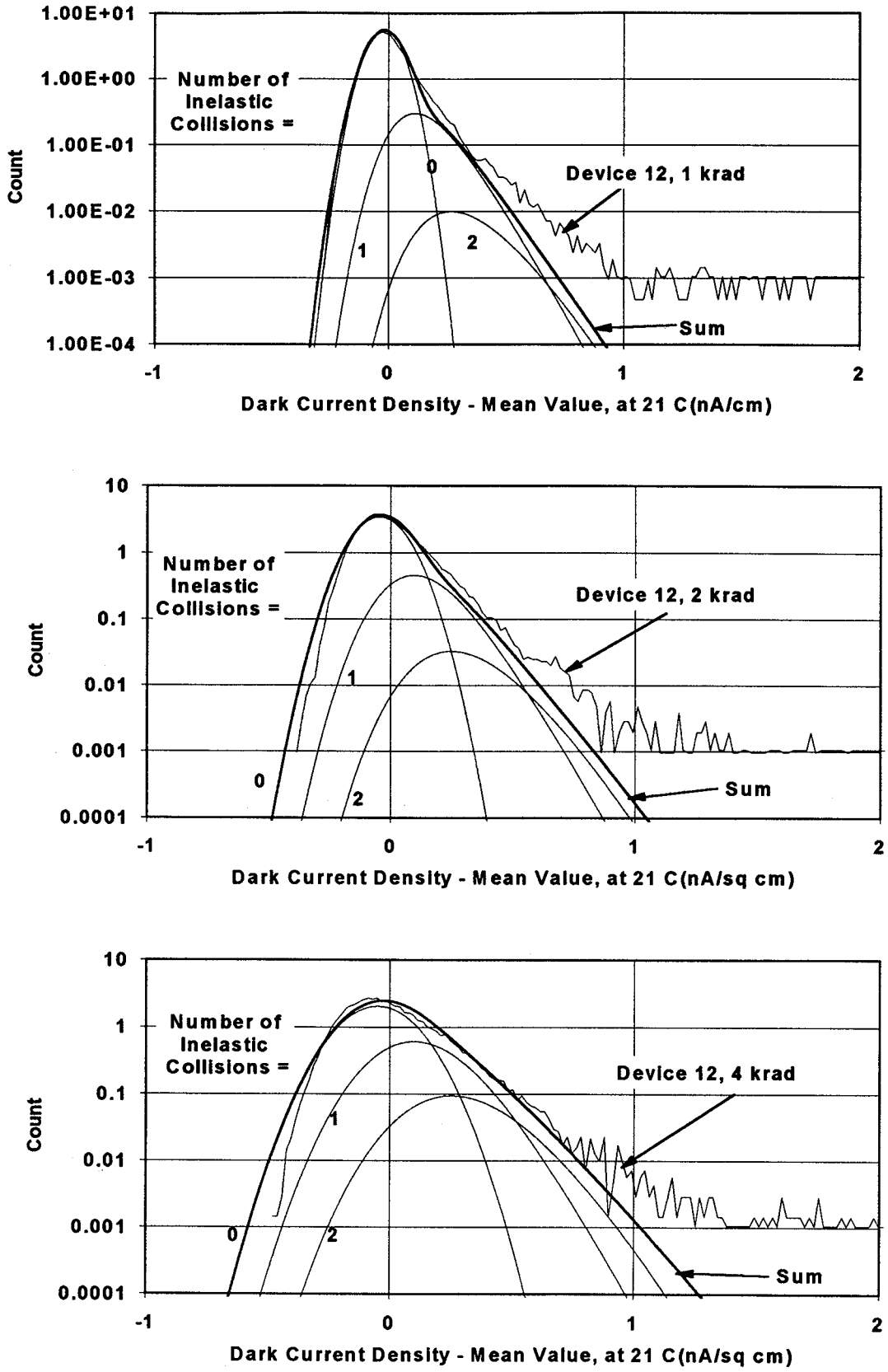


**Figure 4.2.1-6 Modelling of dark current density histograms - plots show distributions for n inelastic collisions per pixel (n = 0, 1, 2, 3, 4, 5) and the sum. Damage constant = 2.4 nA/cm$^2$ at 21°C per MeV**

A/9119/00

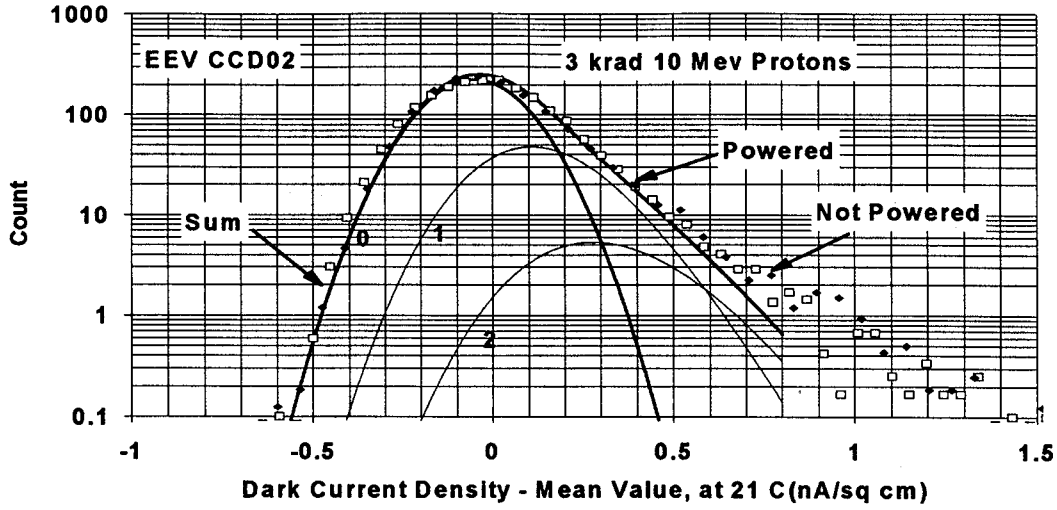


**Figure 4.2.1-7 Dark current density histograms for devices given 3 krad of 10 MeV protons (powered and not powered). Also shown is theoretical fit(as in figure 4.2.1-6)**

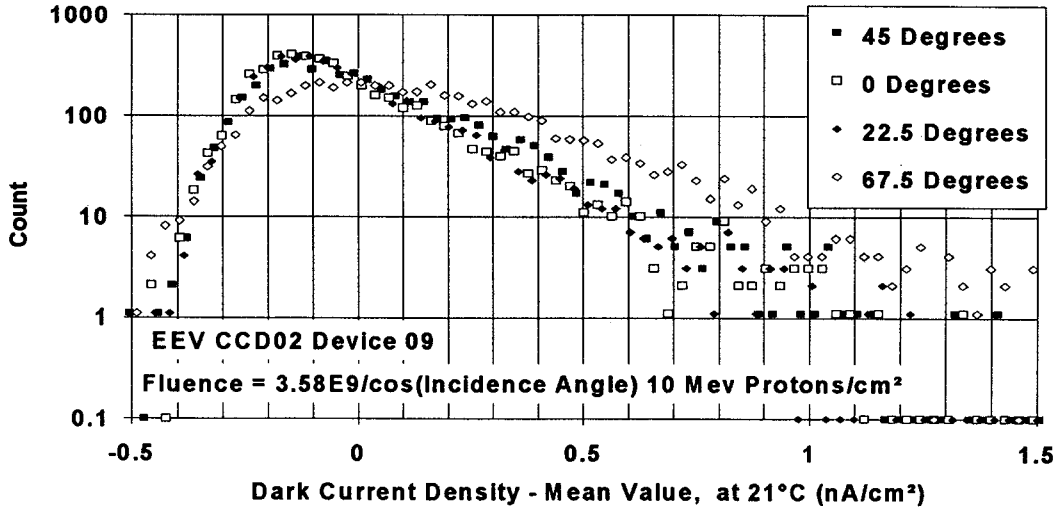


**Figure 4.2.1-8 Dark current histograms for 0°, 22.5°, 45° and 67.5°angles of incidence**

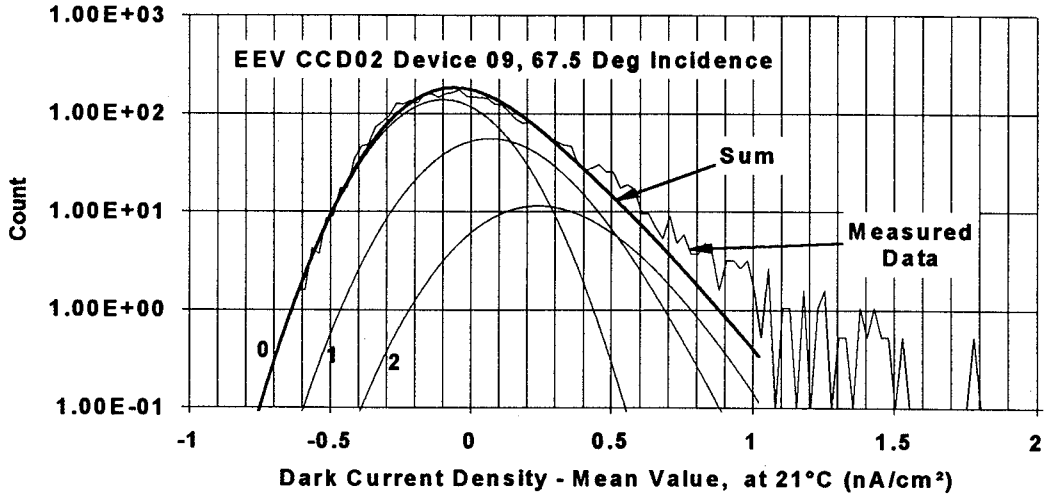


**Figure 4.2.1-9 Theoretical fit to 67.5° data**

A/9119/00

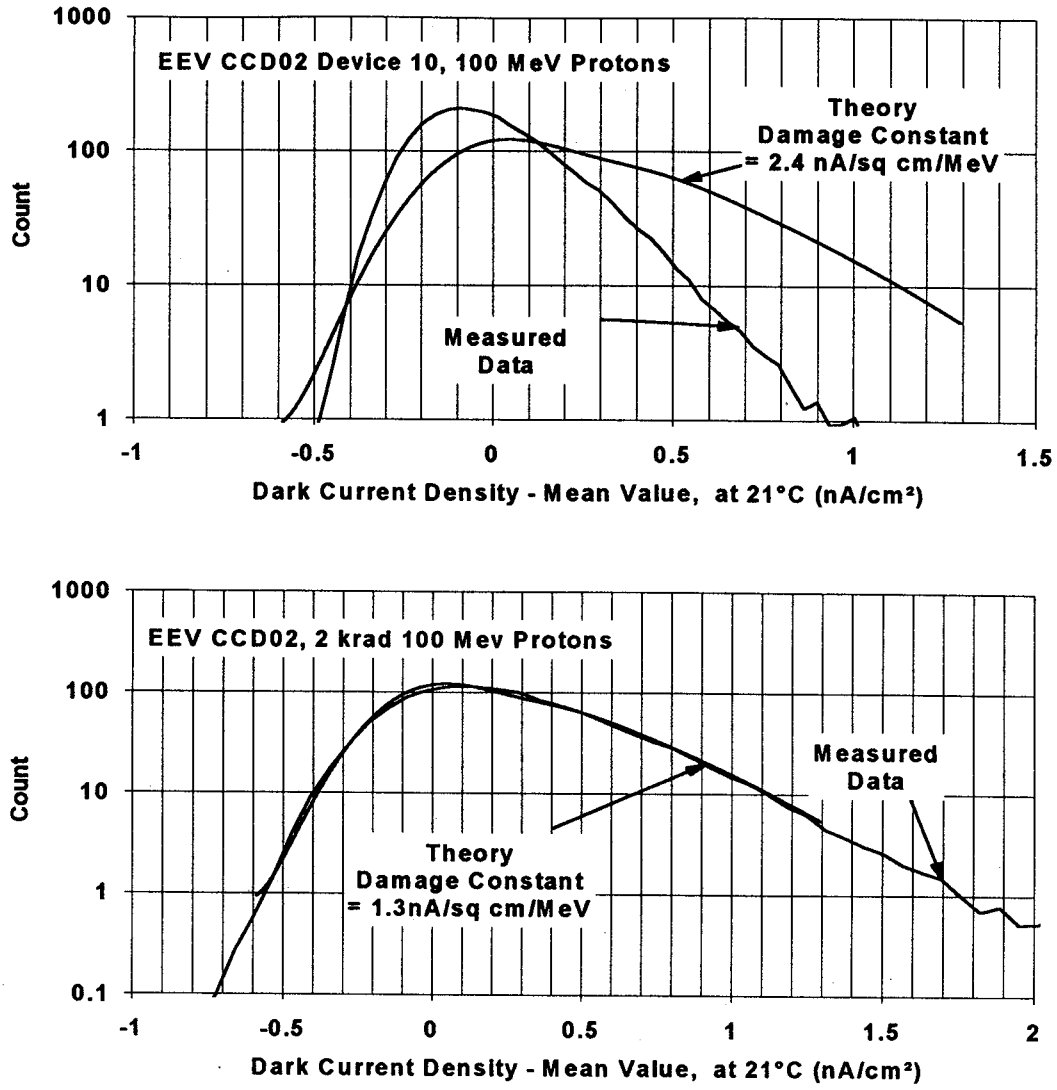


**Figure 4.2.1-10 100 MeV data(fit for 2.4 and 1.3 nA/cm$^2$ per MeV damage)**

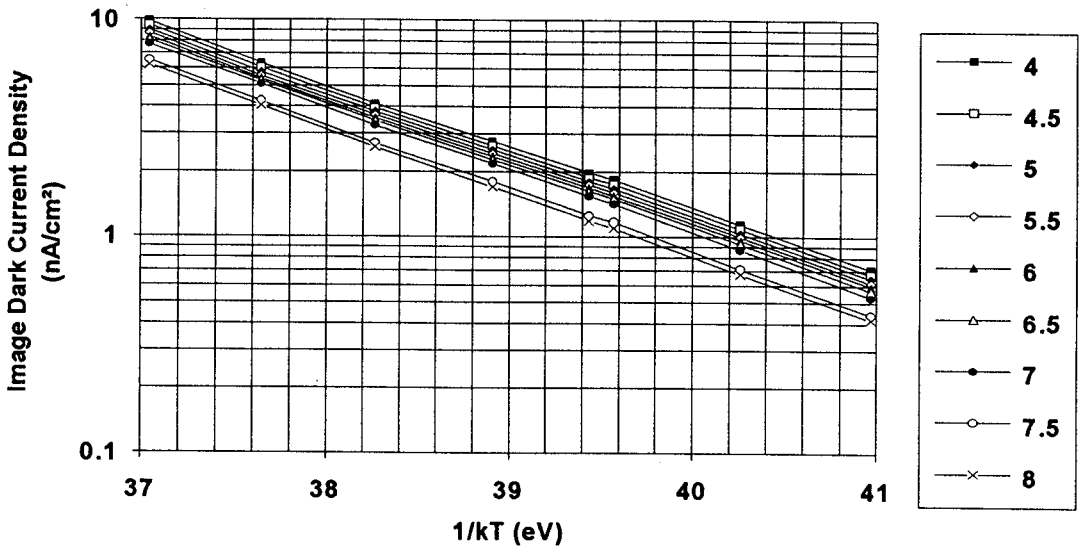


**Figure 4.2.1-11 Average dark current versus 1/kT for device 15**

A/9119/00

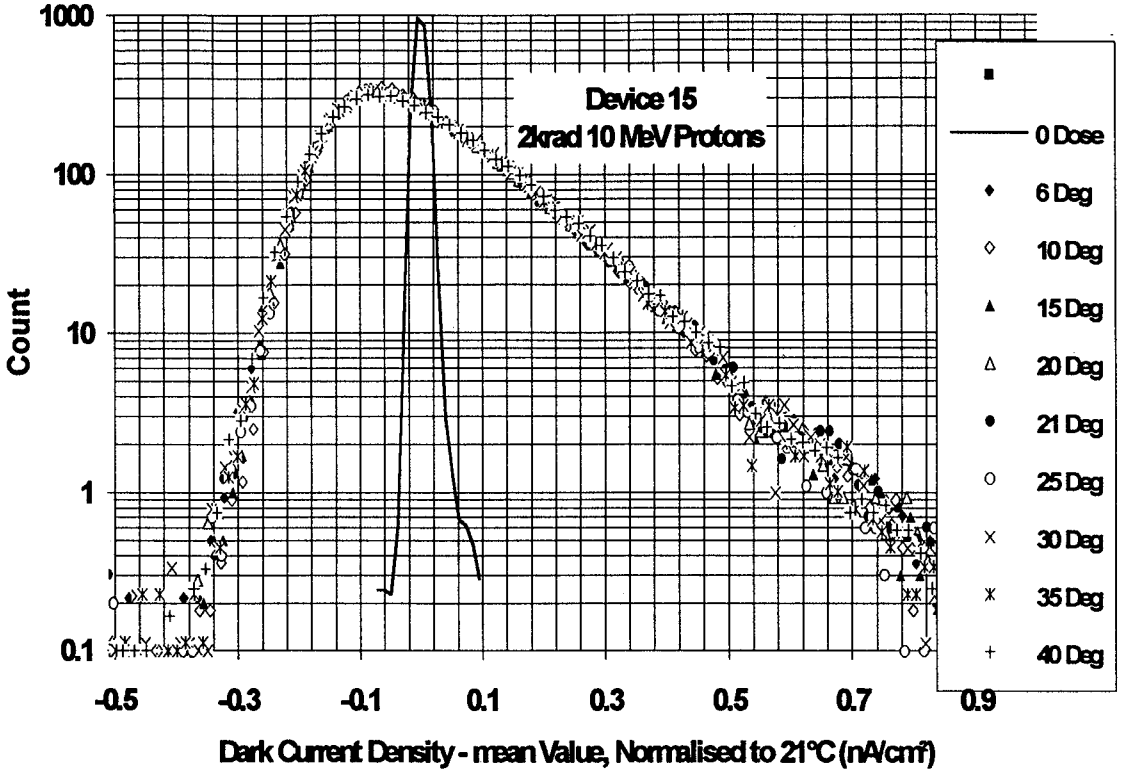


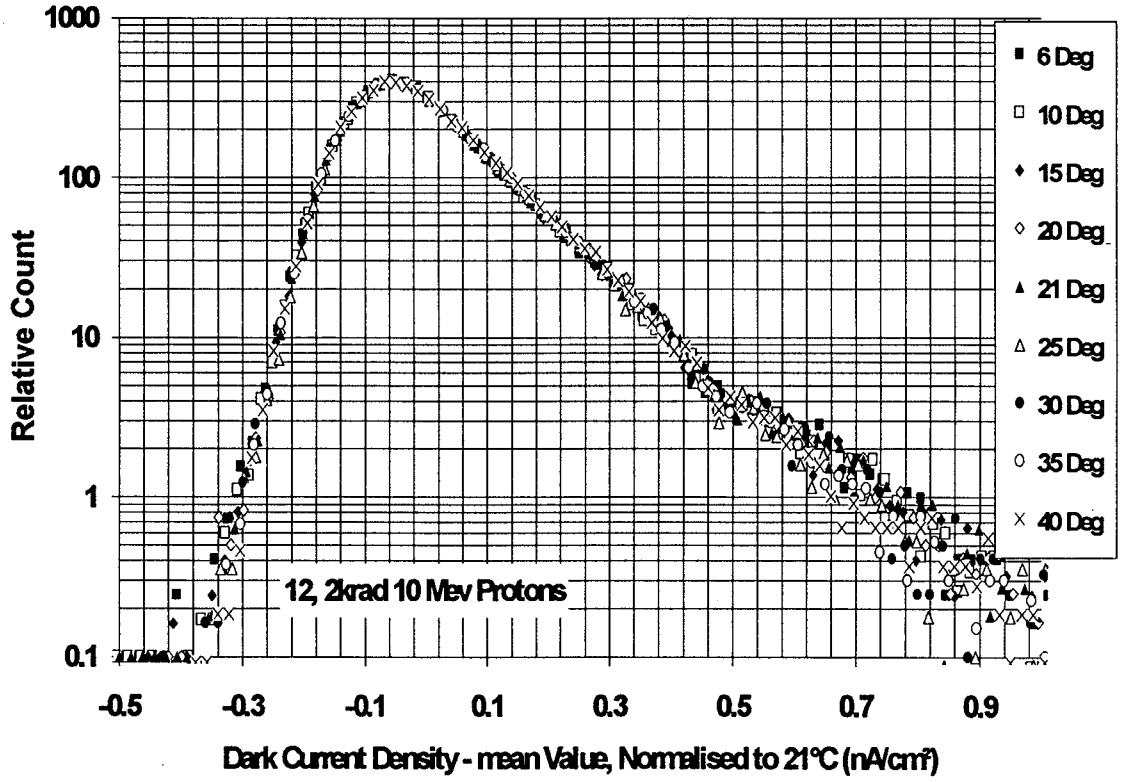


**Figure 4.2.1-12 Dark current histograms for devices 12 and 15 abscissae are scaled assuming an activation energy of 0.633 eV**

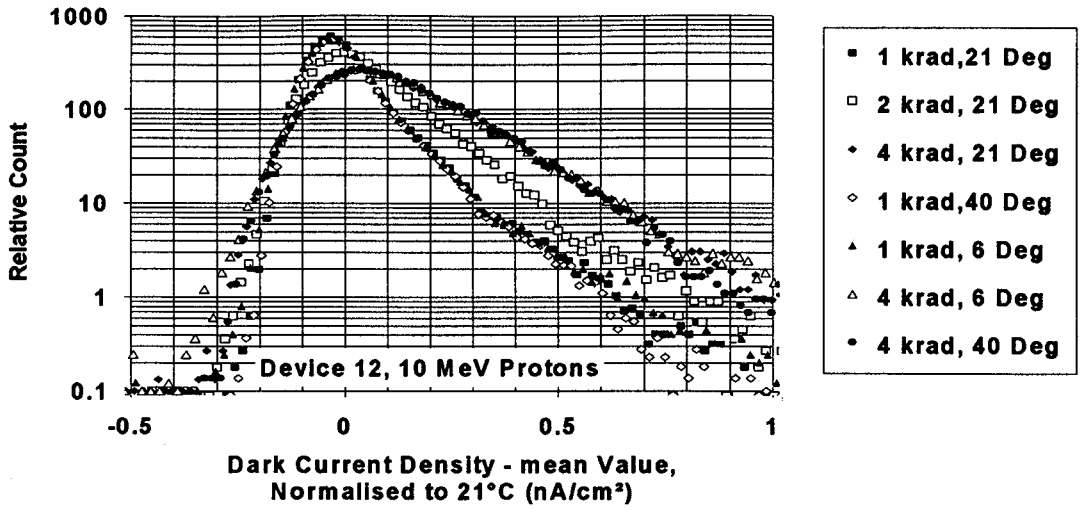


**Figure 4.2.1-13 Dark current density histograms for 1 krad and 4 krad regions of device 12**

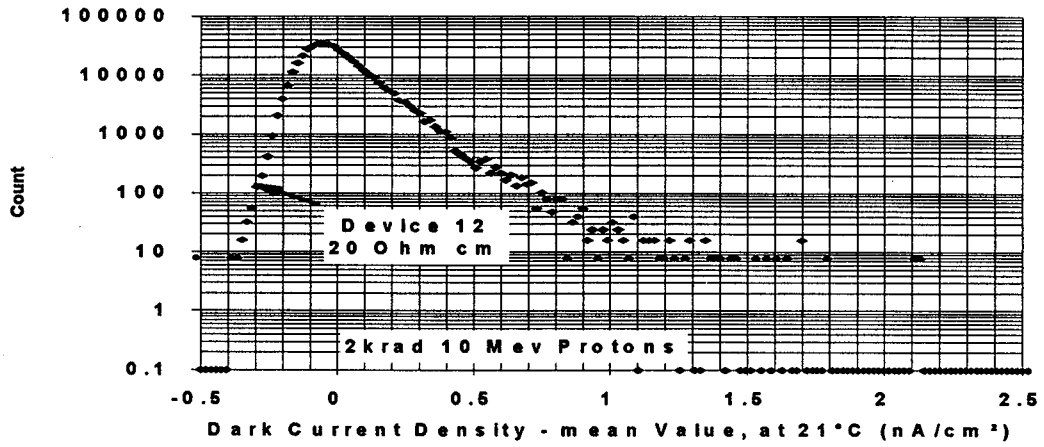


**Figure 4.2.1-14 Dark current density histogram for CCD05 device 12 with pixel count scaled to give absolute numbers of pixels in each bin, for a uniform proton fluence over the device.**

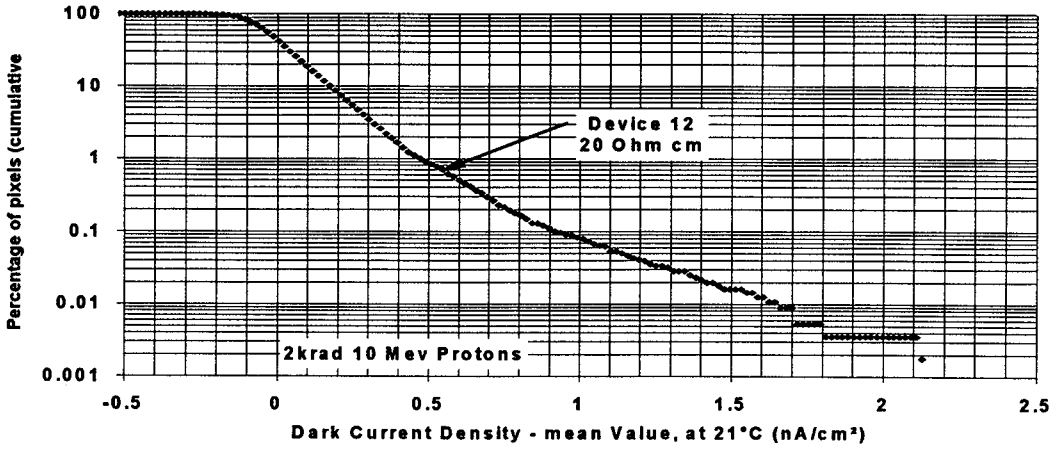


**Figure 4.2.1-15 Cumulative dark current density histogram for CCD05 device 12 , for a uniform proton fluence over the device.**

4.2.1.1 rms dark current uniformity

Figure 4.2.1-16 shows the rms dark current nonuniformity for the image area as a function of 1/kT for devices 12 and 15. The plots are approximately linear with an effective activation energy of 0.60 eV - ie. somewhat smaller then the average value(0.63 eV). Figure 4.2.1-17 shows the variance versus dose - which gives a linear plot as expected from theory [28].

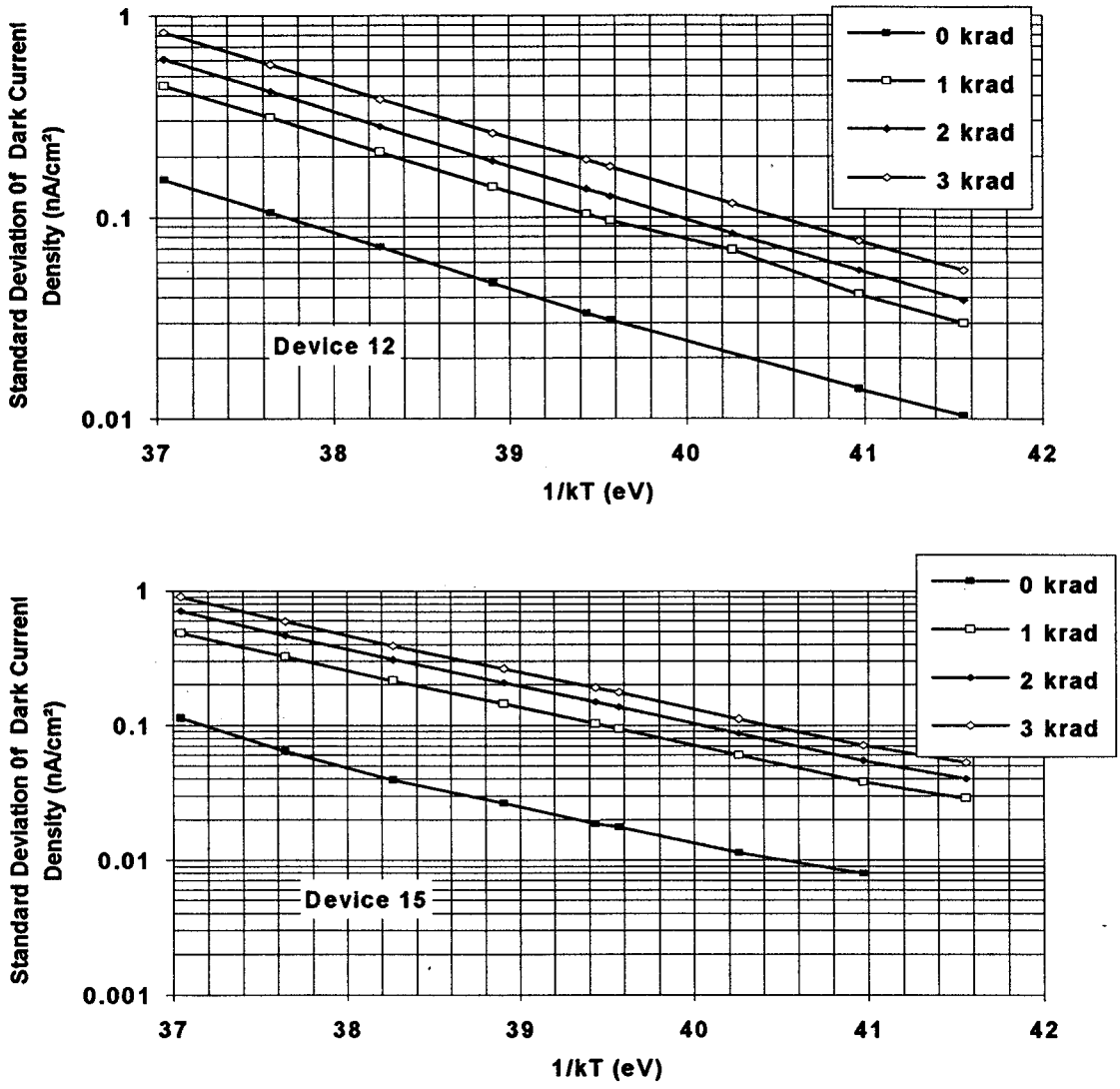


**Figure 4.2.1-16 rms dark current versus 1/kT**

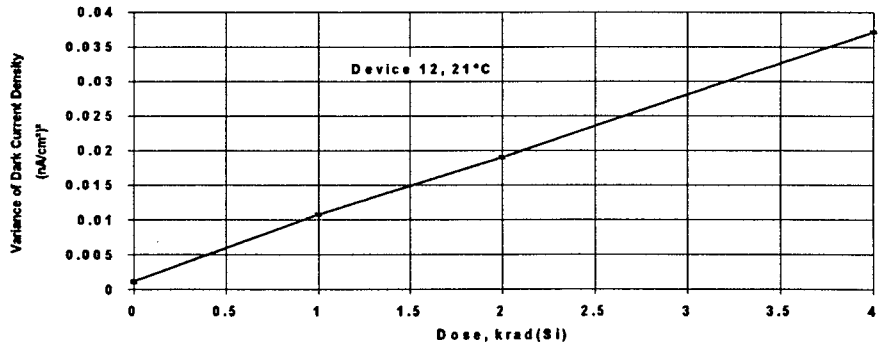


**Figure 4.2.1-17 Variance of dark current density versus dose (device 12)**

### 4.2.2 Dark Charge Spikes

There are a small number of spikes which are anomalously large and lie outside the main distribution at dark current densities of several nA/cm$^2$ (at 21°C). These are thought to be due to field enhanced emission. Anomalous behaviour can be identified using the method of extreme value statistics [27]. A typical plot for an EEV device is shown in figure 4.2.2-1. The plot is a straight line (indicating a common mechanism) for dark currents up to ~1.5 nA/cm$^2$ but there are departures (suggesting other mechanisms such as field enhanced emission) at higher dark currents. Basically the plot shows that these high dark current values cannot be expected simply on the basis of statistical fluctuations. Data on individual dark charge spikes were obtained for CCD05 devices 12 and 15 (10 MeV protons). The brightest 1000 pixels were studied but it should be noted that some individual pixel values may be affected by temporal fluctuations (at the time of measurement) as described in section 4.2.3.

i) Figure 4.2.2-2 shows that the majority of large spikes decrease in size after 3 months storage at room temperature

ii) Figure 4.2.2-3 shows that changing the substrate voltage does not affect the magnitude of most pixels - other than through the change in gain (~10%) of the output amplifier. A few pixels reduce in brightness considerably on increasing $V_{SS}$ from 7.5 to 9.5V - possibly because there is a slight reduction in depletion depth and some defects are no longer contained within the depletion region.

iii) Figure 4.2.2-4 shows dark spikes for dithered and non-dithered I-clock operation at $V_{SS}$ = 7.5V and 9.5V. It can be seen that dither clocking has no significant effect on spike size - as might be expected.

iv) Figure 4.2.2-5 shows dark spike amplitudes versus 1/kT (device 15 gives a similar plot). From the slope of the straight lines we can determine the effective activation energy: shown as a function of spike size in figure 4.2.2-6. There is, however, no obvious trend to figure 4.2.2-6 - other than the possibility of a slight reduction as the spike size increases (trend line shown). Figure 4.2.2-6 shows spike size at 35°C plotted against the size at 6°C. This plot does show a significant effect in that there are groups of pixels showing different activation energies: 0.63 eV for most pixels, but other groups at 0.52 and 0.3 eV. Note that a low value of activation energy implies that spikes cool out slowly. Several hundred pixels will have an activation energy less than 0.63 eV after 2 krad - though relatively few (a few tens) will show a value less than 0.5 eV.

v) It can also be seen from figure 4.2.2-4 that some pixels show erratic behaviour - and large departures from a straight line trend with 1/kT. This is extremely unlikely to be due to the temperature dependence, as such, but is probably due to temporal variations - ie. the pixel value being dependent on the particular time it is measured (and this has been confirmed for several of the anomalous pixels). This is discussed more fully in the next section. Similar behaviour of spikes has been noticed with Thomson-CSF TH7863 devices [10].

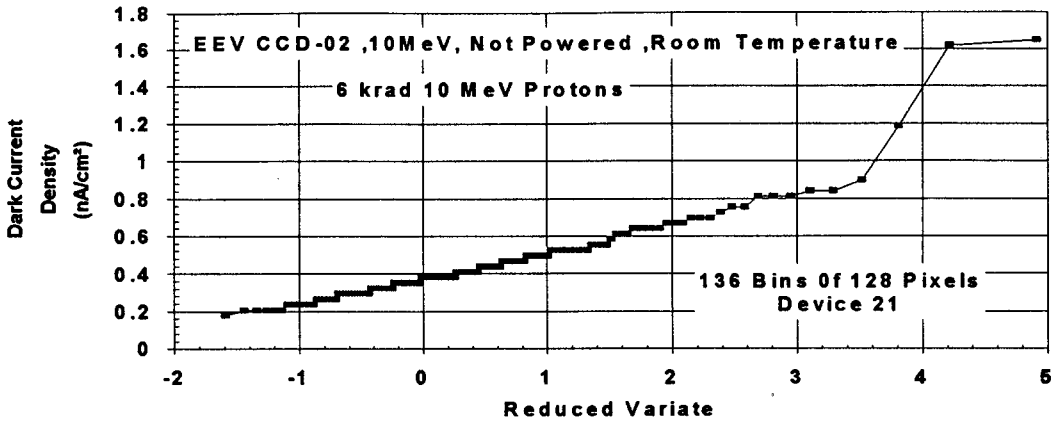


**Figure 4.2.2-1 Extreme value statistics plot for device 21 (6 krad 10 MeV protons)**

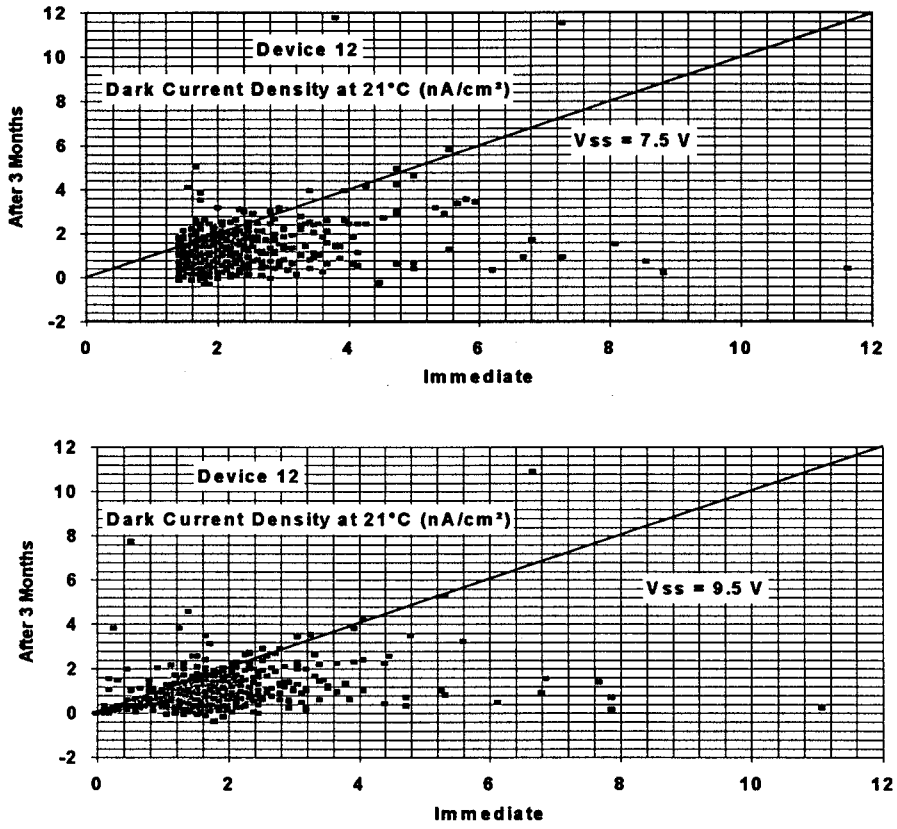


**Figure 4.2.2-2 Dark current spike size (in nA/cm$^2$) immediately and 3 months after irradiation**

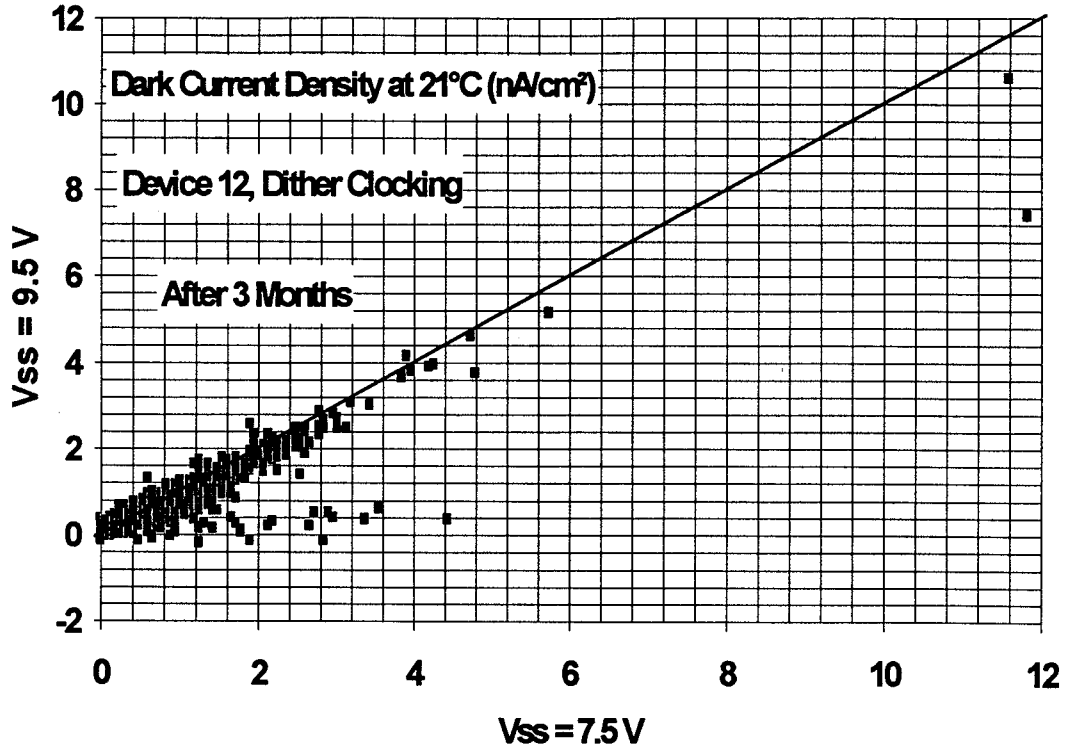


**Figure 4.2.2-3 Dark spike size (in nA/cm$^2$) at $V_{SS}$ = 7.5V and 9.5V**

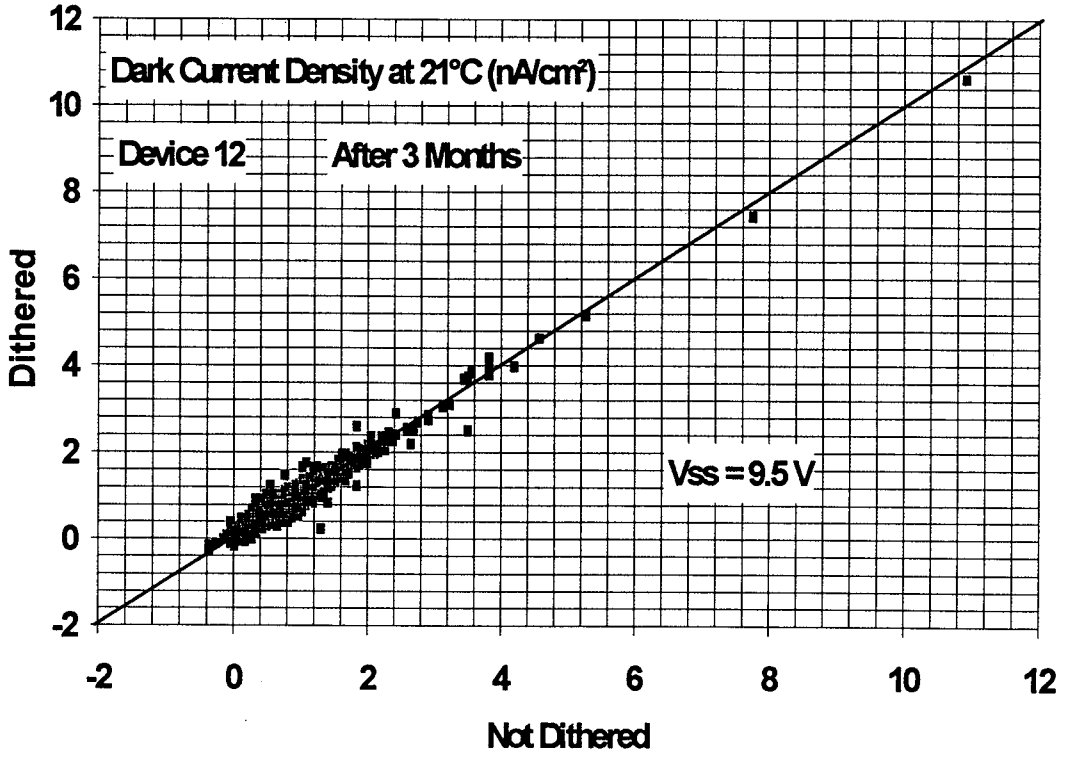


**Figure 4.2.2-4 Dark spike size (in nA/cm$^2$) for dithered and non-dithered I clock operation.**

A/9119/00

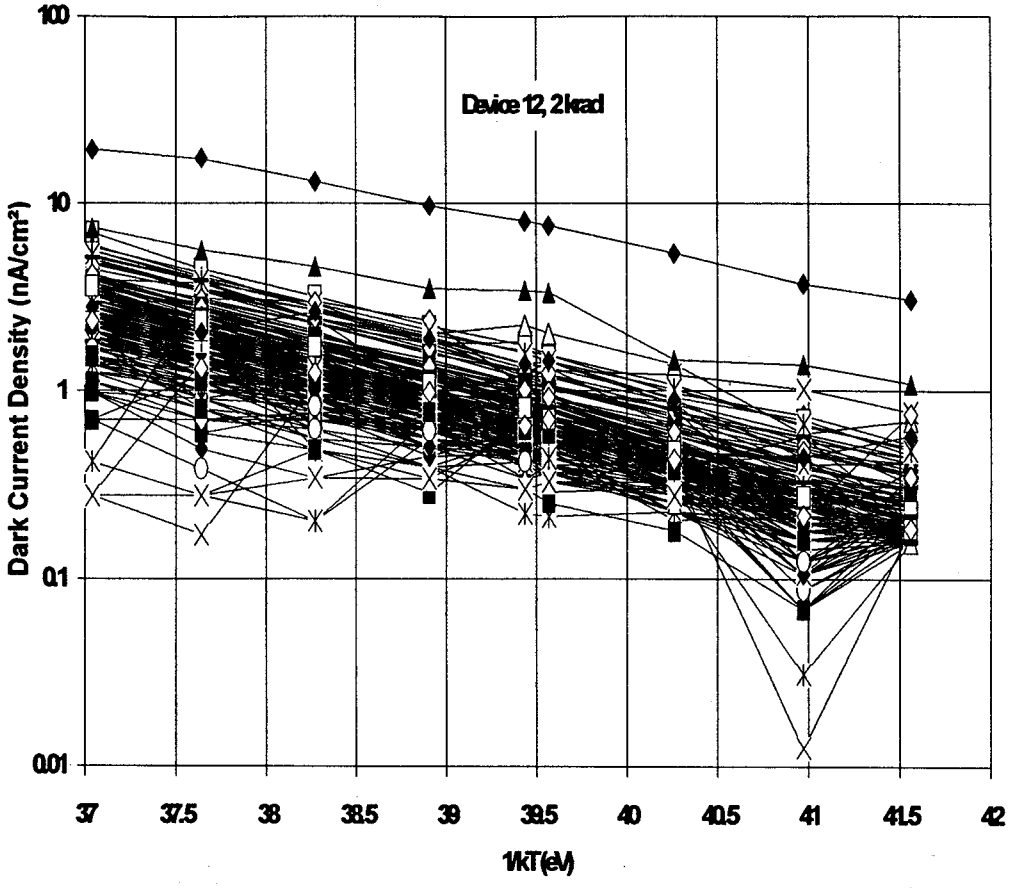


**Figure 4.2.2-5 Dark spike amplitude verses temperature (device 12)**

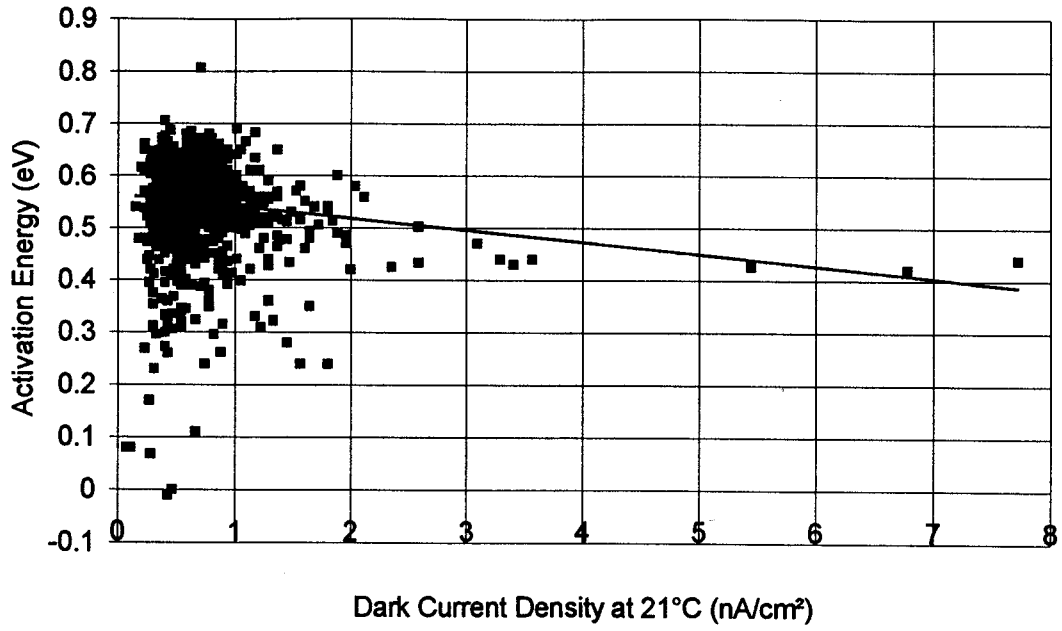


**Figure 4.2.2-6 Effective activation energy versus spike size**

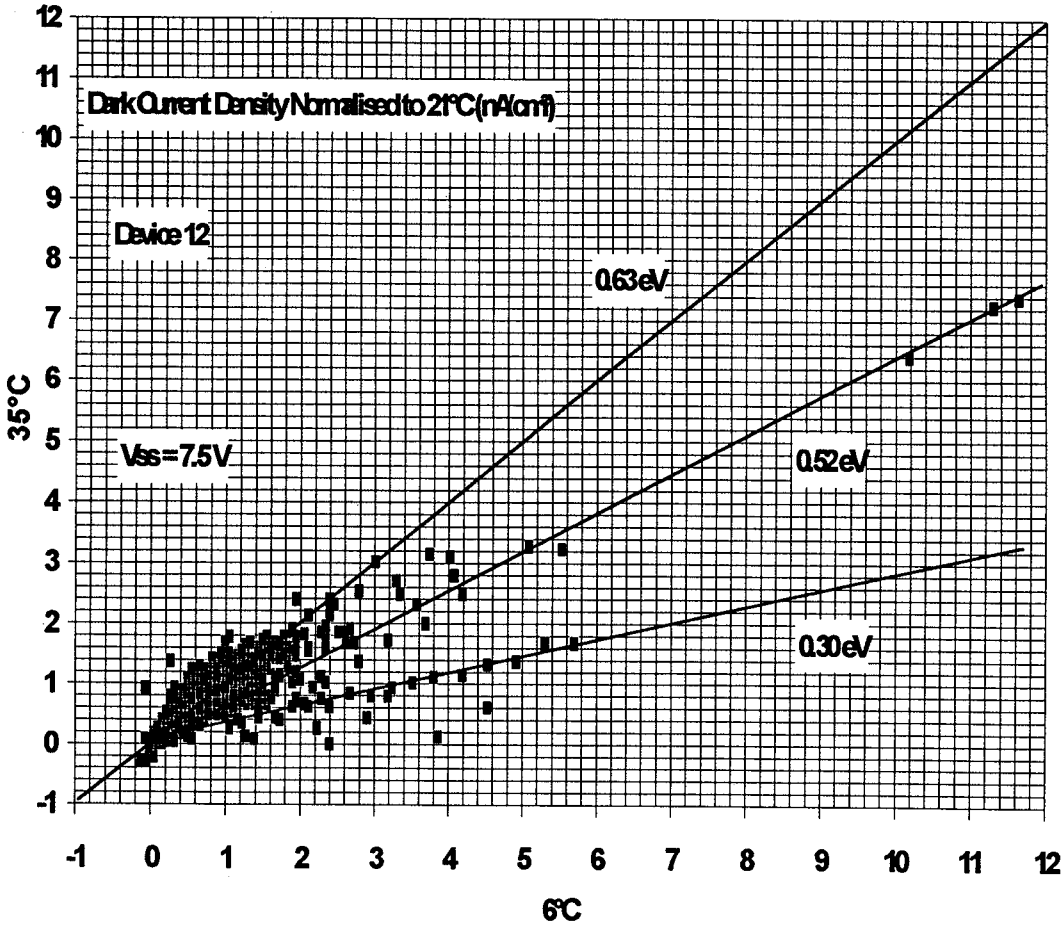


**Figure 4.2.2-7 Spike size (in nA/cm$^2$) at 35° versus size at 6°C**

### 4.2.3 Temporal Stability of Dark Charge

This has been examined for CCD05 device 12 (and to a lesser extent with device 15), irradiated with 10 MeV protons and also for device 14 irradiated with $Co^{60}$ gamma rays.

In order to search for large temporal variations in pixel values a software routine was written which first averaged 16 frames (to remove noise) then subtracted a reference frame (the previous average of 16 frames) and searched for pixels more than 6830 electrons/pixel/s (0.22 $nA/cm^2$) away from the mean, ie. those which made a jump or fall by more than 6830 e/pix/s. This process continued until a list of 200 transitions was generated. In this list (formed over a period ~2 hours) some pixels made several up and down transitions. In fact a total of 105 pixels were found to flip in dark value by more than 0.22 $nA/cm^2$ over the CCD area searched (34%) and this gives a prediction of 310 'flipper' pixels (0.22 $nA/cm^2$) per CCD05 - for roughly 2 krad of 10 MeV proton irradiation. Typical dark current variations are shown in figures 4.2.3-1 and 4.2.3-2.

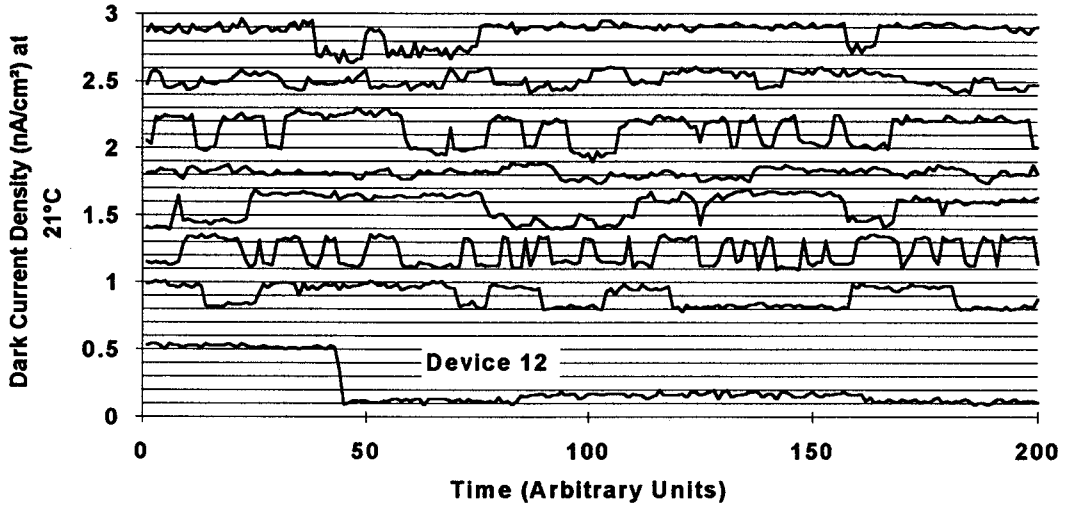


**Figure 4.2.3-1 Large amplitude RTS signals from device 12 at 21°C**

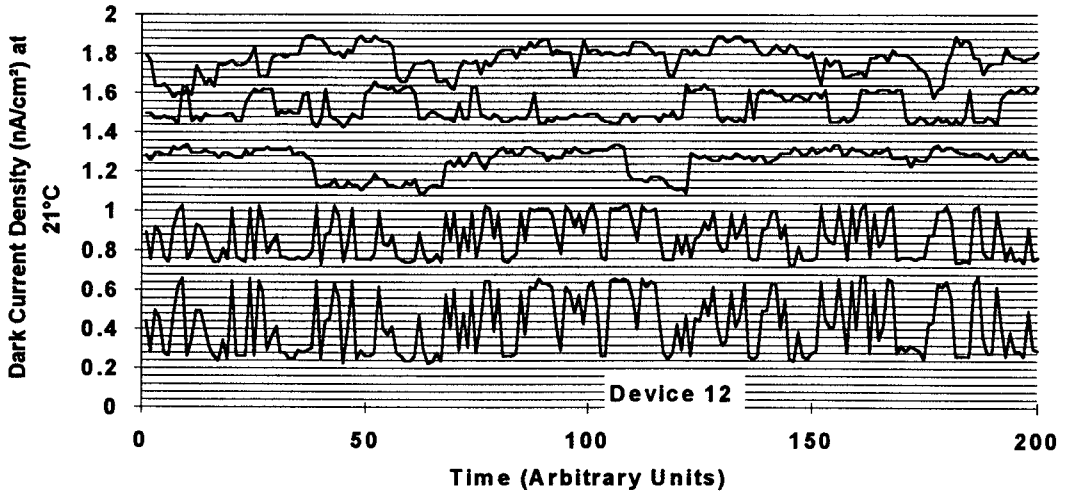


**Figure 4.2.3-2 Large amplitude RTS signals from device 12 at 21°C**

It is seen that the traces give the appearance of random telegraph signals (or RTSs). There is a variety of transition time constants and amplitudes. The largest being ~0.4 nA/cm$^2$ at 21°C. The figures also show 'reference pixels' chosen at random which show essentially flat behaviour. The large amplitude 'flippers' discussed above are in fact the extreme of a distribution of switching behaviour. Looking at the time behaviour of blocks of 9x9 pixels, chosen at random we get plots such as shown in figure 4.2.3-3. There are three basic types of behaviour:

i) sharp transitions from one state to another (sometimes between multiple levels as in cases B or D)

ii) less sharp transitions - or a large number of multiple transitions giving the resemblance of 1/f noise as in case A

iii) steady (flat) levels which only show fluctuations due to system and shot noise (case C of figure 4.2.3-3).

It seems that a large fraction of pixels can show transitions with amplitude ~0.1 nA/cm$^2$ at 21°C with a few hundred 'flipper' pixels with amplitudes in the range 0.2-0.4 nA/cm$^2$. These fluctuations mean that dark current can only be calibrated to ~0.1 nA/cm$^2$ (21°C) at least.

Reducing the CCD operating temperature will reduce the amplitude of the transitions (we already know that most pixels reduce their dark current with an effective activation energy of 0.63 eV). In addition the time constants increase (as illustrated in figure 4.2.3-4).

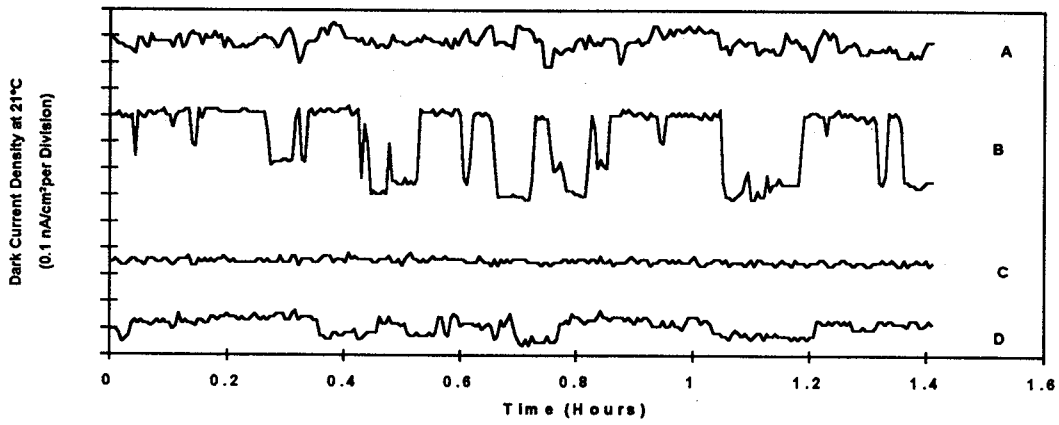


**Figure 4.2.3-3 RTS signals at 21°C**

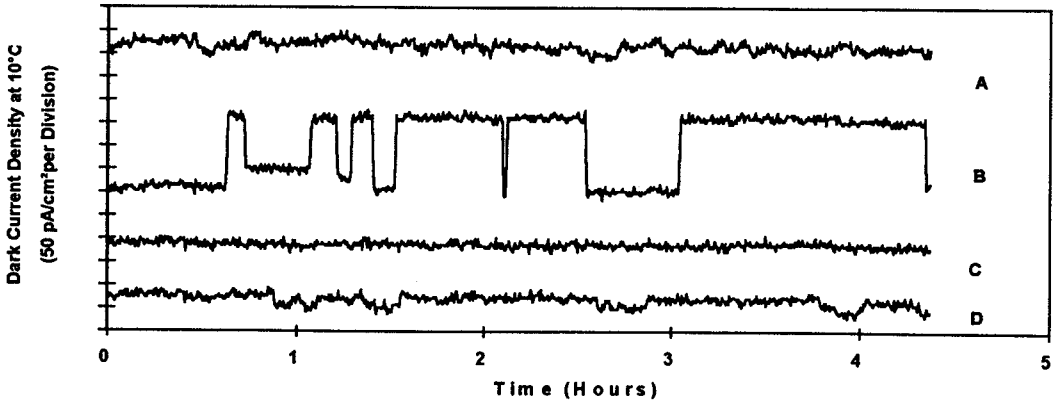


**Figure 4.2.3-4 RTS signals at 10°C**

We can only speculate on mechanisms at present. Sharp transitions in dark current are most likely caused by capture and emission from trapping states - also suggested by the temperature dependence. Recall that

$$\tau_e = \frac{e^{E/KT}}{\sigma_n X_n V_{th} N_c}$$

$$\tau_c = \frac{1}{\sigma_n V_{th} n_s}$$

Thus $\tau_e$ is exponentially dependent on 1/kT. $\tau_c$ has a weak dependence ($V_{th}$ varies as $T^{1/2}$). A detailed examination of the temperature dependence of the time constants may give information on the energy level(s) involved. Random telegraph signals are usually observed as current modulations in small geometry MOSFETs ([29], [30]). In these devices the trapping state is thought to be located just inside the oxide. The field from the charged defect (when it has captured an electron) modulates the channel conductance. Certainly in our case the long time constants imply a very small value for the electron capture cross section $\sigma_n$ of the order $10^{-22}$ cm$^2$ (for $\tau_c$ ~10 minutes) and also a long emission time. This implies that a potential barrier is involved either at the $SiO_2$/Si interface (as is proposed for MOSFET RTSs).

The location in the CCD of the defect responsible is not yet clear, but the RTS effect has only been observed in proton damaged samples - not in unirradiated or $Co^{60}$ irradiated devices. Also the fluctuation amplitudes do not seem to be affected by surface inversion. This implies that we have a bulk effect. The changes in dark current are quite large. If the trapping defect is itself generating the dark current than a mechanism such as field enhanced emission would be needed to explain how so much dark current can come from a single site: for sites with $(\sigma_n\sigma_p)^{1/2}$ ~$10^{-16}$ cm$^2$ (ie. higher than in our case) McGrath et al [31] found dark current densities, $j_B$, of order 1 pA/cm$^2$, without field enhancement. As a check we calculate:

$$j_B = \frac{(\sigma_n\sigma_p)^{1/2} v_{th} q n_i}{2A}$$

where

vth = 1.13 x $10^7$ cm/s at 300K
$n_i$ = 1.45 x $10^{10}$ cm$^{-3}$

for $(\sigma_n\sigma_p)^{1/2}$ = $10^{-15}$ cm$^{-3}$ and A = 22.5 x 22.5μm$^2$

we have $j_B$ = 2.6 pA/cm$^2$ at 300K.

In our case we have flipper dark currents of order 100 pA/cm$^2$ or larger. On the other hand if the field is large enough for field enhanced emission then the activation energy should be lowered - which we have already seen is not the case.

An alternative explanation is that the capture of charge by a defect will give a small local change in the electric field - over a distance of the order of the Debye length $L_D = (\varepsilon_S KT/q^2 N_A)^{1/2}$. For $N_A = 10^{14}$ cm$^{-3}$, $L_D = 0.4\mu m$ so it is possible that the field can extend far enough to influence dark charge generation from a number of generation centres (in the vicinity of the buried channel), particularly at the channel stop boundary where $N_A$ will be reduced.

Returning to the possibility that the 'flipper' defects are at or near the interface we note that $n_i$ and $v_{th}$ change rapidly near the interface and so will $\tau_e$ and $\tau_c$. If the trap is in the oxide then either tunnelling or thermionic emission processes will be involved. For tunnelling Kandiah et al [32] give

$$t_t = \exp(2Ky)/4\, n_s\, v_{th}\, \sigma_n$$

where y is the distance of the trap to the silicon interface and

$$K = 2\pi\, (2m^* E_o)^{1/2}/h$$

where $E_o$ is the height of the oxide potential barrier (which can be in the range 0-3.2 eV [30]), h is Planck's constant an m* is the electron effective mass. Note that tunnelling processes are not very temperature sensitive. On the other hand thermionic emission will involve a factor $\exp(-E_o/kT)$ in the time constants and can be strongly temperature activated [30].

There are several ways to reduce the problem

i) Cool the CCD. This will reduce the amplitude of the fluctuations, though if field-enhancement is involved then the activation energy will be lowered. This is the preferred option.

ii) Anneal the damage. However, the defects sites involved have not been positively identified. If they are P-V centres then annealing can be expected to occur at 150°C, but any temperature in excess of ~60° in flight would have serious implications for mechanical stability of the CCD and its mounting.

iii) Development of some mode of operation which can 'set' the flipper pixels in a given state prior to each integration eg. by ensuring that all the flipper traps are filled (or emptied). Such a technique may not be possible - ideas that might be tried are preflashing with an LED light source, artificial injection of charge into the CCD or pulsing of the electrode voltages.

### 4.3 Trapping States and Dither Clocking

During dither clocking charge is repeatedly moved between I clock phases 1 and 2. In this process charge can come into contact with radiation-induced traps at the edge of the barrier phase (I3). The sequential movement 'pumps' the trap and results in the generation of a black/white pixel pair in the image - this is a manifestation of the phenomenon of pocket pumping [21]. This was investigated by taking the difference between dithered and non-

dithered images (each averages of 16 frames). For device 12 (10 MeV proton irradiation) a total of 22 black/white pairs were found for the 2 krad region (0.035% of pixels) and 11 for the 1 krad region (0.01% of pixels) - so for 2 krad on the whole device we might expect roughly 100-200 black/white pair pixels. This is a relatively small number. In each integration time there were 590 clock dithers (with one dither per line). Hence for a one electron trap the amplitude of the black/white pair will be ±590 electrons. At an amplifier gain setting of 109 electrons/ADU it was found that the black/white pair amplitudes were as shown in figure 4.3-1 for one and two dithers per line. Also shown are the expected peaks for 1, 2, 3 and 4 electron traps (a one electron trap should give an amplitude of 590/109 = 5.4 ADU on one dither per line or 10.8 ADU on 2 dithers per line). It is seen that the correspondence with the expected peak positions is tolerably good. Note that the number of black/white pairs can be reduced by reducing the clock low voltage of the barrier phase I3 (or rising the clock low voltage of I1 and I2) this keeps the charge away from any trapping states under I3 as explained by Janesick [21]. This technique was found to be effective - the voltage difference needed being ~1V. In the present case this voltage change is probably unnecessary since the black/white pair amplitude is small compared with the dark signal nonuniformity. A 2-electron trap gives a black/white amplitude of $1.18 \times 10^3$ electrons/pixel (equivalent to a dark current of 0.075 $nA/cm^2$ at 21°C). Note that with the present readout rate a frame (with its 590 line dithers) takes 0.5015s to readout. For MERIS there is a fast dumping of unwanted lines and the integration time reduces to around 38ms. However the dither rate would be kept at one per useful line so that the ratio of black/white pair amplitude to dark current would be the same. Even if the operating temperature is reduced to 5°C the black/white pairs would be small compared with the dark signal nonuniformity. We conclude that they are not a serious drawback to dither operation for CCD temperatures of 5°C or higher.

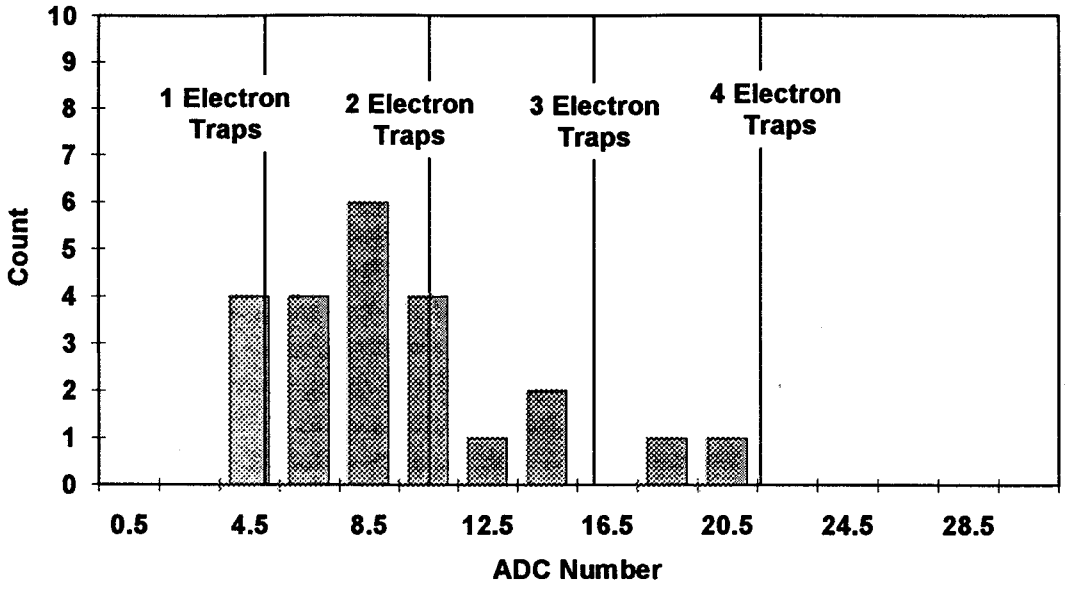


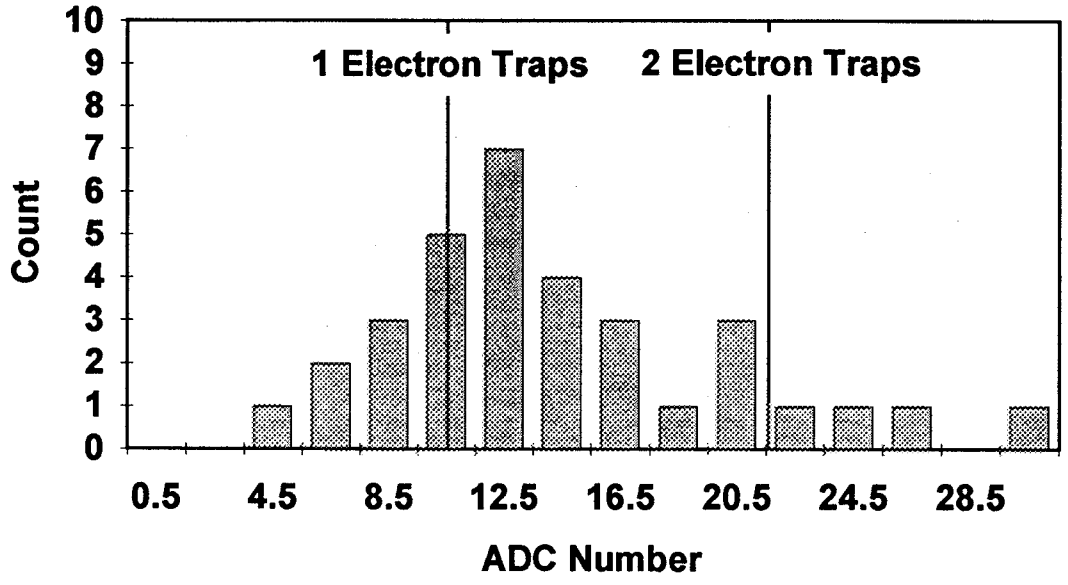


**Figure 4.3-1 Histograms of black/white pairs for dither clocking**

# 5. MISSION ANALYSIS

In this section we consider how to extrapolate experimental and theoretical results to predict the effects to be expected for the mission environment. We consider three areas: ionization damage, bulk displacement damage and transient effects.

## 5.1 Ionization Damage

This is straightforward to predict given the device damage at any dose since effects are expected to be linear with dose. The mission dose will depend on the instrument shielding. Dose-depth curves for solar maximum and solar minimum are given in figures 5.1-1 and 5.1-2.

## 5.2 Displacement Damage

For the MERIS orbit, this is dominated by the effects of trapped protons.

Displacement damage depends on the energy spectrum of the incident radiation (after shielding) and on the device effects (at each energy). For parameters such as CTE and average bulk dark current there is a linear dependence on the non-ionizing energy loss (NIEL). Figure 5.2-1 shows NIEL as a function of energy (data points from Burke, Private Communication 1991, theoretical fit from Johlander, Private Communication 1992).

To calculate the damage the NIEL curve must be multiplied by the trapped proton differential spectrum. This was modelled using the 'space radiation' Code [33]. Figure 5.2-2 shows the differential fluences before and after shielding for solar maximum and solar minimum (shielding file taken from the Aerospatiale sector analysis, document PP-TN-AER-ME-0010 issue 01). Also shown is the incident spectrum from the Aerospatiale model. It is seen that the agreement with the space radiation model is good. Hence the latter model will be used in this section - as it gives information on proton energy spectra. Note that the solar flare contribution (as simulated either with the Stassinopoulos and King or the Feynman (JPL) model) is relatively small and will not be considered here.

Figure 5.2-3 shows spectra behind instrument shielding on a linear scale. These peak at an energy ~60 MeV. Figure 5.2-4 shows the product of the NIEL curve (figure 5.2-1) and the proton spectra after shielding (figure 5.2-3) - both on logarithmic and linear scales. The linear plot shows clearly that low energy protons, though having a high NIEL, do not contribute much to the total damage - which is judged by the total area under the plots. In fact 85% of the damage is due to proton energies in the range 10-250 MeV.

In order to extrapolate the results of section 4 we need the area under the curves of figure 5.2-4 divided by the NIEL at 10 MeV - this gives the equipment number of 10 MeV protons experienced during the mission. The results are

| | |
|---|---|
| solar maximum | $3.62 \times 10^9$ p/cm$^2$ |
| solar minimum | $5.56 \times 10^9$ p/cm$^2$ |

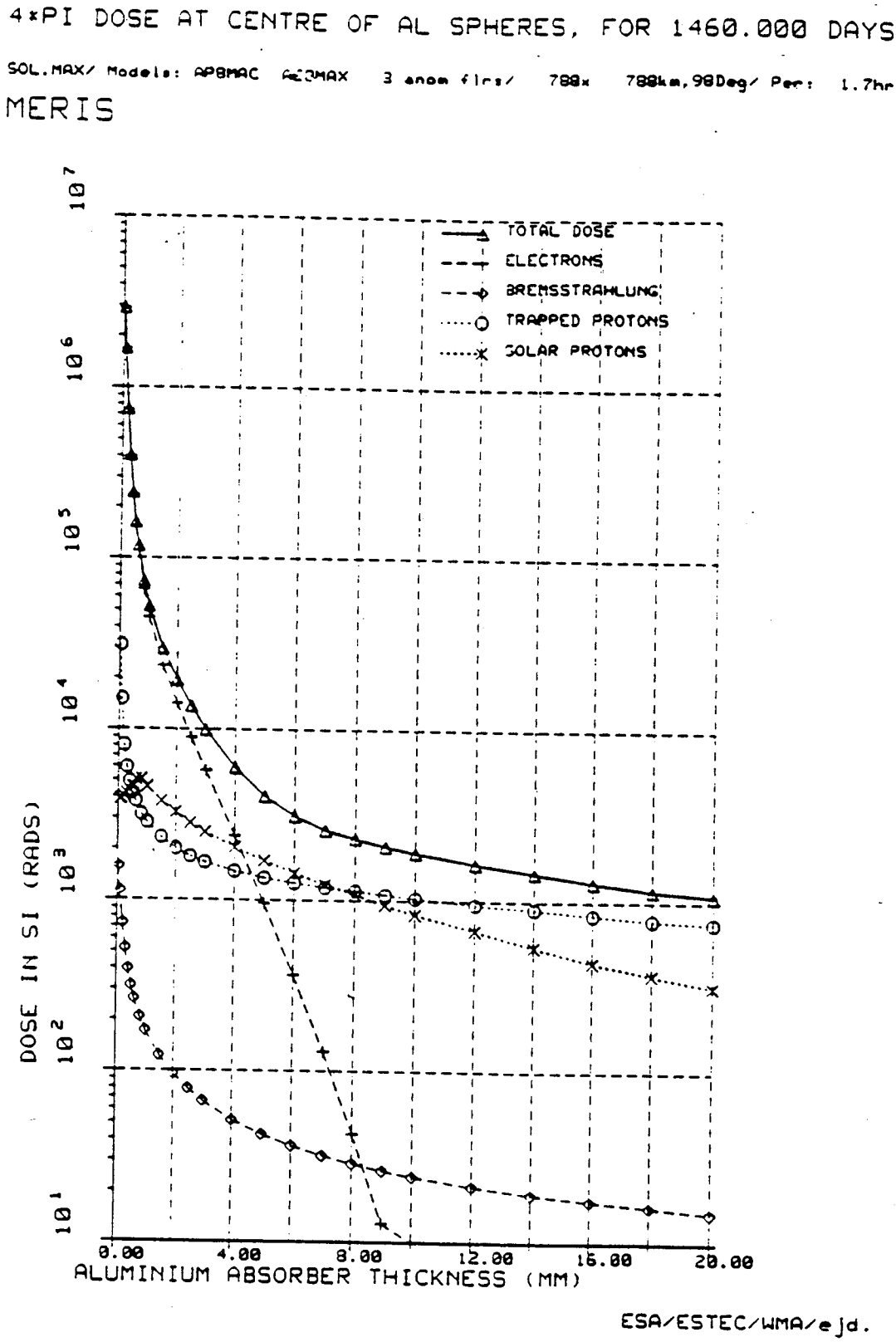


**Figure 5.1-1 Dose depth curve for solar maximum**

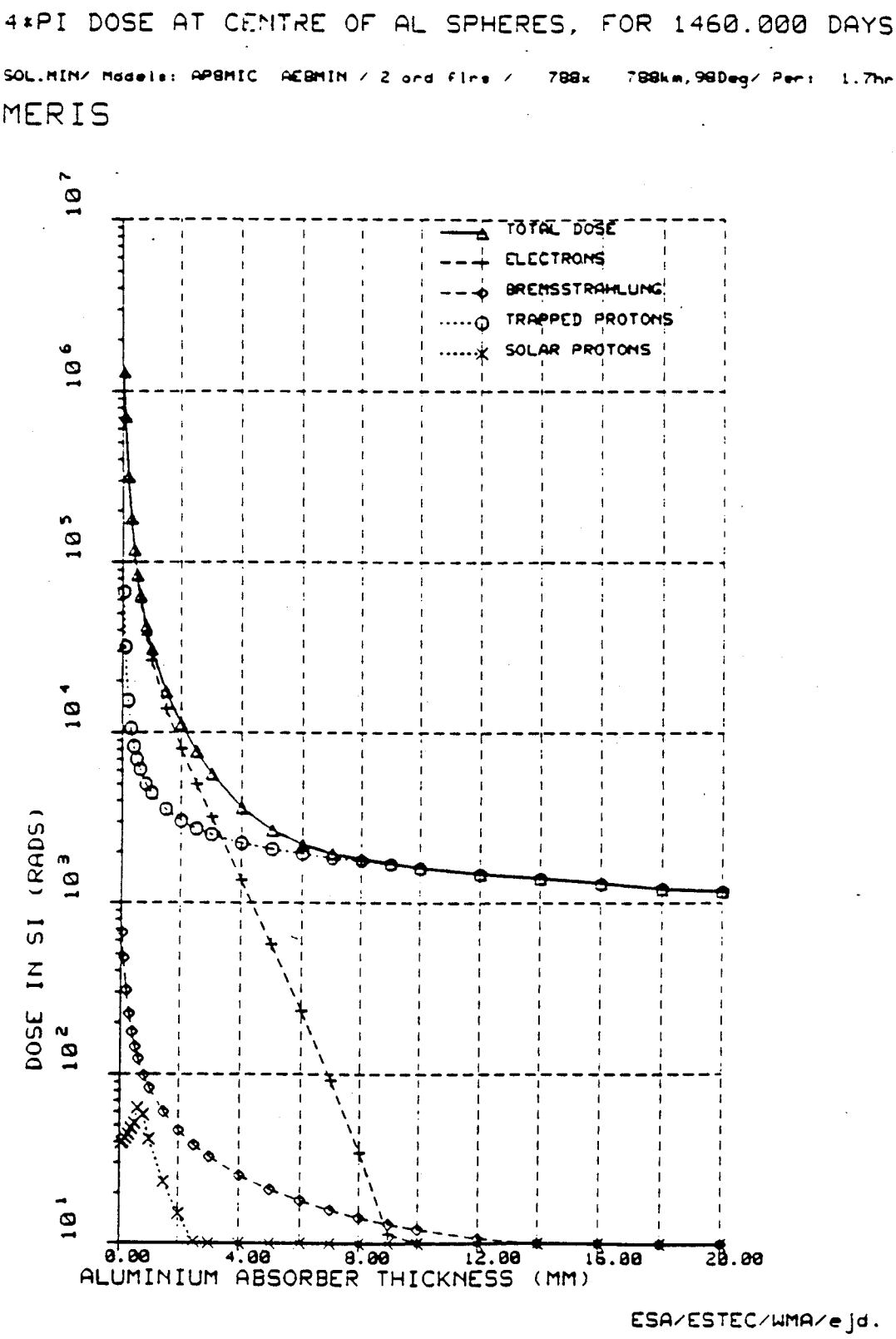


**Figure 5.1-2 Dose depth curve for solar minimum**

Hence results for CTE and bulk dark current changes (expressed per krad, = 1.79 x $10^9$ p/cm$^2$ at 10 MeV) should be multiplied by:

| | **multiplication factor (mission/krad)** |
|---|---|
| solar maximum | 2.0 |
| solar minimum | 3.1 |

Results for CTE and bulk dark current damage were:

parallel signal loss per pixel transfer/krad = 6.0 x $10^{-5}$
serial signal loss per pixel = 1.1 x $10^{-5}$
bulk dark current increase in nA/cm$^2$ at 21°C/krad = 0.10

so these become for the EOL in the mission environment:

| | **solar minimum (4 years)** | **solar maximum (4 years)** |
|---|---|---|
| Parallel CTI change (per pixel) | 1.9 x $10^{-4}$ | 1.2 x $10^{-4}$ |
| Serial CTI change (per pixel) | 3.4 x $10^{-5}$ | 2.2 x $10^{-5}$ |
| Bulk dark current increase (nA/cm$^2$ at 21°C) | 0.31 | 0.20 |
| Surface dark current increase (nA/cm$^2$ at 21°C), noninverted | 1.4 (average environment, 1.4 krad) | |
| Surface dark current increase (nA/cm$^2$ at 21°C), inverted | 0.28 (average environment, 1.4 krad) | |

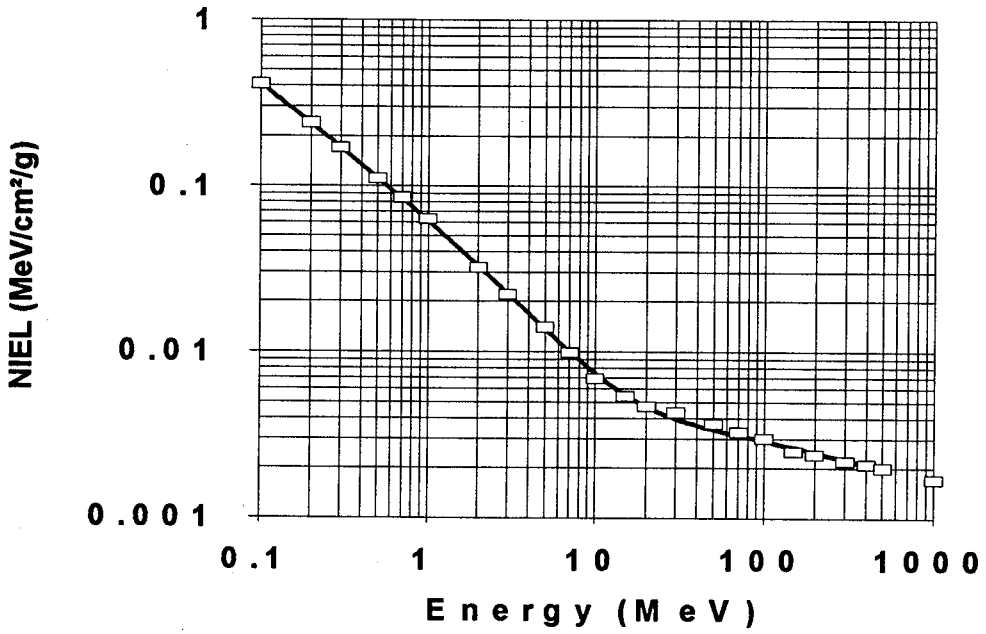


**Figure 5.2-1 Non-ionizing energy loss versus energy for protons on silicon**

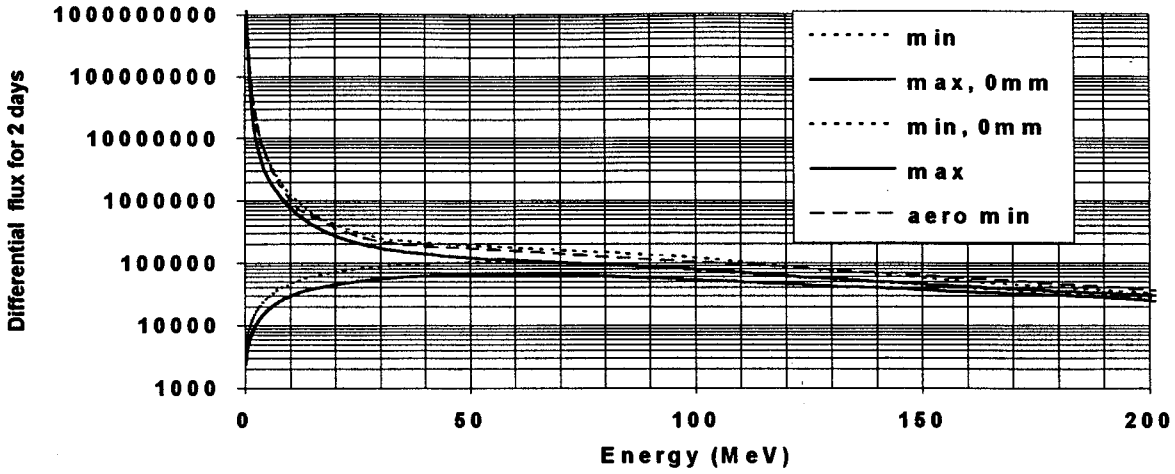


**Figure 5.2-2 Differential trapped particle fluxes**

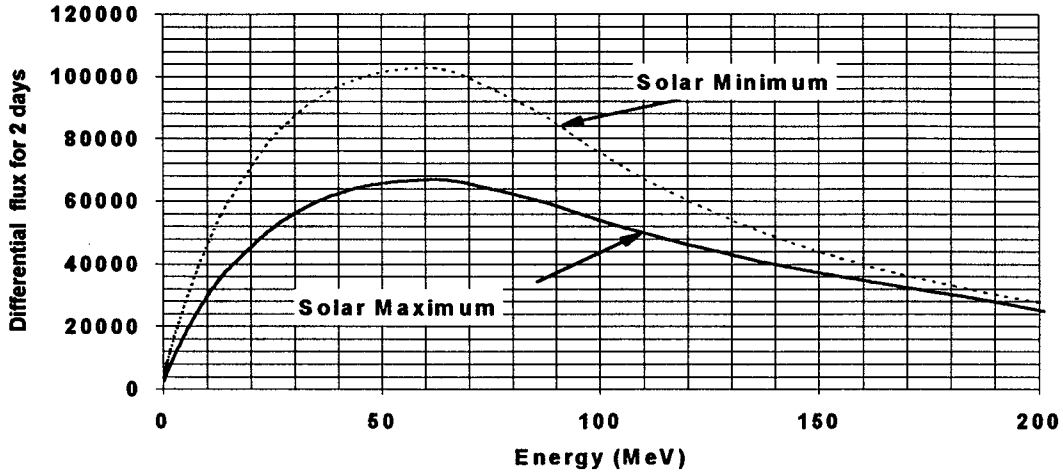


**Figure 5.2-3 Differential trapped particle fluxes at solar minimum and solar maximum, on a linear scale**

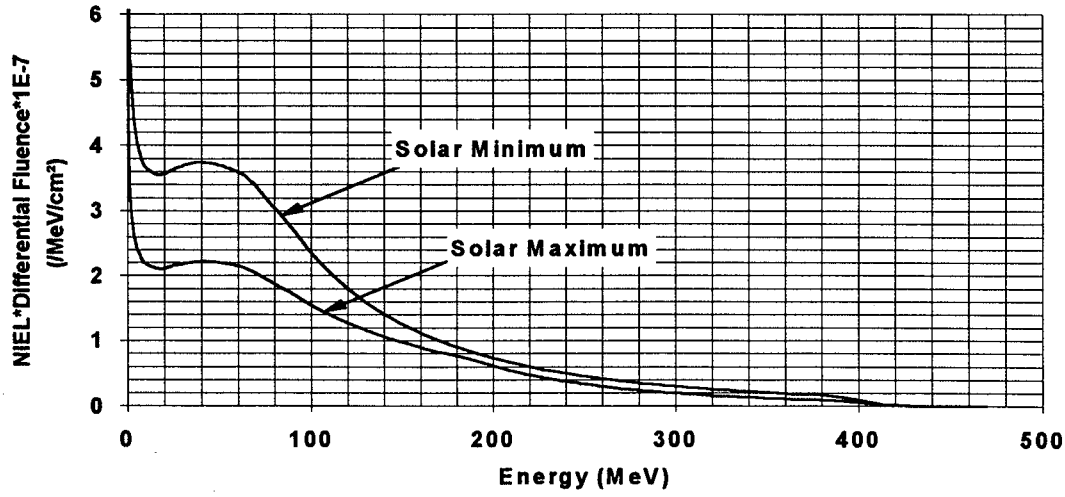


**Figure 5.2-4 Product of NIEL and differential particle flux spectra (after shielding)equivalent fluence of 10 MeV protons (over 4 years)**

## 5.3 Transient Effects

### 5.3.1 Trapped Protons

These effects are only important during passage through the South Atlantic Anomaly (SAA). The average rate of electron-hole pair creation along particle tracks will be:

$80/\beta^2$ e-h pairs /μm of track, where $\beta$ = velocity/c

The transient event size will depend on the track length (in each pixel) and on the amount of sideways diffusion which takes place before charge is collected. The signal can be estimated by taking the track length as equal to the epitaxial thickness (≈20μm) and the particles as being minimum ionizing ($\beta$=1). We then have event sizes of ~1600 electrons per pixel. Thus we can say that all trapped proton events will give significant spurious charge in the pixels affected. Note that track length distributions can be calculated using the formulae given by Ziegler and Lanford [34]. The shape of the energy loss histogram is very asymmetric, with a large signal tail [35] and it should be noted that signals greater than the average value are quite likely.

To calculate the number of events we refer to figure 5.3-1 which shows positional fluxes (before shielding) for trapped protons during solar minimum. These fluxes are significant ($>10^3$/cm$^2$/s) for periods of ~0.1 hr out of an orbit period of 1.67 hours. Integrating the flux spectra from figure 5.2-3 gives the total flux of particles after shielding as 1.58 p/cm$^2$ /2 days at solar minimum = 91.3 p/cm$^2$/s. If these all occur during 0.1 hr then the average arrival rate during SAA passage is 1.5 x $10^3$ p/cm$^2$/s or approximately 60 particles/MERIS integration time. Given that each event will spread over several pixels, we can expect that 100-200 pixels in each image will be significantly affected during passage through the peak of the SAA.

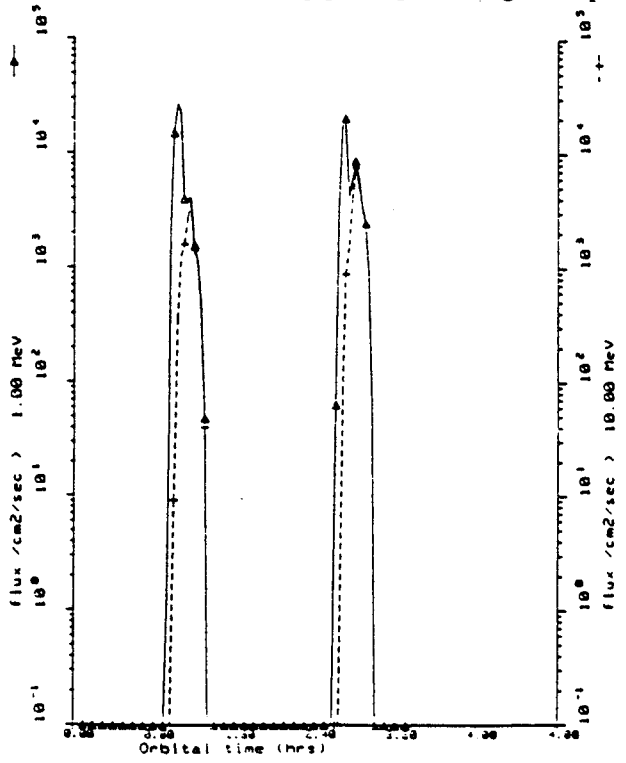


**Figure 5.3-1 Positional fluxes for trapped protons during solar minimum**

5.3.2 Bremsstrahlung

This is caused by the slowing down of trapped electrons by the spacecraft and instrument shielding. Figure 5.3-2 shows positional electron fluxes for a 99° 900 km orbit [3] - ie. one similar to the MERIS orbit. It can be seen that the electron flux comes from the SAA and the North and South Polar horns. Note that the SAA electrons are relatively soft and hence are ranged out quicker. No bremsstrahlung spectra were available for the MERIS environment. However a glance at figure 5.3-3 shows that the differential flux spectrum for the ROSAT orbit 57° 550 km) - for which results are available [4] - is similar to that for MERIS. Figure 5.3-4 shows the ROSAT data for solar maximum scaled up by a factor 2.5 gives a good representation to the situation for MERIS. Figure 5.3-5 shows the corresponding bremsstrahlung spectrum for various shielding thicknesses. The energy of the photons is predominantly in the range 0.5 - 5 MeV. In this regime the interaction with the silicon of the CCD is via the Compton effect.

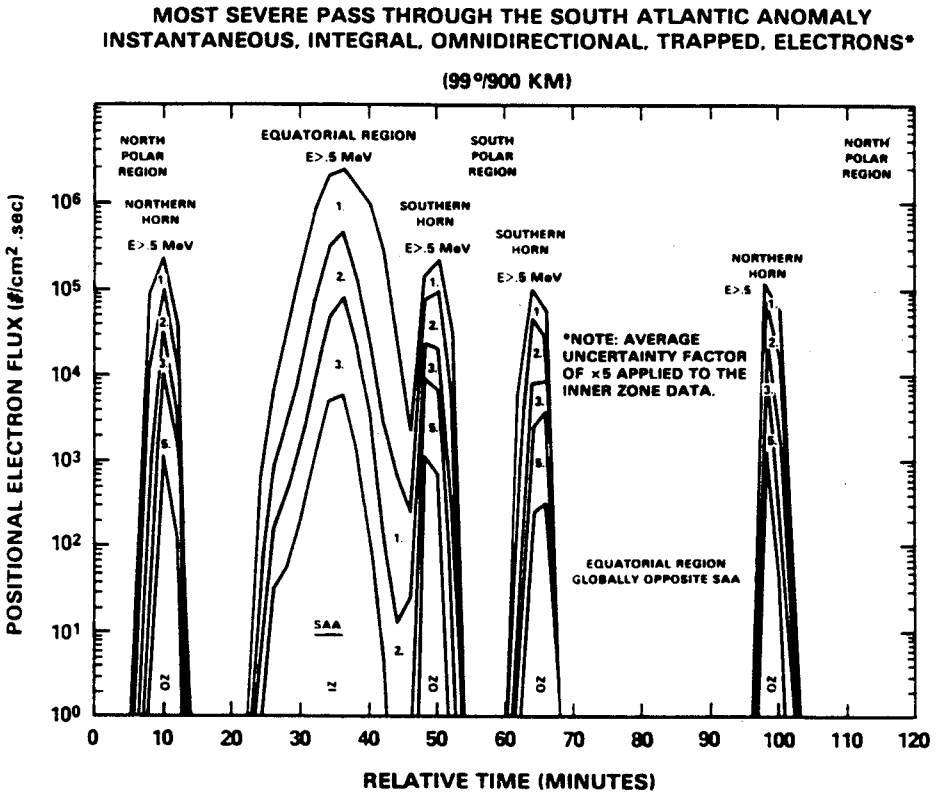


**Figure 5.3-2 Positional fluxes for trapped electrons for a 99° 900km orbit [3]**

To calculate the number of a Compton Scattering events in the CCD we multiply the differential spectrum in figure 5.3-5 and multiply by the probability for Compton Scattering (= exp $-t/l$) where t is the epitaxial thickness (= 20μm) and l is the attenuation length (figure 5.3-6). To get an event rate per CCD frame we assume that 20% of the orbit is spent going through the horns of the trapped electron belt where the flux will be high. The average flux during passage through the horns is then 5x the orbit averaged flux. and the flux per MERIS integration time (37.4 ms) is:

| shield thickness ($g/cm^2$) | number of Compton events in 20μm/integration time (37.4 ms) |
|---|---|
| 3 | 0.20 |
| 5 | 0.27 |
| 10 | 0.13 |

The result is relatively insensitive to shielding with ~1 event every 5 frames.

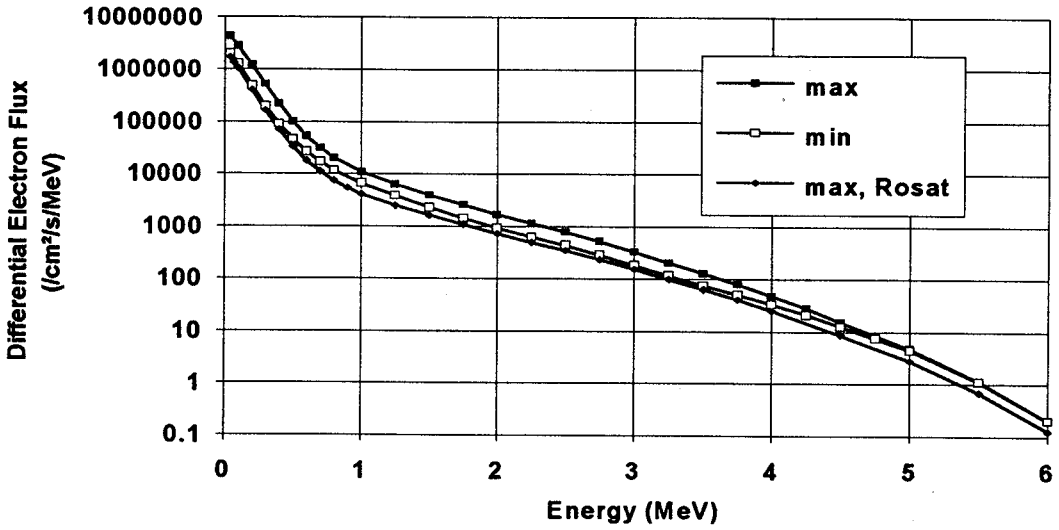


**Figure 5.3-3 Differential electron flux for MERIS (Aerospatiale data)and ROSAT [4]**

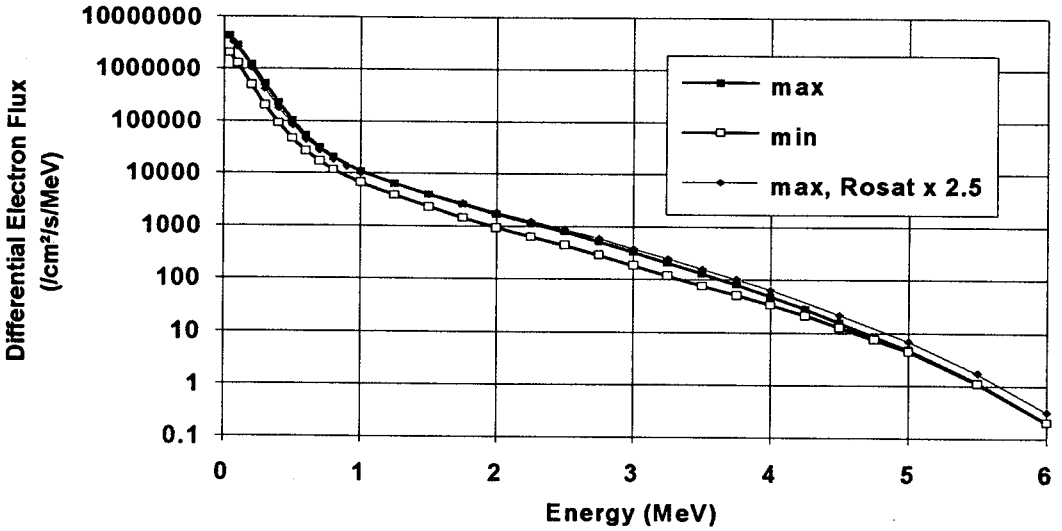


**Figure 5.3-4 Differential electron flux for MERIS (Aerospatiale data)and ROSAT data increased by a factor 2.5**

Calculating the event size is somewhat difficult but as a first approximation we can assume that the Compton electrons are minimum ionizing thus giving 80 electrons/μm of track or 1600 electrons in a 20μm track. Holland [36] has given measurements on EEV CCDs with 20 and 50μm epitaxial thicknesses (figure 5.3-7). Note that $Co^{60}$ gamma rays have an average energy of 1.25 Mev and hence give a good simulation of bremsstrahlung photons. It is seen

that events with total size up to 10,000 electrons can be produced (integrated over all the pixels in the track). Event sizes per pixel can be as high as ~5,000 electrons. Figure 5.3-8 shows an image of electron tracks after $Co^{60}$ illumination taken from a recent memo from J R Janesick at JPL [37] (pixel size 7.5 x 7.5$\mu m^2$).

We note that for MERIS calibrations will involve averages over 500 frames, so that the averaging process will reduce the event size by 500 to ~10 electrons at most. Thus the effect is small but may not be negligible. Hence calibration during passage through the polar horns should be avoided if possible.

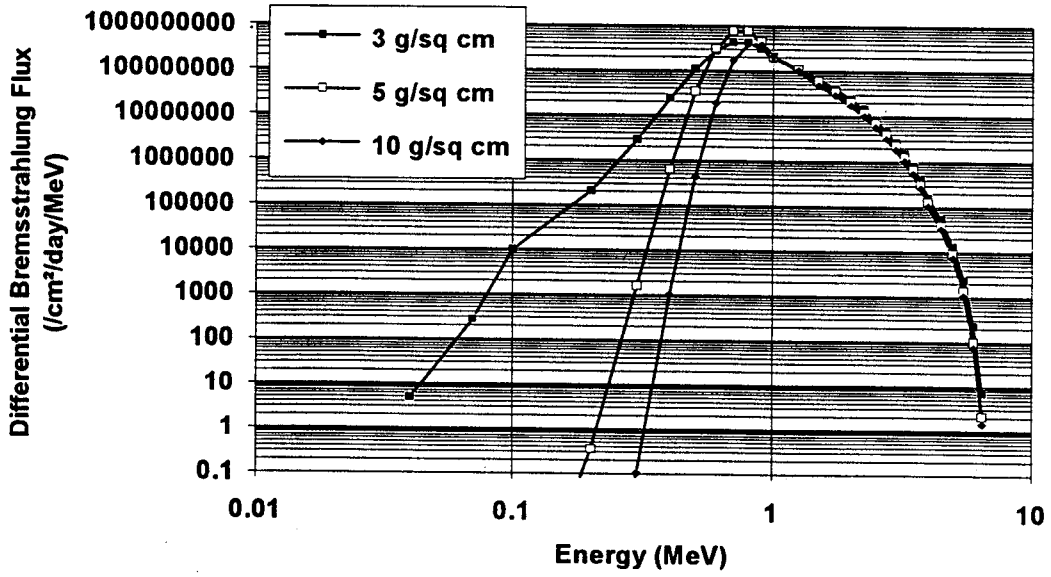


**Figure 5.3-5 Bremsstrahlung spectra for 2x ROSAT and various shielding thicknesses.**

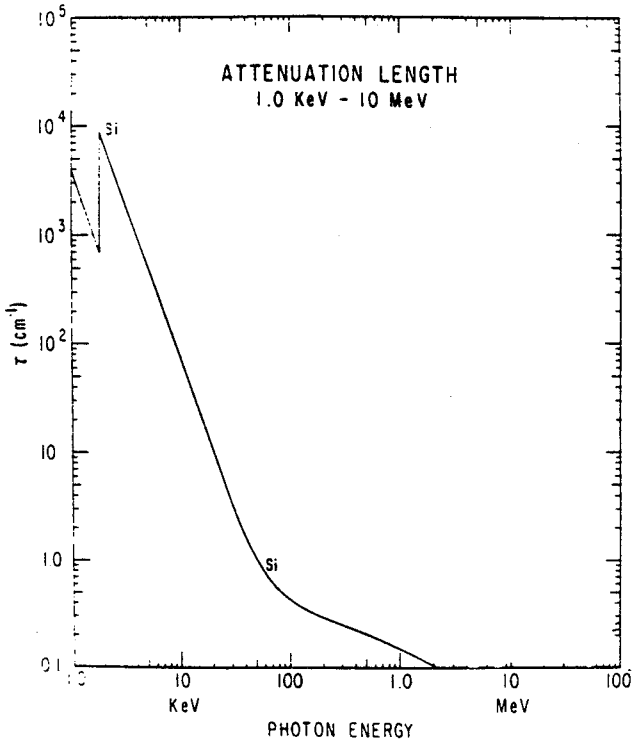


**Figure 5.3-6 Attenuation length for silicon**

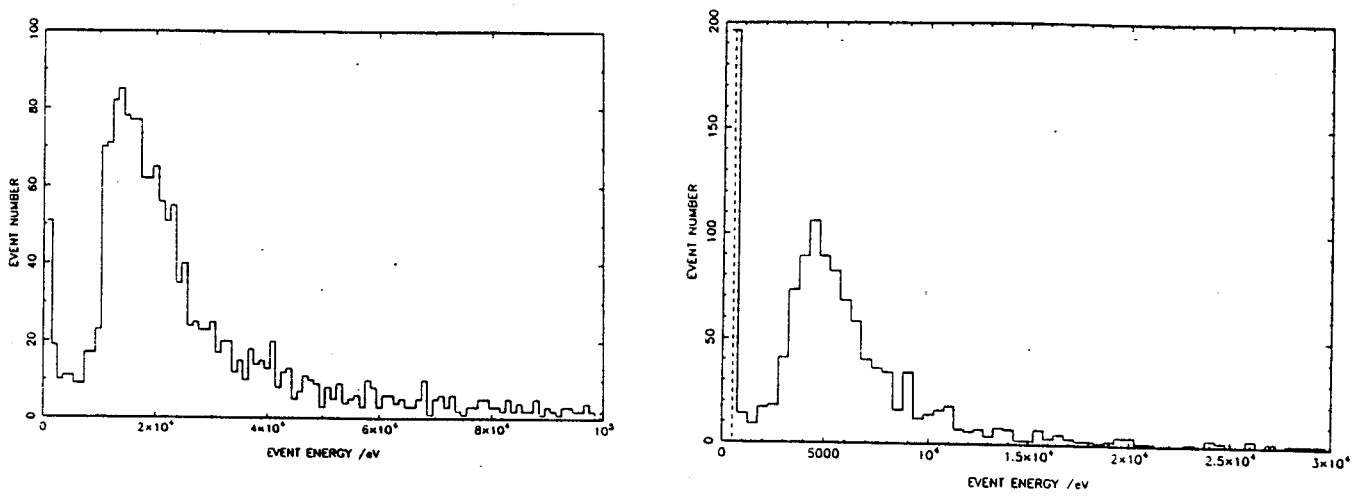


**Figure 5.3-7 $Co^{60}$ spectra for EEV CCDs [36]**

**Figure 5.3-8 $Co^{60}$ image [37]**

# 6. REFERENCES


1. E G Stassinopoulos and J P Raymond, 'The space radiation environment for electronics', Proc IEEE, 76(11), 1423-1442 (1988).

2. E J Daly, 'The analysis of space radiation environments for ESA projects', ESA Journal, 12, 229-247 (1988).

3. E G Stassinopoulos, 'Charged particle radiation exposure of geocentric satellites', in High-Energy radiation background in Space, Sanibel Island, FL 1987, eds. A C Rester and J I Trombka, AIP Conference Proceedings 186, 3-63 (1989).

4. E G Stassinopoulos, J M Barth and R L Smith 'ROSAT charged particle environment study', NASA report X-600-87-13 (GSFC, September 1987).

5. J M Killiany, 'Radiation effects in silicon charge-coupled devices', Topics in Applied Physics, 38, 147-176 (1980).

6. J Janesick, G Soli, T Elliott and S Collins, 'The effects of proton damage on charge-coupled devices', in Charge Coupled Devices and Solid State Image Sensors II, Proc SPIE, 1447, 87-108 (1991).

7. G R Hopkinson, 'Space radiation effects on CCDs', Proc ESA Electronics Components Conference, ESTEC, Noordwijk, The Netherlands, 12-16 November 1990, ESA SP-313, 301-306, March 1991.

8. G R Hopkinson, 'The effect of space radiation on CCDs', Presented at the ICSO '91 Conference 25-27 September 1991, Toulouse, France.

9. G R Hopkinson, 'Radiation effects on CCDs for spaceborne acquisition and tracking applications', RADECS 91, IEEE Proceedings 368-372 (1992). (Note: last page missing).

10. G R Hopkinson, 'Proton radiation testing of CCDs for the SILEX project', European Space Agency contract report (August 1991).

11. T Roy, S J Watts and D Wright, 'Radiation damage effects on imaging charge coupled devices', Nuclear Instruments and Methods, A-27, 545-557 (1989).

12. M S Robbins, T Roy and S J Watts, 'Degradation of the charge transfer efficiency of a buried channel charge coupled device due to radiation damage by a beta source, RADECS 91, IEEE proceedings 327-332 (1992).

13. A Homes-Siedle, A Holland, B Johlander and L Adams, 'Limiting the effects of radiation damage in charge-coupled devices by control of operating conditions', ibid pp 338-342.

14. A Holmes-Siedle, A Holland, A Den Boggende and F A Jansen', Evaluation of proton tests on EEV charge-coupled devices', CCD radiation project Vol III, Final report on ESTEC Contract 8815/90/NL/LC (1991).

15. R W Tallon, W T Kemp, M R Ackermann, M H Owen and A Hoffland, 'Radiation damage in MOS transistors as a function of the angle between an applied electric field and various incident radiations (protons, electrons and $Co^{60}$ gamma rays)', IEEE Trans on Nuclear Science, NS-34(6), 1208-1213 (1987).

16. S J Watts and M S Robbins, informal presentation at ESTEC CCD working group meeting, December 1991.

17. B E Burke and S A Gajar, 'Dynamic suppression of interface-state dark current in buried channel CCDs', IEEE Trans on Electron Devices, ED-38(2), 285-290 (1991).

18. D Hervé, I Lefesvre and E Dupont-Nivet, 'Cumulated dose long term effects in charge coupled devices', RADECS 91, IEEE proceedings, 343-347.

19. G A Hawkins, 'Lateral profiling of interface states along the sidewalls of channel-stop isolation', Solid-State Electronics, 28(9), 945-956 (1985).

20. S M Sze, Physics of Semiconductor Devices (2nd Edn), p90 (Wiley Interscience, New York, 1981).

21. J R Janesick, 'Two tricks for antiblooming operation', JPL MemorandumMay 10 1990.

21a. A Delamere, J Bare, T Ebben, J Flores, G Kleiman, M Blouke and M P McCormick, 'A high radiometric performance CCD for the third generation stratospheric aerosol and gas experiment' in Charge Coupled Devices and Solid State Image Sensors II, Proc SPIE, 1447, 204-213 (1991).

22. A M Mohsen and M F Tompsett, 'The effects of bulk traps on the performance of bulk channel charge-coupled devices, IEEE Trans on Electron Devices ED-21,701-712 (1974).

23. S D Brotherton and P Bradley, 'Defect production and lifetime control in electron and γ-irradiated silicon', J App Phys, 53(8), 5720-5732 (1982).

24. E K Banghart, J P Lavine, E A Trabka, E T Nelson and B C Burkey, 'A model for charge transfer in buried channel charge-coupled devices at low temperature', IEEE Trans on Electron Devices, ED-38, 1162-1174 (1991).

25. G R Hopkinson and Ch. Chlebek, 'Proton damage effects in an EEV CCD imager', IEEE Trans, on Nuclear Science, NS-36(6), 1865-1871 (1989).

26. A Holland, A Holmes-Siedle, B Johlander and L Adams, 'Techniques for minimising space proton damage in scientific charge coupled devices', IEEE Trans on Nuclear Science NS-38(6), 1663-1670, (1991).

27. P W Marshall, C J Dale and E A Burke, 'Proton-induced displacement damage distributions and extremes in silicon microvolumes', IEEE Trans on Nuclear Science, NS-37(6), 1776-1783, (1990).

27a K L Wang, Y H Lee and J W Corbett, 'Defect distribution near the surface of electron-irradiated silicon', Appl Phys Lett, 33(6), 547-548 (1978).

28. C J Dale, P W Marshall and E A Burke, 'Particle-induced dark current fluctuations in focal plane arrays', IEEE Trans on Nuclear Science, NS-37(6), 1784-1791, (1990).

29. M J Kirton, M J Uren, S Collins, M Schulz, A Karmann and K Scheffer, 'Individual defects at the Si:SiO2 interface, Semicond Sci Technol, 4, 1116-1126 (1989).

30. M Schulz and A Karmann, 'Single defects and noise in sub-μ MOSFETs', in Fifth Congress of the Brazilian Society of Microelectronics, Proc SPIE, 1405, 2-18, (1990).

31. R D McGrath, J Doty, G Lupino, G Ricker and J Vallerga, 'Counting of deep-level traps using a charge-coupled device', IEEE Trans on Electron Devices, ED-34(12), 2555-2557 (1987).

32. K Kandiah, M O Deighton and F B Whiting, 'A physical model for random telegraph signal currents in semiconductor devices', J Appl Phys, 66(2), 937-948 (1989).

33. Space Radiation, Severn Communications Corp., Millersville, MD.

34. J F Ziegler and W A Lanford, 'The effect of sea level cosmic rays on electronic devices', J Appl Phys, 52(6), 4305-4312 (1981).

35. H Bichsel, 'Energy loss and ionization of fast charged particles in a 20μm silicon detector', Nuclear Instrum and Methods, A235, 174-179 (1985).

36. A D Holland, 'Radiation effects in CCD x-ray detectors', PhD Thesis, Leicester University (1990).

37. J R Janesick, JPL Memo, 27 August 1991.